

Advanced Techniques for Constituent-Based Progressive Failure Analysis of
Composite Structures

by

Douglas J. Kenik

A thesis submitted to the Department of Mechanical Engineering and the Graduate
School of the University of Wyoming in partial fulfillment of the requirements for the
degree of

MASTER OF SCIENCE

in

MECHANICAL ENGINEERING

Laramie, Wyoming

August, 2009

ACKNOWLEDGEMENTS

I would like to thank Professor Andrew Hansen whose excellent instruction and guidance throughout this project, and the years of my education, has helped to mold my understanding of engineering practices. Your vast knowledge throughout this research has been inspiring, and I thank you for helping my education to be an amazing experience.

I would also like to extend my sincere gratitude to Firehole Technologies for funding this project and taking an interest in my education through the past four years. The employees of your company are outstanding, and they have helped tremendously in my understanding of finite element practices.

Finally, I would like to thank Dr. Mark Garnich for introducing me to the vast world of composites. Your willingness to help in any circumstance is greatly appreciated and never forgotten.

TABLE OF CONTENTS

LIST OF FIGURES	vi
LIST OF TABLES	x
1. A REVIEW OF FAILURE ANALYSIS OF COMPOSITE STRUCTURES	1
1.1 Introduction to Progressive Failure Analysis of Composite Structures	1
1.2 A Review of Current Approaches to Progressive Failure Analysis	4
1.3 A Comparison of Failure Predictions.....	9
1.4 Numerical Implementation of Theories Discussed.....	16
2. MULTI-CONTINUUM THEORY	19
2.1 The Multi-Continuum Concept.....	20
2.2 MCT Constituent Level Failure Criteria.....	25
2.3 Nonlinear Matrix Material Behavior.....	28
2.3.1 Matrix Damage	28
2.3.2 Enforcing a Consistent Set of Material Characteristics	29
2.4 Nonlinear Finite Element Implementation.....	31
2.5 Implementation Challenges	33
2.5.1 Enhanced Micromechanics Solution Times.....	34
2.5.2 Thermal Stresses	35
2.5.3 Orthotropic Degradation	37
3. ENHANCING MICROMECHANICS SOLUTION SPEED	38
3.1 Micromechanics Model	38
3.2 ABAQUS Micromechanics Solution	41
3.3 The Search for Computational Speed	42
3.3.1 Mesh Density Analysis	42
3.3.2 Composite (Volume Averaged) Stress and Strain Calculation	44
3.3.3 Implementation of Constraint Equations	45
3.3.4 Static Condensation	46
3.3.5 Finite Element Matrix Operations.....	47
3.4 Implementation	52

3.5	Results.....	56
4.	CURE STRESS ANALYSIS.....	57
4.1	Linear Viscoelasticity	58
4.2	Time-Temperature Superposition	67
4.2.1	Theory and Finite Element Implementation	67
4.2.2	Derakane 510 Master Curve	73
4.3	Micromechanics Cool-Down Study.....	75
5.	THE IMPACT OF THERMAL LOADS ON FAILURE PREDICTIONS.....	78
5.1	Failure Coefficient Modifications for Thermal Cure Stresses	79
5.1.1	Purely Mechanical Approach.....	79
5.1.2	Cure Stress Approach	85
5.2	Unidirectional Lamina Room Temperature Failure Predictions	91
5.3	Unidirectional Lamina Cryogenic Failure Envelope Comparisons	98
5.4	Laminate Cryogenic Failure Envelope Comparisons	103
6.	ORTHOTROPIC MATERIAL DEGRADATION	107
6.1	Ply-Level Material Degradation.....	108
6.1.1	Submicrocrack (Void) Accumulation	108
6.1.2	Transverse Cracking	110
6.2	Orthotropic Degradation	112
6.2.1	Degradation Parameters	115
6.2.2	Degradation Under Transverse Compression	121
6.3	Implementation of the Post-Failure Response for Transverse Cracking.....	122
6.4	Results.....	123
7.	CONCLUSIONS AND RECOMMENDATIONS	130
7.1	Micromechanics Enhancements.....	130
7.2	Effects of Cure Stresses on Multidirectional Laminates.....	132
7.3	Analysis of Failure at Cryogenic Temperatures.....	133
7.4	Orthotropic Degradation	134
7.5	Progressive Failure at Elevated Temperatures	135
	REFERENCES	137
	APPENDIX A.....	I
	APPENDIX B.....	V

APPENDIX C	X
C.1 Macroscopic Stress Calculation	XI
C.2 Macroscopic Strain Calculation	XVI

LIST OF FIGURES

Figure 1.1 Local (a) and global (b) material coordinates.....	5
Figure 1.2 Experimental failure data for combined σ_{11} and σ_{12} loading for a unidirectional lamina (Hinton <i>et. al</i> , 2004).....	11
Figure 1.3 Experimental failure data for combined σ_{xx} , σ_{xy} loading of an EGlass/LY556 $[90^\circ / \pm 30^\circ]_s$ laminate (Hinton <i>et. al</i> , 2004).....	11
Figure 1.4 Theoretical failure predictions for combined σ_{xx} , σ_{xy} loading of an EGlass/LY556 $[90^\circ / \pm 30^\circ]_s$ laminate (Rotem, 1998).	12
Figure 1.5 Transverse cracking of a $[0^\circ / 90^\circ]_s$ laminate (Akula, 2007).....	13
Figure 1.6 Experimental stress-strain data for combined $\sigma_{xx}:\sigma_{yy} = 1:-1$ of a $[0^\circ / \pm 45^\circ / 90^\circ]_s$ AS4/3501-6 laminate (Hinton <i>et. al</i> , 2004).....	14
Figure 1.7 Stress-strain curve for a combined $\sigma_{xx}:\sigma_{yy} = 0:1$ of a $[0^\circ / \pm 45^\circ / 90^\circ]_s$ AS4/3501-6 laminate where the solid lines are theoretical predictions and the open circles are experimental data (Mayes and Hansen, 2002).....	15
Figure 2.1 Schematic of a multi-continuum decomposition showing: (a) a continuum point for a unidirectional composite lamina, (b) a continuum point for the fibers only, and (c) a continuum point for the matrix material.	21
Figure 2.2 Nonlinear material behavior, and a representation of the tangent and secant moduli for the i^{th} increment.....	32
Figure 3.1 Idealized uniform hexagonal packing representation for a unidirectional composite (Garnich, 1996).....	39
Figure 3.2 ANSYS periodic unit cell and finite element mesh from Garnich (1996).....	40
Figure 3.3 ABAQUS standard mesh for a 60% fiber volume fraction.	42

Figure 3.4 Optimized mesh for a 60% fiber volume fraction.	43
Figure 3.5 Symmetric partitioned mesh for a fiber volume fraction of 60%.	47
Figure 3.6 Rotated coordinate axes about the longitudinal axis.	51
Figure 3.7 Representation of global node numbering for (a) the master fiber super-element and (b) a fiber super-element rotated 120° about the longitudinal axis of the unit cell centroid.	53
Figure 3.8 Node representation for a fiber volume fraction of 60% for (a) the uncondensed super-element and (b) the condensed super-element. Note some back face nodes are hidden in (a), and the back face corner node is hidden in (b).	53
Figure 3.9 Matrix node representation for a fiber volume fraction of 60% for (a) the uncondensed super-element and (b) the condensed matrix super-element. Note some back face nodes are hidden in (a).	54
Figure 4.1 Constant applied stress for an isothermal loading.	60
Figure 4.2 Creep compliance resulting from a strain history cause by an applied stress, σ_0	60
Figure 4.3 Composite stress and applied temperature history for a combined thermomechanical loading.	66
Figure 4.4 (a) Matrix strains and (b) reinforcement strains predicted by Garnich and Hansen (1997).	66
Figure 4.5 Matrix and reinforcement strains as a function of time predicted by the current micromechanics model.	67
Figure 4.6 Master curve for Derakane 510.	74
Figure 5.1 Matrix invariant axes plotted against composite biaxial stress space.	83
Figure 5.2 Matrix invariant axes incorporating matrix cure stresses plotted against biaxial composite stress space.	90

Figure 5.3 Room temperature failure envelope comparison for an EGlass/LY556 glass/epoxy unidirectional lamina.	94
Figure 5.4 Room temperature failure envelope comparison for a T300/BSL914C carbon/epoxy unidirectional lamina.	95
Figure 5.5 Room temperature failure envelope comparison for a Silenka/MY750 glass/epoxy unidirectional lamina.	96
Figure 5.6 Room temperature failure envelope comparison incorporating only mechanical failure coefficients for a Silenka/MY750 glass/epoxy unidirectional lamina.	97
Figure 5.7 Failure envelope comparisons for a T300/BSL914C carbon/epoxy unidirectional lamina at cryogenic temperatures for combined transverse tension/compression and longitudinal shear.	100
Figure 5.8 Failure envelope comparisons for a T300/BSL914C carbon/epoxy unidirectional lamina at cryogenic temperatures for combined longitudinal tension/compression and longitudinal shear.	101
Figure 5.9 Failure envelope comparisons for a T300/BSL914C carbon/epoxy unidirectional lamina at cryogenic temperatures under biaxial loading.	102
Figure 5.10 Biaxial failure envelope comparison for a $[90^\circ / \pm 30^\circ]_s$ T300/BSL914C laminate at $\Delta T = -150^\circ\text{C}$ and room temperature.	105
Figure 5.11 Biaxial failure envelope comparison for a $[0^\circ / \pm 45^\circ / 90^\circ]_s$ T300/BSL914C laminate at $\Delta T = -150^\circ\text{C}$ and room temperature.	106
Figure 6.1 Schematic of transverse ply cracking, Akula (2007).	110
Figure 6.2 E_2^d/E_2 , ν_{21}^d/ν_{21} , and ν_{23}^d/ν_{23} lamina degradation as a function of normalized transverse crack density as presented by Akula (2007). Symbols represent FEA data.	113

Figure 6.3 G_{12}^d/G_{12} lamina degradation as a function of normalized transverse crack density as presented by Akula (2007). Symbols represent FEA data.....	114
Figure 6.4 G_{23}^d/G_{23} lamina degradation as a function of normalized transverse crack density as presented by Akula (2007). Symbols represent FEA data.....	114
Figure 6.5 E_2^d/E_2 and ν_{23}^d/ν_{23} as a function of normalized transverse crack density.....	116
Figure 6.6 G_{12}^d/G_{12} as a function of normalized transverse crack density.....	116
Figure 6.7 G_{23}^d/G_{23} as a function of normalized transverse crack density.....	117
Figure 6.8 E_2^d/E_2 and ν_{23}^d/ν_{23} as a function of the third strain invariant.....	118
Figure 6.9 G_{12}^d/G_{12} as a function of the third strain invariant.....	119
Figure 6.10 G_{23}^d/G_{23} as a function of the third strain invariant.....	119
Figure 6.11 Biaxial failure envelope comparison for a $[90^\circ / \pm 30^\circ]_s$ EGlass/LY556 laminate.....	124
Figure 6.12 Failure envelope comparison for a $[90^\circ / \pm 30^\circ]_s$ EGlass/LY556 laminate.....	125
Figure 6.13 Stress-strain curve comparison for a $[\pm 55^\circ]_s$ EGlass/MY750 laminate loaded under $\sigma_{xx}:\sigma_{yy} = 1:2$	127
Figure 6.14 Close up stress-strain curve comparison for a $[\pm 55^\circ]_s$ EGlass/MY750 laminate loaded under $\sigma_{xx}:\sigma_{yy} = 1:2$	128
Figure 6.15 Stress-strain curve comparison for a $[\pm 55^\circ]_s$ EGlass/MY750 laminate loaded under $\sigma_{xx}:\sigma_{yy} = 0:1$	129
Figure B.1 Hexagonally packed representative volume element (RVE).....	VIII
Figure C.1 Optimized mesh representation of unit cell with corner node labels.....	XI
Figure C.2 Representation of shearing about the x_3 -axis for the micromechanics unit cell.....	XIII
Figure C.3 Representation of shearing about the x_2 -axis for the unit cell.....	XIV
Figure C.4 Representation of shearing about the x_1 -axis for the micromechanics unit cell.....	XV

LIST OF TABLES

Table 3.1 Composite material property comparison for a T300/BSL914C carbon/epoxy with a 60% fiber volume fraction.....	44
Table 4.1 Viscoelastic matrix and elastic reinforcement material properties for a 60% fiber volume fraction.....	65
Table 4.2 Average isotropic material properties of Derakane 510 for various temperatures.	73
Table 4.3 Derakane 510 neat resin viscoelastic data for various temperatures.....	73
Table 4.4 Master curve coefficients for Derakane 510.....	74
Table 4.5 Fiber material properties for micromechanics cool-down study.....	76
Table 4.6 Coefficients of thermal expansion for micromechanics cool-down study.....	76
Table 4.7 Glass/vinylester composite viscoelastic cool-down constituent stresses (<i>MPa</i>) for a fiber volume fraction of 60%. Superscripts represent the constituent.....	76
Table 4.8 Carbon/vinylester composite viscoelastic cool-down constituent stresses (<i>MPa</i>) for a fiber volume fraction of 60%. Superscripts represent the constituent.....	77
Table 4.9 Glass/vinylester and carbon/vinylester composite elastic cool-down constituent stresses (<i>MPa</i>) for a fiber volume fraction of 60%. Superscripts represent the constituent.....	77
Table 5.1 Fiber, matrix, and composite transversely isotropic material properties for EGlass/LY556.	92
Table 5.2 Fiber, matrix, and composite transversely isotropic material properties for Silenka/MY750.....	93
Table 5.3 Fiber, matrix, and composite transversely isotropic material properties for T300/BSL914C.....	93

Table 5.4 Comparison of ply level and constituent level stresses for a linear elastic cool-down of 150°C for a $[90^\circ / \pm 30^\circ]_s$ EGlass/LY556 laminate.....	98
Table 6.1 Lamina curve fitting coefficients for composite degradation based on Equation (6.10).....	120
Table 6.2 Matrix curve fitting coefficients for matrix degradation based on Equation (6.11).....	120

1. A REVIEW OF FAILURE ANALYSIS OF COMPOSITE STRUCTURES

Fiber reinforced composite materials are used in a wide variety of structures due to their light weight and superior strengths. Applications include aircraft, boats, motor vehicles, military equipment, and technologically advanced sporting equipment. Composites encompass an extremely broad material class as a multitude of fiber and matrix combinations can be used to form materials with a wide variety of thermomechanical characteristics.

While composites offer superior attributes to the vast majority of materials used for lightweight structures, predicting their failure accurately is a difficult task. Designers compensate for unknowns in failure predictions by generating overly conservative designs, thereby mitigating many of the benefits promised by composites. However, the increasingly severe service loads for composites are now placing a premium on optimized designs, thereby warranting significant time and effort devoted to accurate failure analysis.

1.1 Introduction to Progressive Failure Analysis of Composite Structures

Thermomechanical analysis of composite structures proves to be an extraordinarily complex task as structural components are typically comprised of multiple plies with

fiber orientations varying from ply to ply. Ply-level material properties depend on constituent (fiber and matrix) material properties of the selected lamina, and furthermore, the constituent properties can be functions of time, temperature, moisture, and even stress and strain fields.

Over the past fifty years, significant progress has been made in characterizing the mechanical properties of a wide variety of composite materials in various environments. While these advances have expanded the availability and use of the materials to a variety of applications, failure predictions are still of large concern due to lack of availability of an accepted progressive failure methodology. Consequently, overweight, and usually overly stiff, structures are repeatedly designed. Alternatively, many composite structures are fabricated using a “design and test” process that is extremely costly and time consuming.

The fundamental “building block” of a composite structure is the composite ply, or lamina, assumed here to consist of continuous fibers of carbon or glass embedded in an epoxy matrix. Clearly, an accurate representation of ply-level behavior requires detailed knowledge of the material properties of the fiber and matrix. Fiber material properties are difficult to characterize as fiber diameters are on the order of microns, thereby making strength and stiffness measurements perpendicular to the length of the fiber extremely difficult to obtain. Matrix material properties present a different set of problems, as these properties are usually strong functions of the environment and the

deformation. The constituent unknowns of the fiber and matrix lead to substantial uncertainty when predicting failure of laminates placed in severe environmental settings and loading combinations. The failure analysis itself is highly nonlinear leading to intense computational demands.

Failure of composite structures may be attributed to a variety of factors other than the prescribed mechanical loading, with the most notable of these being environmental conditions. For instance, large temperature differences can cause failure in a laminate before any mechanical loading is applied. This phenomenon is due to the inherent mismatch of the fiber and matrix thermal expansion properties at the ply level as well as the global mismatch of thermal expansion properties between the various plies that comprise the laminate. Thus, any failure prediction must take into consideration the “stress-free” temperature at which no residual stresses are present, and the temperature of interest where thermally induced stress fields within the constituents may be a significant factor.

The characterization of failure is also vague, as many forms exist for a laminate. Failure mechanisms transcend multiple geometric scales, including submicrocrack accumulation in the matrix, ply-level matrix cracking, fiber fracture in tension, and fiber buckling in compression. It is interesting to note that the various failure modes described may be related to the individual fiber and matrix constituents. This phenomenon is a central theme of this entire thesis.

The various scenarios of constituent level failure identified above must all be handled differently. For instance, the case of fiber breakage or buckling ultimately results in the inability of the ply to carry load, and thus final failure of the ply should be concluded. However, submicrocrack accumulation on the ply-level does not result in a completely failed ply, but rather a damaged ply in which the ability of the ply to carry load is only hindered. Therefore the material properties of the matrix, and consequently the failed lamina, should be reduced but also allowed to further carry loads.

The use of the term “failure” is also considered a loose interpretation of an analyst’s design goals and needs. For example, pressure vessels containing fluid are said to fail if the tank “weeps” fluid through a wall due to matrix cracking, while an aircraft structure might be assumed failed when excessive deformations exist or delamination of plies are present. In extreme cases, ultimate failure may not be declared until a laminate is unable to sustain a given load.

1.2 A Review of Current Approaches to Progressive Failure Analysis

In order to provide a comprehensive means of evaluating leading failure theories, a World-Wide Failure Exercise (WWFE) was developed in which contributors were asked to provide progressive failure analysis predictions for a known set of experimental data comprised of multiple materials, laminate configurations, and multiaxial load cases. Hinton, *et. al.* (2004) provide a detailed discussion of the Exercise and the theories of the

contributors. Here, an overview of several theories is presented in order to provide a brief introduction of the current approaches to progressive failure analysis of composite laminates.

Before the discussion continues, an introduction of local and global material coordinates is provided as a basis for the remainder of this thesis. Figure 1.1(a) depicts ply-level local (material) coordinates, while Figure 1.1(b) depicts a global material coordinate system for a laminate.

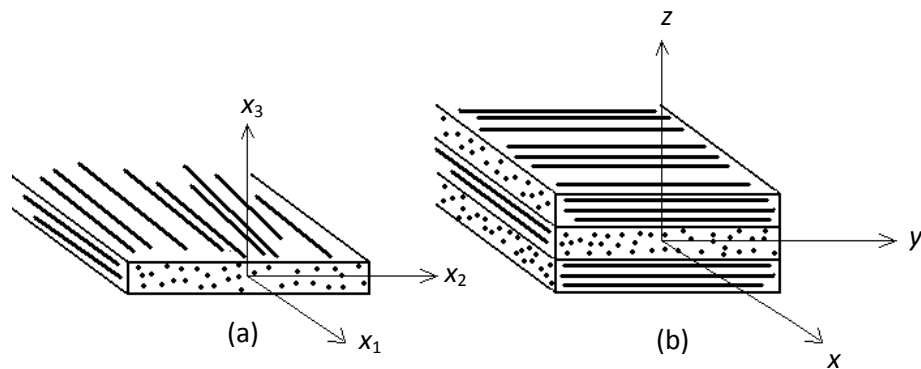


Figure 1.1 Local (a) and global (b) material coordinates.

Any quantities relating to x_1 , x_2 , or x_3 reference the local coordinate system, while any quantities relating to x , y , or z reference the global coordinate system. Note that if the laminate is comprised solely of a unidirectional lamina, the local and global coordinates coincide. In the case of local (material) coordinates, x_1 is always taken to define the fiber direction while the x_1 - x_2 plane defines the plane of the lamina.

Perhaps the most notable failure theory of the WWFE is that of Puck and Schürmann (1998). They develop a three-dimensional interactive stress-based theory which recognizes two modes of failure from laminate stresses, namely matrix (inter-fiber) and fiber failure, based upon an “action plane” approach. For inter-fiber failure, a principal plane is calculated about the longitudinal (fiber) axis on which cracking is most likely to form. Depending on the crack initiation angle, two different material degradation schemes are employed. In particular, under transverse tension (σ_{22}) the lamina properties E_2 , G_{12} , and ν_{12} are degraded continuously from material independent experimentally deduced curves. In transverse compression, only the lamina shear modulus G_{12} is degraded.

Another widely known failure theory is that of Rotem (1998), in which fiber and matrix failure are separated in accordance with the early work of Hashin (1980). Macroscopic stresses and strains are used to predict failure and initiate cracking, and progressive failure analysis is conducted by continuous degradation of an isotropic matrix elastic modulus after crack initiation is detected. Degrading the matrix stiffness in all directions is overly restrictive as experimental and numerical studies clearly reveal directional dependence of matrix failure. Uniform matrix degradation could very well have an erroneous influence on a damaged ply’s ability to carry loads in certain directions and should be considered cautiously.

Perhaps one of the most well known composite failure theorists is Tsai, as the Tsai-Hill failure criterion is widely used in the industry. Liu and Tsai (1998) develop a two-dimensional quadratic stress-interactive failure criterion based on ply-level stresses and strains. Thermal cure stresses are included in the failure predictions by using a linear theory of thermoelasticity. While this approach seems reasonable for a first order prediction of thermal residual stresses from a curing cycle, the stresses predicted by a linear elastic theory are unrealistically high as significant stress relaxation occurs in polymers at elevated temperatures. Liu and Tsai implement a progressive failure analysis which relies on the values of the lamina transverse strain to predict transverse crack densities. Specifically, if the strain is positive, a ply-discount method is employed in which ply-level transverse stiffness and shear properties are degraded instantaneously to material dependent tabulated values.

Gotsis and Chamis (1998) introduce a theory that relies on generating lamina material properties from those of the constituents. While failure is still calculated from stresses at the ply-level, damaged lamina material properties are calculated by suddenly degrading the fiber and/or matrix to approximately 10% of the original material properties and updating the macroscopic properties through a finite element analysis. While this type of degradation is not considered accurate in the case of multi-directional laminates, the concept of allowing homogenized ply-level material properties to be formulated through the constituent properties is considered a large step in enforcing a degradation process in which the constituent material properties can be reduced independently of each other.

Huang (2004) opens the constituent window of information further than Chamis by proposing a means of decomposing the lamina stresses to those of the constituents with the use of an approximate two-dimensional theory that relates fiber and matrix stresses to those of the composite. Huang also realizes the importance of calculating failure at the constituent level rather than the lamina level, and proposes a maximum stress failure criterion for both the fiber and matrix. Thus, fiber and matrix failure modes are independent and easily identifiable.

Mayes and Hansen (2004) also propose a means for decomposing lamina stress/strain fields to the constituent level by the use of an exact three-dimensional relationship developed from continuum mechanics. Like Huang, the importance of calculating failure at the constituent level is realized, and a three-dimensional stress-interactive failure criterion is developed, largely motivated by Hill (1950). A distinct advantage of the theory proposed by Mayes and Hansen is the coupling of the failure algorithm to a routine finite element analysis, thus eliminating the need for classical lamination theory (CLT). Furthermore, Mayes and Hansen follow the work of Gotsis and Chamis (1998) by calculating ply-level material properties for failed fiber and failed matrix states prior to performing any failure analysis.

Both the theories of Huang, and Mayes and Hansen, realize the importance of thermal residual stresses on failure predictions. Moreover, because constituent information can

be easily calculated, residual stresses from mismatched material properties at both the ply and constituent level can be used within any analysis. The ability to readily compute *constituent* level thermal stresses is a distinguishing feature from the other failure theories discussed thus far, where only thermal stresses at the ply-level may be computed.

Huang approximates the residual stresses from a cure cycle by using linear thermoelasticity and finds some failure predictions are altered due to the residual stresses. Again, the assumption of linear elasticity in a thermal analysis of curing will lead to unrealistically high stresses. Moreover, to the knowledge of the author, the strength parameters used for the failure predictions are not altered to account for the presence of the residual stresses. If thermal residual stresses are incorporated in a failure analysis, strength parameters must reflect the impact of the thermal stresses. In contrast, Mayes and Hansen argue that the effect of thermal cure stresses are naturally accounted for in strength data provided by the WWFE. The differing views of Huang, and Mayes and Hansen, are thoroughly explored in this work.

1.3 A Comparison of Failure Predictions

In accordance with the WWFE, 19 theories were submitted providing predictions for a variety of failure envelopes and stress-strain curves. The first portion of the Exercise, named Part A, required contributors to submit blind predictions knowing only unidirectional lamina and constituent material properties. Detailed information regarding the Exercise can be found in the publication of Hinton *et. al.* (2004). Here, a brief

summary of the experimental data and “blind” predictions is presented to offer observations on what specific details should be considered in any progressive failure theory.

The first three test cases of the WWFE involve unidirectional composites under two-dimensional multiaxial loads. The unidirectional fiber orientation of these materials removes the need for any post-failure degradation scheme, as any matrix or fiber *failure* results in complete failure of the lamina. An examination of the experimental data for these cases shows that any max-stress or max-strain non-interactive theory behaves poorly when longitudinal shear stresses are encountered, as these theories only consider normal stresses along the longitudinal and transverse directions. For instance, Figure 1.2 shows failure data for combined longitudinal tension/compression and longitudinal shear. The data clearly indicate longitudinal shear stresses influence failure loads.

Following the analysis of unidirectional laminates, the WWFE requested four envelopes for various multidirectional laminates and material combinations. These test cases included a layup configuration of $[90^\circ / \pm 30^\circ]_s$ for an EGlass/LY556 glass/epoxy laminate loaded in combined $\sigma_{xx}:\sigma_{xy}$. Figure 1.3 depicts the experimental data for this laminate.

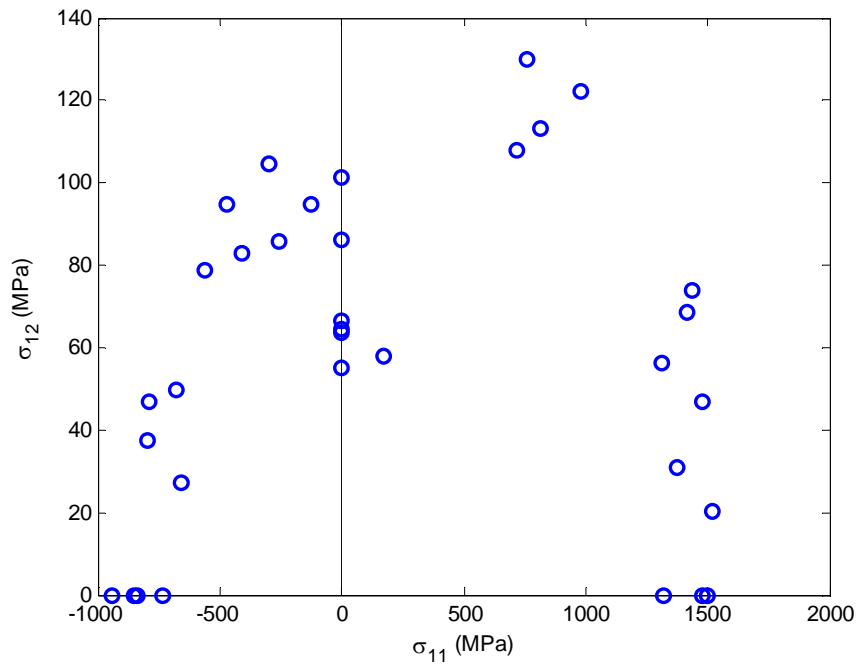


Figure 1.2 Experimental failure data for combined σ_{11} and σ_{12} loading for a unidirectional lamina (Hinton *et. al.*, 2004).

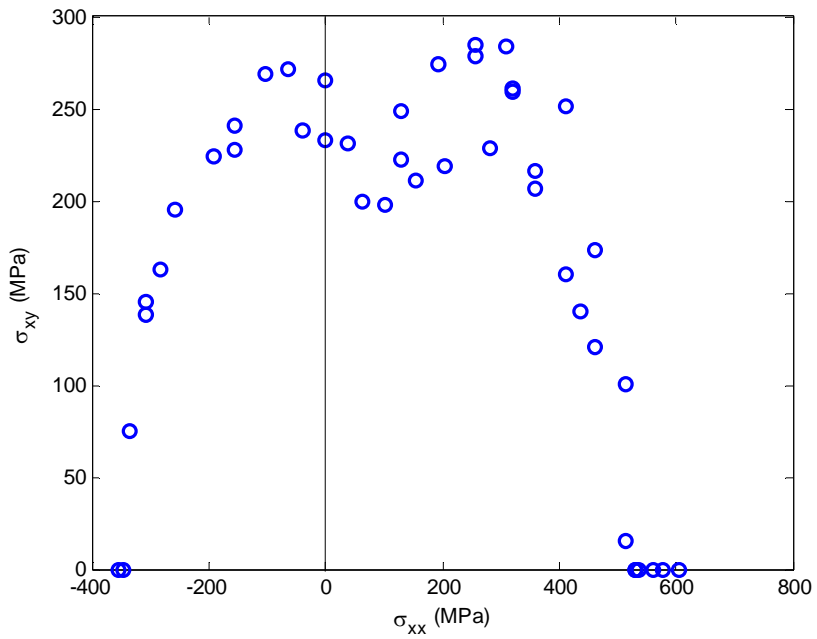


Figure 1.3 Experimental failure data for combined σ_{xx} , σ_{xy} loading of an EGlass/LY556 $[90^\circ / \pm 30^\circ]_s$ laminate (Hinton *et. al.*, 2004).

Blind predictions of failure for the EGlass/LY556 laminate of Figure 1.3, as provided by Rotem (1998), are shown in Figure 1.4. It is clear that degradation of longitudinal matrix stiffness for matrix transverse failure, such as done by Rotem (1998), results in a severe under-prediction of final failure. If the matrix longitudinal stiffness is degraded, the ability of the ply to carry on-axis loads is severely hindered in a way that does not reflect experimentally observed behavior.

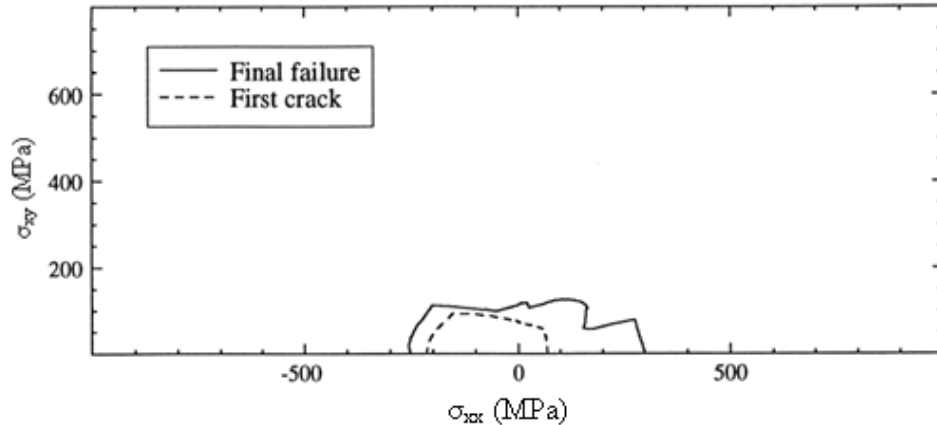


Figure 1.4 Theoretical failure predictions for combined σ_{xx} , σ_{xy} loading of an EGlass/LY556 $[90^\circ / \pm 30^\circ]_s$ laminate (Rotem, 1998).

An explanation of the lack of influence of matrix cracks on longitudinal stiffness is provided by considering matrix cracking of a $[0^\circ / 90^\circ]_s$ laminate where macroscopic cracks extend through the thickness of the laminate. The term “transverse crack” is used to refer to a crack where a unit normal vector defining the crack surface extends in the transverse direction. An example of transverse cracking is shown in Figure 1.5. In contrast, a longitudinal crack is defined by a unit normal of the crack surface extending in

the longitudinal, or x_1 , direction. Because the fibers typically carry nearly all the load under longitudinal tension, any longitudinal cracks forming in a ply would generally not inhibit the ply's ability to sustain loading in the longitudinal direction. Furthermore, the stiffness in the longitudinal direction of a ply is not affected by the presence of transverse cracks, as these cracks open perpendicular to the longitudinal direction.

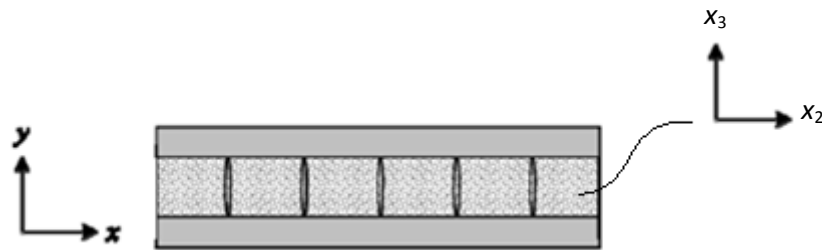


Figure 1.5 Transverse cracking of a $[0^\circ / 90^\circ]_s$ laminate (Akula, 2007).

The WWFE also required participants to make stress-strain predictions for several multidirectional laminates. Laminates were loaded in various combinations of $\sigma_{xx}:\sigma_{yy}$ to allow participants to demonstrate the ability to model material nonlinearity caused by submicrocrack accumulation and transverse cracking. Figure 1.6 shows the global stress-strain response of a $[0^\circ / \pm 45^\circ / 90^\circ]_s$ AS4/3501-6 carbon/epoxy laminate loaded biaxially as $\sigma_{xx}:\sigma_{yy} = 1:-1$. Biaxial loading of this nature produces significant longitudinal shear in the $\pm 45^\circ$ plies. From the results, one can deduce that modeling nonlinear shear is imperative to predict correct stress-strain behavior.

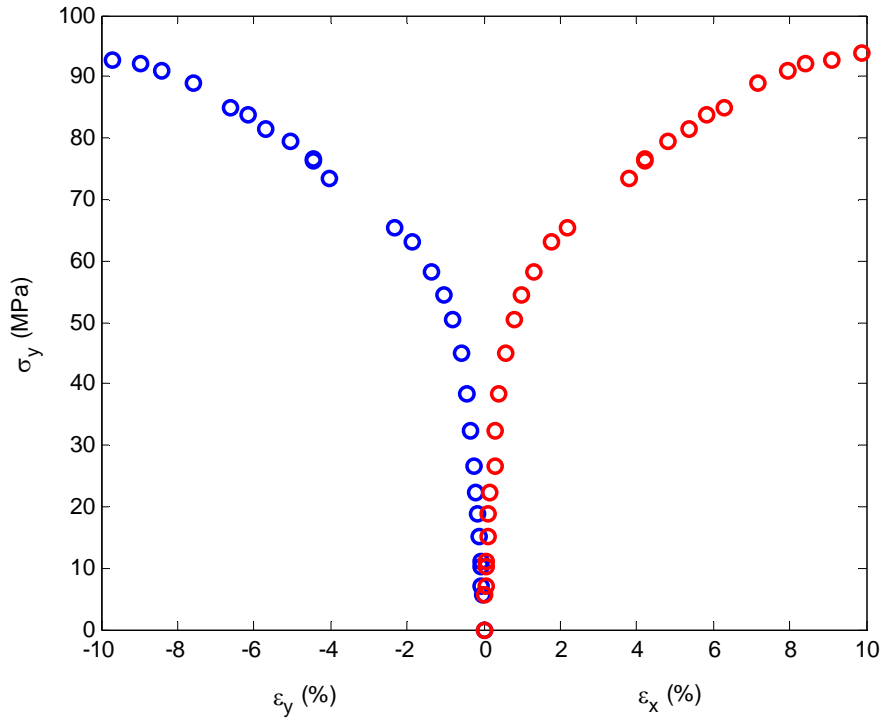


Figure 1.6 Experimental data for combined $\sigma_{xx}:\sigma_{yy} = 1:-1$ of a $[0^\circ / \pm 45^\circ / 90^\circ]_s$ AS4/3501-6 laminate (Hinton *et. al*, 2004).

Finally, Figure 1.7 shows the global stress-strain response for a $[0^\circ / \pm 45^\circ / 90^\circ]_s$ carbon/epoxy laminate loaded under transverse tension as $\sigma_{xx}:\sigma_{yy} = 0:1$. Also shown in the Figure are theoretical predictions of Mayes and Hansen (2002). The jump in the stress-strain curve near 400 MPa is caused by a prediction of matrix failure and the subsequent “zeroing” of matrix properties. Examination of theoretical predictions with experimental data suggests that post-failure matrix degradation in transverse tension should occur gradually to eliminate the unrealistic jump in the stress-strain response. Physically, gradual matrix degradation in the presence of matrix failure occurs due to load redistribution, through complex interlaminar load paths, back to the matrix a short distance from the localized failure.

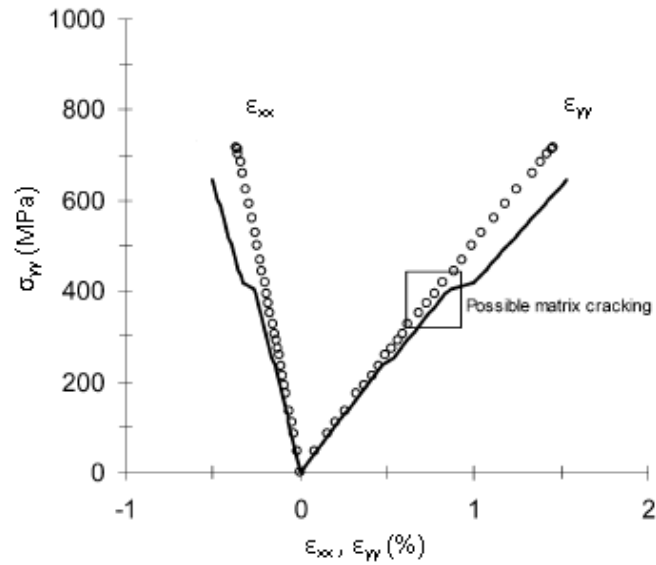


Figure 1.7 Stress-strain curve for a combined $\sigma_{xx}:\sigma_{yy} = 0:1$ of a $[0^\circ / \pm 45^\circ / 90^\circ]_s$ AS4/3501-6 laminate where the solid lines are theoretical predictions and the open circles are experimental data (Mayes and Hansen, 2002).

From the results of the WWFE cases discussed, it is evident that any successful failure criterion should incorporate certain fundamental aspects, including:

- i) Different failure modes for the fiber and matrix,
- ii) Interactive failure criteria allowing for multiaxial influence of stress or strain,
- iii) Nonlinear material behavior in longitudinal shear, and
- iv) A gradual reduction of matrix material properties in the direction of loading under transverse tension/compression.

The theories that incorporated these effects predicted the behavior of the WWFE laminates exceedingly well. The theories described by Puck (1998) and Cuntze (2004)

are notable in this regard. Furthermore, it is considered extremely advantageous to predict failure at the constituent level, as failure modes can be clearly identified. The work of Mayes and Hansen (2004) and that of Huang (2004) provide detailed constituent level information that other theories simply cannot capture.

1.4 Numerical Implementation of Theories Discussed

If nonlinear stress-strain behavior is introduced in any progressive failure theory, an incremental analysis must be performed to accurately predict material behavior at any point during the analysis. Because of this fact, it is advantageous, and perhaps even necessary from a pragmatic view, to couple failure theories with a nonlinear finite element analysis. Of all the theories presented in the Exercise, only two have explicitly accomplished this feat, namely Gotsis and Chamis (1998), and Mayes and Hansen (2004).

An additional important point related to numerical implementation is that the majority of the theories presented in the WWFE rely on classical lamination theory (CLT) to predict the stresses and strains at the lamina level. The use of CLT has serious negative consequences in the fact that only a two-dimensional stress/strain field can be considered. An extension of CLT to accommodate three-dimensional stress states commonly found in large scale structures would ultimately lead to a complex and numerically inefficient solution process. Moreover, while it may be argued that the vast majority of composite laminates are only loaded in states of plane stress, Garnich (1996) demonstrates that,

even for a state of plane stress in a lamina, the constituents have a fully three-dimensional stress state. Thus, a failure criterion trying to capture distinct failure modes in the fiber or matrix constituent must recognize the three-dimensional nature of the stress field.

An additional consideration for evaluating the fidelity of any failure theory is the relative complexity of the implementation. For example, the three-dimensional failure theory presented by Puck (1998) requires numerous curve fitting coefficients and material behavior characteristics to calculate macroscopic failure. In particular, five different failure criteria must be evaluated to determine a failure mode, and each criterion utilizes different coefficients (Puck *et. al.*, 2001). Moreover, most of the failure coefficients are empirical in nature and must be fit to material-dependent experimental stress-strain curves, which may or may not be available at the time of a failure prediction.

Finally, a desired feature of any failure prediction methodology is the ability to determine all failure coefficients prior to an analysis, and the calculations to determine the coefficients involved should be as few as possible. Furthermore, separating modes of fiber and matrix failure should be transparent and accomplished as efficiently as possible. This goal is best met by evaluating failure using constituent level stress/strain information, thereby naturally separating fiber and matrix behavior.

Noting the desired features of numerical implementation of a progressive failure analysis, the theory proposed by Mayes and Hansen (2004) is considered to be the most attractive of any developed for the WWFE. Constituent information is readily available at any point during the analysis, failure criteria evaluate to a single valued scalar for both the fiber and matrix, all coefficients are determined prior to any analysis, and the theory inherently provides failure criteria for three-dimensional stress states. All of these steps are accomplished in an extremely efficient computational manner. However, several improvements to the original theory of Mayes and Hansen (2004) are possible, and the work here-in is aimed at addressing these.

2. MULTI-CONTINUUM THEORY

The discussion presented in Chapter 1 highlights that the majority of successful progressive failure criteria for composite structures recognize distinct differences between fiber and matrix failure. Furthermore, implementation of the majority of the theories in an incremental analysis is onerous, as often numerous failure coefficients from various equations must be solved simultaneously to obtain an acceptable solution. Some of the coefficients generated for these equations must be determined as the analysis progresses, or from large quantities of experimental data that may, or may not, be available for the specified material.

It has been argued here that the most numerically efficient theory to be implemented for a composite progressive failure analysis is the MCT approach of Mayes and Hansen (2004), for which the macroscopic composite stress-state is efficiently decomposed to the constituent level. This multi-scale decomposition allows for easy identification between fiber and matrix failure states. The progressive failure analysis can also be coupled to a nonlinear finite element code with minimal additional input requirements for the analyst.

In this chapter, the general framework of the MCT progressive failure analysis of Mayes and Hansen (2004) is developed along with a collection of proposed modifications aimed at improving the theory. To begin, the concept of a multi-continuum is introduced and the relationships between macroscopic and microscopic material behavior are presented.

The MCT constituent-based failure criteria are also developed for the fiber and matrix. Matrix material behavior is inherently nonlinear, and the deformation mechanisms responsible for nonlinear inelastic behavior are discussed. Finally, an overview of the finite element implementation is presented. Issues addressed include the incremental solution scheme, effects of thermal stresses, and orthotropic degradation of the matrix material.

2.1 The Multi-Continuum Concept

The fundamental premise underlying continuum mechanics is that all mathematical variables represent average values of the quantity of interest. The averaging occurs over a material volume whose physical dimensions are small compared to the physical dimensions of the system of interest, yet large enough to represent the microstructure of a “material point.” The latter requirement is of particular interest in the context of the analysis of composite materials. Specifically, in the case of a continuous fiber unidirectional composite material, a material point must represent the characteristics of a volume large enough to contain numerous fibers and the surrounding matrix as shown in Figure 2.1(a). The macroscopic value used to characterize the stress tensor at a point in the continuum is given by the volume average of the micro-stress field of Figure 2.1(a) as

$$\bar{\sigma} = \frac{1}{V} \int_D \tilde{\sigma}(x) dV \quad , \quad (2.1)$$

where D is the region representing the continuum (material) point.

The concept of a multi-continuum simply extends the notion of a continuum to reflect coexisting materials within a material point. Such an extension is natural in any case where there are two or more clearly identifiable constituents with drastically different material properties. Hence, the composite material of Figure 2.1(a) may be viewed as two interacting continua composed of fibers (f) and matrix (m) as shown in Figures 2.1(b) and 2.1(c), respectively.

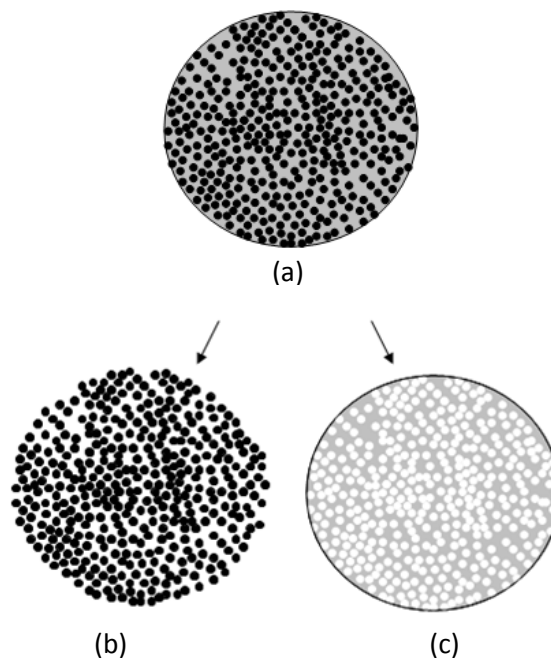


Figure 2.1 Schematic of a multi-continuum decomposition showing: (a) a continuum point for a unidirectional composite lamina, (b) a continuum point for the fibers only, and (c) a continuum point for the matrix material.

Applying the continuum definition of stress given in Equation (2.1) for each constituent there follows:

$$\tilde{\sigma}_f = \frac{1}{V_f} \int_{D_f} \tilde{\sigma}(x) dV \quad , \quad (2.2)$$

and

$$\tilde{\sigma}_m = \frac{1}{V_m} \int_{D_m} \tilde{\sigma}(x) dV \quad , \quad (2.3)$$

where

$$D = D_f \cup D_m \quad . \quad (2.4)$$

Combining Equations (2.1) through (2.3) leads to

$$\tilde{\sigma} = \phi_f \tilde{\sigma}_f + \phi_m \tilde{\sigma}_m \quad , \quad (2.5)$$

where ϕ_f and ϕ_m are the volume fractions of fiber and matrix, respectively. Likewise, a similar relationship holds for strains given by

$$\tilde{\epsilon} = \phi_f \tilde{\epsilon}_f + \phi_m \tilde{\epsilon}_m \quad . \quad (2.6)$$

While Equations (2.5) and (2.6) are standard results for any volume fraction-based mixture theory, the context of the multi-continuum constituent stress/strain fields and their distinction from the micromechanical constituent stress/strain fields is critical. Note the above relations inherently give averaged stresses and strains of the constituents as a consequence of the definition of the multi-continuum. Hence, variations of stress and strain within each constituent are not accounted for at the microscopic level.

Accommodating these variations in stress and strain at the microstructural level is computationally unfeasible. Furthermore, there is little evidence to support the value of microstresses and strains in the context of a failure analysis, as these values are clearly dependent on an actual microstructure that is random in nature. In contrast, constituent averaged stresses and strains are efficiently calculated with the MCT decomposition. These constituent fields open an exciting window of multi-scale analysis that may provide substantial insights to composite material failure that were previously unavailable.

Given a composite stress and strain field, and assuming linear elastic or linear viscoelastic behavior in an incremental loading scheme, it is a straightforward matter to decompose the composite stress/strain fields down to their constituent level stress/strain fields for the fiber and the matrix. Garnich (1996) developed the proper decomposition for a unidirectional composite consisting of linear elastic fibers in a linear elastic matrix as well as a linear viscoelastic matrix. In what follows, the linear elastic decomposition is presented, as this algorithm forms the basis for subsequent failure analyses.

The development of the MCT decomposition is best accomplished using contracted matrix notation where stress and strain tensors are represented in vector form as

$$\{\sigma\} = [\sigma_{11} \quad \sigma_{22} \quad \sigma_{33} \quad \sigma_{12} \quad \sigma_{13} \quad \sigma_{23}]^T, \quad (2.7)$$

and

$$\{\varepsilon\} = [\varepsilon_{11} \quad \varepsilon_{22} \quad \varepsilon_{33} \quad \gamma_{12} \quad \gamma_{13} \quad \gamma_{23}]^T . \quad (2.8)$$

The linear elastic constitutive relations for the composite and constituents may be written as

$$\{\sigma\} = [C](\{\varepsilon\} - \{\varepsilon_o\}) , \quad (2.9)$$

$$\{\sigma_f\} = [C_f](\{\varepsilon_f\} - \{\varepsilon_{f,o}\}) , \quad (2.10)$$

and

$$\{\sigma_m\} = [C_m](\{\varepsilon_m\} - \{\varepsilon_{m,o}\}) , \quad (2.11)$$

respectively. Here, vectors with subscript o are defined as stress-free strains, $[C]$ is the composite stiffness matrix, $[C_f]$ is the fiber stiffness matrix, and $[C_m]$ is the matrix (resin) stiffness matrix. Following the development of Garnich (1996), Equations (2.5) and (2.6) can be combined with Equations (2.9) through (2.11) to give the matrix strain vector as

$$\{\varepsilon_m\} = (\phi_m[I] + \phi_f[A])^{-1}(\{\varepsilon\} - \Delta T\{\eta\}) , \quad (2.12)$$

where

$$[A] = -\frac{\phi_m}{\phi_f}([C] - [C_f])^{-1}([C] - [C_m]) , \quad (2.13)$$

and

$$\{\eta\} = ([C] - [C_f])^{-1}([C]\{\alpha\} - \phi_f[C_f]\{\alpha_f\} - \phi_m[C_m]\{\alpha_m\}) . \quad (2.14)$$

In the above, $[I]$ is the 6×6 identity matrix, $\{\alpha\}$ is the composite coefficient of thermal expansion (CTE) vector, $\{\alpha_f\}$ is the fiber CTE vector, $\{\alpha_m\}$ is the matrix CTE vector, and ΔT is a change in temperature from an assumed stress-free state.

Given the matrix strains from Equation (2.12), the fiber strains can then be solved from Equation (2.6) as

$$\{\epsilon_f\} = \frac{1}{\phi_f} (\{\epsilon\} - \phi_m \{\epsilon_m\}) \quad . \quad (2.15)$$

Thus, if fiber, matrix, and composite material constants are known prior to a structural analysis, the constituent stresses and strains can be extracted quickly and efficiently, solely from a composite strain field.

2.2 MCT Constituent Level Failure Criteria

Virtually all successful failure theories developed for structural analysis of high performance composite materials recognize that different failure criteria apply for the fiber and matrix within a composite material. Hashin (1980) was one of the pioneers of such an approach when he proposed failure criteria for both the fiber and matrix materials within a composite based on the *composite* stress fields of a homogeneous lamina. The theory is based upon transverse isotropy of the lamina and recognizes that composite materials have different ultimate strengths in tension and compression. A failure criterion can then be defined for a lamina as

$$K_1 I_1 + L_1 I_1^2 + K_2 I_2 + L_2 I_2^2 + M_{12} I_1 I_2 + K_3 I_3 + K_4 I_4 = 1 \quad , \quad (2.16)$$

where K_i , L_i , and M_{12} are coefficients determined from composite strength data, and I_i are transversely isotropic invariants of the composite stress tensor given by Hansen (1991) as

$$I_1 = \sigma_{11} \quad ,$$

$$I_2 = \sigma_{22} + \sigma_{33} \quad ,$$

$$I_3 = \sigma_{22}^2 + \sigma_{33}^2 + 2\sigma_{23}^2 \quad , \quad (2.17)$$

$$I_4 = \sigma_{12}^2 + \sigma_{13}^2 \quad ,$$

and

$$I_5 = \sigma_{22}\sigma_{12}^2 + \sigma_{33}\sigma_{13}^2 + 2\sigma_{12}\sigma_{13}\sigma_{23} \quad .$$

A natural extension of the approach of Hashin is to develop *constituent* failure criteria for the fiber and matrix of a composite based on the *constituent* stress fields. The necessary continuum level constituent information is efficiently generated using the MCT decomposition outlined previously.

Following the work of Mayes and Hansen (2004), failure of a constituent is assumed to be quadratic in stress and hence K_1 in Equation (2.16) is set to zero. After relabeling failure coefficients for consistency, Equation (2.16) becomes

$$\pm A_1 I_1^2 - \pm A_2 I_2^2 - \pm A_5 I_1 I_2 + A_3 I_3 + A_4 I_4 = 1 \quad , \quad (2.18)$$

where differences between compression and tension have been realized through the leading superscript on the failure coefficients, A_j . Note terms A_3 and A_4 do not contain dependence on the sign of loading as these terms contain shear stresses and the square of normal stresses. Equation (2.18) represents a general interactive stress failure criterion, and it is here that a distinction is made between fiber and matrix failure.

To develop a criterion for fiber failure, it is noted that most fibers have transverse strengths much greater than their matrix counterparts, and thus it is assumed that composite transverse failure is dominated by matrix failure. It is also of interest to note that the last term in I_3 found in Equation (2.17) contains transverse shearing, which is also assumed to be matrix dominated. Based on these observations and following the derivation of Mayes and Hansen (2004), coefficients $\pm A_2^f$, $\pm A_5^f$ and A_3 are set to zero as their associated invariants involve transverse stresses. Thus, the fiber failure criterion is given by

$$\pm A_1^f (I_1^f)^2 + A_4^f I_4^f = 1 \quad . \quad (2.19)$$

Here the fiber constituent is defined by the superscript f , and any other numeric superscript represents a power. The remaining coefficients in Equation (2.19) are determined from experimental data. The actual derivations leading to numerical values for the coefficients are presented in detail within Chapter 5.

Most multiaxial loading conditions of composite materials result in matrix stress states in which off-axis stresses are comparable to those of the direction of loading, and thus substantial matrix stress interactions exist. The three-dimensional nature of the matrix stress field provides motivation for retaining terms $\pm A_1^m$, $\pm A_2^m$, and $\pm A_5^m$ that were discarded in the case of fiber failure. Realizing these arguments, the matrix failure criterion takes the form

$$\pm A_1^m (I_1^m)^2 - \pm A_2^m (I_2^m)^2 - \pm A_5^m I_1^m I_2^m + A_3^m I_3 + A_4^m I_4^m = 1 \quad , \quad (2.20)$$

where the superscript m represents the matrix constituent. Again, Chapter 5 details the numerical determination of these coefficients.

2.3 Nonlinear Matrix Material Behavior

As a composite material is loaded, nonlinear behavior is often observed due to inelastic deformation mechanisms occurring in the matrix constituent. Here, a brief discussion of nonlinear matrix behavior is presented along with its effect on a progressive failure analysis in a finite element setting.

2.3.1 Matrix Damage

When a composite is loaded, nonlinear matrix behavior initiates at loads far below ultimate failure in the form of submicrocrack (void) accumulation. By submicrocracks, we refer to voids developing in the matrix with length scales on the order of a 1 to 100 nanometers (Zhurkov, 1974). Eventually submicrocracks will accumulate to a critical

density and coalesce to form a macroscopic crack. Numerous excellent accounts of theoretical and experimental research on submicrocracking appear in the literature, and most may be traced to the pioneering work of Zhurkov (1965).

The effects of submicrocrack damage are most apparent in longitudinal shear, where a strong nonlinear response is observed far below ultimate failure. It is not uncommon to see nonlinearity begin at loads that are 20-25% of the ultimate load.

Damage in the matrix material also presents itself in the form of both longitudinal and transverse cracks through the thickness of individual plies in a laminate. Akula (2007) investigated the effects of both longitudinal and transverse cracking in laminates and compares experimental data for a variety of authors. From these comparisons, longitudinal cracking within a ply is found to have little effect on ply-level material properties, while transverse cracks lead to immediate failure of unidirectional composites, or significant reductions of ply-level matrix properties for multidirectional composite laminates.

2.3.2 Enforcing a Consistent Set of Material Characteristics

The discussion above is limited to damage occurring in the matrix constituent for both submicrocracking and transverse ply cracking. In an incremental finite element analysis, when the matrix material properties are updated as damage accumulates, the composite

properties must also be updated to enforce a consistent set of thermomechanical material properties at the micro and macro scale. Thus, when the MCT decomposition is performed for the next iteration, the stresses and strains computed at the constituent level are consistent with the current state of the material.

To compute the relationships between thermoelastic properties at the micro and macro scales, a finite element micromechanics model is utilized. The micromechanics model requires a geometric representation of the multi-continuum discussed in Section 2.1. To create such a model, a fiber packing arrangement is assumed, and a periodic unit cell, or representative volume element (RVE), is constructed representing the microstructure of the multi-continuum. Periodic multipoint constraints are employed along the boundary of the unit cell to force the model to behave as if it were a representation of the entire composite.

The relationships between matrix and composite material properties take the form of curves relating elastic constants. These curves may be completely developed for any material prior to structural analysis, thereby circumventing the need to perform a micromechanical analysis at each load step where nonlinear behavior occurs. Thus, the matrix material properties can be altered, and the current fiber and matrix properties can then be used to predict a new set of composite properties. The ability to connect composite and constituent properties through simple predefined curves is a critical aspect of the computational efficiency of an MCT progressive failure structural analysis.

2.4 Nonlinear Finite Element Implementation

To implement the MCT constituent-based progressive failure analysis into a finite element setting, an incremental analysis must be conducted to allow for nonlinear material behavior. Stresses and strains are updated at each increment, as are material properties for the composite and constituents. Here, a brief discussion of the finite element solution process is presented for a general nonlinear problem to give insight into solution techniques used within this work.

A typical solution algorithm for an incremental finite element analysis consists of approximating the material behavior of the system for the specified increment and performing iterations on the global system of equations to finally reach a converged state. Convergence is typically judged by comparing the work done by internal stresses within an element to nodal loads of external forces. If a residual force is too large, the solution is performed again using the residual nodal loads to update the displacement field. Iteration continues until the residual forces at each node are within a specified tolerance, and then the analysis resumes for the next increment.

In general, nonlinear material behavior usually “softens” as strains increase, as shown by the solid line in Figure 2.2. To capture this behavior at each increment in a finite element setting, an incremental solution using instantaneous “elastic properties” is used to approximate the stresses from the known strains for the desired increment. Keeping with

Figure 2.2, consider the i^{th} increment. The increment in stresses can be computed from the incremental strains using a tangent modulus, denoted by E_t . An alternate approach is to compute the total stress based on the total strains using a secant modulus, denoted by E_s . For the purposes of stability, a secant modulus approach is preferred because, as strain levels increase, the secant modulus is still a positive number much larger than zero. For the purposes of convergence, a tangent modulus approach is preferred as the rate of convergence is improved for a given load increment. However, if a tangent modulus is utilized, the modulus tends toward a zero slope when the material behavior begins to plateau, which adversely affects the stability of the solution. Furthermore, if the material behavior exhibits a drop in stress for elevated strains, as is typical of crack induced damage, the corresponding tangent modulus is negative. A negative tangent modulus results in serious stability issues in a load-based finite element solution algorithm.

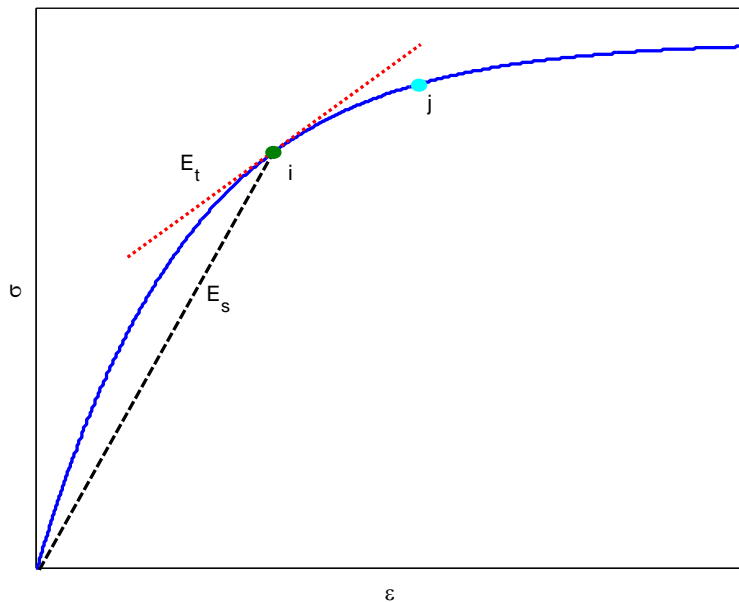


Figure 2.2 Nonlinear material behavior, and a representation of the tangent and secant moduli for the i^{th} increment.

However, if the tangent modulus begins to assume a zero or negative slope in a load driven finite element solution, stability can be improved by switching to a solution that is displacement driven. For the purposes of this work, a secant modulus is preferred as the majority of finite element problems encountered are load driven. Furthermore, a negative tangent modulus for an integration point in a multidirectional laminate does not necessarily mean the laminate is experiencing a large drop in stiffness. Thus, switching to a displacement driven solution from a load driven solution is considered a trying task for *multidirectional laminate* progressive failure predictions.

Many techniques exist to converge on a solution in a nonlinear analysis while minimizing computational costs. The choice of the technique depends on the nonlinearity of the material behavior and the size of the finite element model in question. In this work, the finite element models are quite small in the context of typical structural analysis problems. Thus, it is considered beneficial to reformulate the global equations at every increment to achieve rapid convergence. This technique is generally referred to as the full Newton method in a finite element setting, in accordance with ABAQUS documentation (2007).

2.5 Implementation Challenges

The MCT constituent-based failure analysis outlined in this chapter has been proven to compare very well with the vast majority of acquired experimental data. However, there exists the possibility for substantial improvements in the analysis for certain materials,

laminates, and load cases. These improvements include enhancing the micromechanics solution times to allow for embedding the micromechanics in a nonlinear structural problem. This capability may lead to more flexible degradation schemes that recognize advanced failure mechanisms at the constituent level.

An in-depth investigation of the effects of thermal residual stresses during curing is also of interest. To achieve this, the micromechanics analysis must be implemented with advanced viscoelastic material modeling capability to correctly model polymer behavior at elevated temperatures.

2.5.1 Enhanced Micromechanics Solution Times

As explained in Section 2.3, degraded composite properties are related through a micromechanics model to degraded matrix properties in order to enforce a consistent set of material properties across the geometric scales of a composite. The degradation schemes employed with the MCT constituent-based progressive failure analysis utilize known “material curves” for matrix degradation schemes, and are in fact limited to a special case of degradation. The choice to limit degradation schemes to those that may be quantified by material curves is due to the fact that predicting degradation “on the fly” is computationally inefficient as the micromechanics model would have to be employed for every increment, and every integration point, in an analysis. Solution times for the current micromechanics model are far too large to incorporate micromechanics in every time step of a nonlinear analysis.

In reality, matrix degradation may not generally result in material behavior that can be quantified by one or two material dependent curves, and thus being able to accommodate various degradation schemes within an analysis is desired. However, in order to accomplish such a feat, the micromechanics model solution times must be dramatically decreased to make such a coupled macro/micro analysis numerically feasible. Thus, an investigation of enhanced solution times of the micromechanics model is warranted, and further presented in Chapter 3 of this work.

2.5.2 Thermal Stresses

Another major challenge with the progressive failure analysis of composite structures is the unknown impact of thermal cure stresses on failure predictions. Typical composite materials undergo cure cycles during fabrication, where elevated temperatures are used to set the resin. When the temperature returns to ambient conditions, stresses develop in the fiber and matrix due to a mismatch in thermal expansion properties. The current approach to an MCT failure analysis is to assume both the fiber and matrix are at a stress free state before any mechanical or thermal loading occurs. An argument in support of this assumption is that all composite failure test data is taken at ambient temperatures. Thus, any residual stresses are assumed accounted for during strength testing as the constituent stresses at failure would inherently incorporate the thermal effects. While this argument seems to be well grounded, there has been no conclusive evidence to support the claim due to large difficulties in predicting constituent level stresses for a cure cycle.

In order to thoroughly investigate the effects of a cure cycle on failure predications, an advanced constitutive model for the polymer matrix must be developed to accommodate time and temperature-dependent material behavior. An appropriate constitutive law for polymers at elevated temperatures is one of viscoelasticity, incorporating time-temperature superposition (TTS). Implementing such a constitutive law requires experimentally determining material data at a range of temperatures the polymer matrix is expected to encounter. In practice, the availability of such material data is virtually nonexistent, as viscoelastic data for most materials is usually taken at a single temperature. However, Seifert (2002) provides temperature-dependent creep data for Derakane 510, a vinylester polymer used as a matrix material in U.S. Navy composite materials. We use the viscoelastic data acquired for Derakane 510 to study the effects of thermally induced cure stresses on composite failure.

Numerical implementation of the TTS algorithm in the micromechanics analysis requires the creation of an incremental finite element routine that incorporates the viscoelastic effects of the material properties at each integration point. Chapters 4 and 5 detail this analysis and further examine the effects of thermal stresses arising from cure cycles on failure predictions.

Also, increasing numbers of composite materials are being utilized for cryogenic environments. Fuel tanks containing cryogenic liquids for aerospace applications are a

prime example. The effects of large temperature changes on composite failure are largely unknown, and experimental data for such environments is sparse. A major difficulty in modeling the effects of thermal loads at the structural level is that traditional analysis techniques cannot capture the large thermally induced constituent stresses, as they are self-equilibrating and hence do not alter the composite stress field. A huge advantage to an MCT analysis is the fact that any thermal loading is completely captured in the constituents, and thus any failure predictions at the constituent level inherently contain the constituent stresses resulting from temperature changes. Constituent stress information presents a large opportunity to conduct a detailed analysis on failure predictions of composite laminates placed in cryogenic environments, as discussed in detail within Chapter 5.

2.5.3 Orthotropic Degradation

A critical deformation mechanism to model in progressive failure analysis of composite materials is the formation of transverse cracks and the effect of transverse crack density on composite stiffness properties. Currently, the transverse stiffness and transverse shear stiffness of the composite and matrix are degraded in a manner that is consistent with transversely isotropic material behavior. Akula (2007) investigated the influence of transverse cracking on the material properties of individual lamina with a finite element micromechanics model to deduce that transverse cracking causes orthotropic degradation of the damaged plies. Chapter 6 details an investigation of orthotropic degradation schemes employed to model material behavior in the presence of transverse cracks in accordance with the work of Akula.

3. ENHANCING MICROMECHANICS SOLUTION SPEED

3.1 Micromechanics Model

MCT relies on composite and constituent thermoelastic material properties when decomposing the macroscopic stress and strain fields to those of the constituents. A critical aspect of the MCT decomposition is the development of a *consistent* set of thermoelastic properties linking the composite and the constituents. To achieve this consistency, given thermoelastic properties for the fiber and matrix, a finite element micromechanics model is utilized to generate composite material properties.

In general, computing a set of composite thermoelastic material properties for use in a linear analysis is a trivial matter using the micromechanics model. However, when constituent material properties need to be continuously updated in a nonlinear analysis, composite material properties must also be continuously updated. For a computationally efficient analysis, the composite material properties must be updated as quickly as possible. It is therefore desirable to have a micromechanics model capable of generating composite material properties extremely efficiently as the analysis progresses.

The micromechanics model used in this thesis is based on the assumption of uniform hexagonal packing of a unidirectional lamina as shown in Figure 3.1.

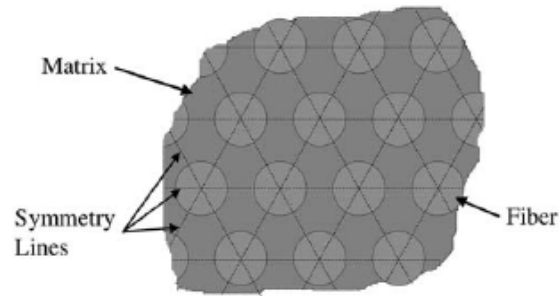


Figure 3.1 Idealized uniform hexagonal packing representation for a unidirectional composite (Garnich, 1996).

Following the work of Garnich (1996), a triangular unit cell can be extracted from the hexagonal packing as shown in Figure 3.2. The fiber volume fraction is utilized to determine the geometric parameters, and constraints are applied to enforce the periodicity of the repeating boundaries.

The most general class of materials considered here-in is that of orthotropic behavior of the matrix and transverse isotropy of the fibers. Orthotropic matrix behavior is the result of degradation schemes to model various levels of matrix damage. For orthotropic matrix behavior, the resulting composite is orthotropic as well. In the case of orthotropy, nine independent elastic constants must be determined along with three independent coefficients of thermal expansion (CTE). A total of six independent mechanical load cases are necessary to apply to the micromechanics model to obtain the nine orthotropic material constants for a composite material. A single thermal load is sufficient to calculate the three composite CTE.

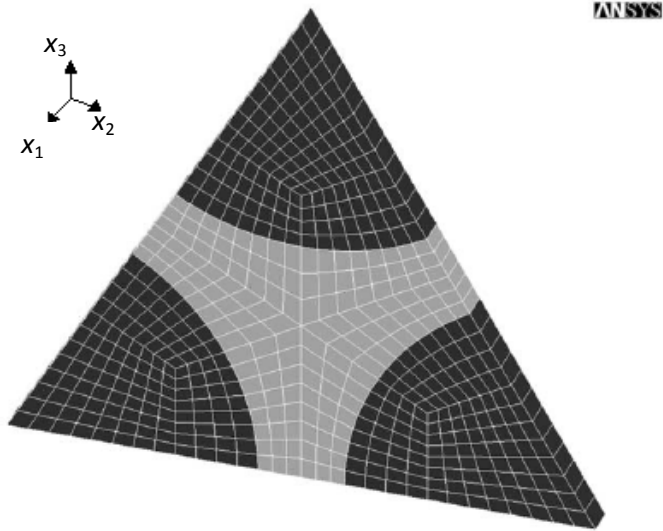


Figure 3.2 ANSYS periodic unit cell and finite element mesh from Garnich (1996).

A common approach to computing the *composite* stress and strain fields for a given thermomechanical load is to volume average the respective fields over the unit cell. In particular, recall the definition of stress at a point given by

$$\bar{\sigma} = \frac{1}{V} \int_D \tilde{\sigma}(x) dV \quad . \quad (3.1)$$

In terms of a finite element formulation, volume averaging is achieved by summing the stresses and strains in each element multiplied by the respective element volume. However, the stress and strain fields within each element are also spatially variable. The average *element* stresses and strains are obtained by calculating the stresses and strains at integration (Gauss) points and multiplying these values by the volume fraction associated with the respective integration points. The volume of the element can simply be approximated as the sum of the Jacobians at the elemental integration points (Cook *et.*

al., 1974). In this manner, the volume averaged stresses and strains can be approximated for the composite as

$$\tilde{\sigma} = \frac{1}{V} \sum_{i=1}^e \sum_{k=1}^{n_{int}} \tilde{\sigma}_k J_k W_k \quad , \quad (3.2)$$

where e is the number of elements, n_{int} is the number of integration points within the element, J_k is the Jacobian of the integration point, W_k is the weighting factor employed by Gauss quadrature, and V is the total volume of the model.

3.2 ABAQUS Micromechanics Solution

In the period since 1996, University of Wyoming (UW) researchers have migrated from ANSYS to ABAQUS as a commercial code for research. An ABAQUS micromechanics model, patterned after Garnich's (1996) model, has been previously developed to generate composite material properties. The standard mesh for a 60% fiber volume fraction using this model is shown in Figure 3.3.

The model incorporates 578 nodes and 255 fully integrated isoperimetric brick elements, and the element stresses and strains are volume averaged in a post-processing subroutine that is linked with ABAQUS. Given this model, along with fully implemented multipoint constraints that enforce periodicity, the mean wall-clock time to generate composite material properties is approximately 4.0 seconds. The hardware used to generate the material properties was a personal desktop computer using a hyper-threaded Intel® Dual Core Xeon processor with 3.0 GB of RAM and a clock speed of 3.2 GHz.

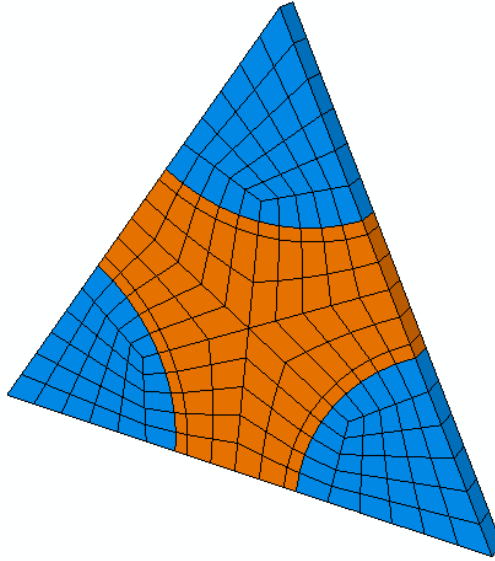


Figure 3.3 ABAQUS standard mesh for a 60% fiber volume fraction.

3.3 The Search for Computational Speed

In the search to speed up solutions of the micromechanics model, several techniques, both simple and complex, were used to reduce the total number of equations that needed to be solved. First and foremost, a mesh density analysis was conducted on the ABAQUS micromechanics model to obtain the optimized number of nodes while still generating accurate material properties. After a convergence study was completed with the ABAQUS model, the geometry, constraint equations, and load conditions were ported to an in-house finite element code developed at UW. Multiple highly model-specific numerical algorithms were then implemented to optimize performance.

3.3.1 Mesh Density Analysis

The standard mesh of Figure 3.3 used to develop composite material properties consists of 578 nodes, resulting in 2,517 equations after implementing the necessary multipoint

constraint equations. A mesh density analysis was conducted, with the standard mesh used as a baseline, to determine the minimum number of nodes required to retain the accuracy of the calculated macroscopic material properties. It was determined that for a fiber volume fraction of 60%, the nodes could be reduced from 578 to 242 while retaining material property convergence to within 0.5% of the standard model. The optimized mesh is depicted in Figure 3.4, and a comparison of volume averaged mechanical material properties for a carbon/epoxy composite with a fiber volume fraction of 60% is given in Table 3.1.

The progressive failure analysis developed in this thesis requires one to compute “damaged” composite properties based on degraded matrix properties. Therefore, similar results to those shown in Table 3.1 were computed for a range of degraded matrix properties to ensure convergence of the solutions. In all cases examined, material properties of the optimized mesh of Figure 3.4 were within 0.5% of those computed using the baseline mesh of Figure 3.3.

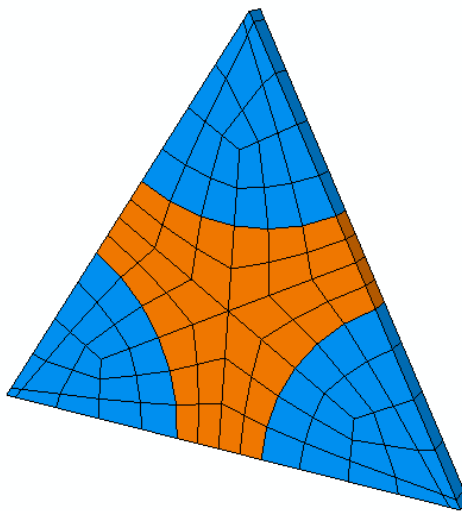


Figure 3.4 Optimized mesh for a 60% fiber volume fraction.

Table 3.1 Composite material property comparison for a T300/BSL914C carbon/epoxy with a 60% fiber volume fraction.

Carbon T300 Fiber Material Properties					
Young's Modulus	<i>GPa</i>	Poisson Ratio		Shear Modulus	<i>GPa</i>
E_1	227.0	ν_{12}	0.2450	G_{12}	28.00
E_2	25.00			G_{23}	9.500
BSL914C Epoxy Matrix Properties					
Young's Modulus	<i>GPa</i>	Poisson Ratio		Shear Modulus	<i>GPa</i>
E	4.500	ν	0.3400	G	1.679
Original Mesh Volume Averaged Composite Properties					
Young's Modulus	<i>GPa</i>	Poisson Ratio		Shear Modulus	<i>GPa</i>
E_1	138.0	ν_{12}	0.2790	G_{12}	5.520
E_2	11.30			G_{23}	3.990
Optimized Mesh Volume Averaged Composite Properties					
Young's Modulus	<i>GPa</i>	Poisson Ratio		Shear Modulus	<i>GPa</i>
E_1	137.7	ν_{12}	0.2790	G_{12}	5.495
E_2	11.25			G_{23}	3.986
% Difference					
Young's Modulus	%	Poisson Ratio	%	Shear Modulus	%
E_1	0.2170	ν_{12}	0.1080	G_{12}	0.4530
E_2	0.4430			G_{23}	0.1000

The optimized mesh reduces the total number of linear algebraic equations in the micromechanics model from 2,517 to 1,149, which is a decrease of over a factor of two from the standard mesh. Wall-clock solution times within ABAQUS dropped from 4.0 seconds to approximately 2.0 seconds. While the drop in solution times through mesh optimization is unimpressive, the reduction in the total number of equations is a critical step in the search for speed in the in-house code.

3.3.2 Composite (Volume Averaged) Stress and Strain Calculation

As discussed in Section 3.1, the stresses and strains of the micromechanics model can be volume averaged to determine the macroscopic stress/strain fields of the composite. The

process of volume averaging must be repeated for seven different load cases to fully characterize the thermoelastic properties of the composite. This process is obviously a significant factor in the total calculation time of composite material properties as the stresses and strains at every integration point must be computed as a post-processing operation after solution of the displacements. Volume averaging of these fields is then achieved using equations of the form of Equation (3.2).

An alternate approach to volume averaging the stress and strain fields is to determine the macroscopic quantities based on the nodal values of the corners of the micromechanics model. As a related example, consider a constant strain triangle in a finite element setting, where the strains are calculated solely from the corner node displacements. An outline of the procedure to calculate the composite strains from the corner node displacements of the micromechanics model can be found in Appendices B and C. The use of nodal forces and displacements to determine composite stress/strain fields eliminates a vast set of floating point operations in a material property calculation.

3.3.3 Implementation of Constraint Equations

When linear multipoint constraint equations are implemented in a general conventional finite element analysis, the equations are typically added to the end of the stiffness matrix by the use of Lagrange multipliers. This technique is utilized in commercial codes as it is readily implemented for any general problem. However, while practical for broad functionality, the Lagrange multiplier method is computationally inefficient as it increases the total number of equations to be solved.

Although model specific, constraint equations can also be used to eliminate degrees of freedom from the stiffness matrix instead of adding equations, thereby reducing the numerical effort of solving the problem. Because the micromechanics model is specific to that of the hexagonally packed unit cell, it is computationally efficient to use the periodic constraint equations to eliminate degrees of freedom from the stiffness matrix. Curiskis (1978) presents a detailed explanation of the algorithm required to eliminate the nodal degrees of freedom for a generalized set of linear constraint equations.

3.3.4 Static Condensation

Static condensation is a technique employed to “condense” nodal degrees of freedom from a finite element mesh in order to reduce the size of the global system of equations. In particular, nodes residing in the interior of a mesh can be removed by “passing” the effect of the node to the nodes on the boundary of the mesh. This routine is exact in the sense of correctly capturing the global response of the full mesh, and can potentially reduce the size of the global stiffness matrix tremendously. Thus, when a majority of the nodes reside on the interior of a mesh, a significant enhancement of solution speed can be obtained when solving the global system of equations. Static condensation eliminates the ability to compute micromechanical stress and strain fields, but the need for such information has been eliminated as described in Section 3.3.2.

Observing Figure 3.4, it can be easily seen that the hexagonally packed unit cell can be reduced further to three symmetric portions as shown in Figure 3.5. It is extremely

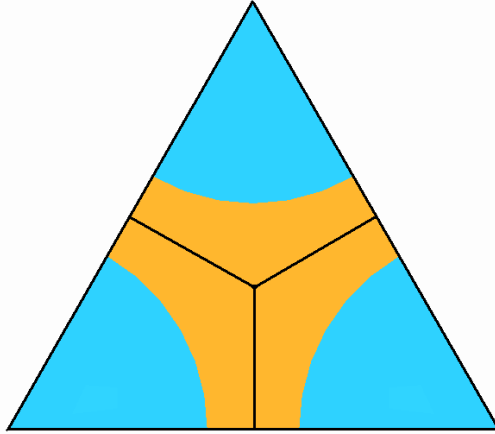


Figure 3.5 Symmetric partitioned mesh for a fiber volume fraction of 60%.

advantageous to utilize symmetry in conjunction with static condensation. In particular, the fiber and matrix can be statically condensed in each symmetric volume, resulting in three fiber super-elements and three matrix super-elements.

Static condensation utilizes Gaussian elimination to condense out the interior nodal degrees of freedom in a super-element. Wilson (1973) outlines the approach for an arbitrary stiffness matrix and load vector. The nature of this process requires numbering nodes in a manner such that any degrees-of-freedom to be condensed out are placed at the bottom of the solution vector.

3.3.5 Finite Element Matrix Operations

Inherent with any finite element solid mechanics solution is the formulation of element stiffness matrices and load vectors for assemblage into the global stiffness matrix and load vector. The development of these matrices requires large quantities of matrix

multiplications and the corresponding floating point operations. Specifically, consider the local element stiffness matrix formulation in matrix notation, given by

$$[K_e] = \int_V [B]^T [C] [B] dV , \quad (3.3)$$

where $[B]$ is the strain-displacement matrix and $[C]$ is the material stiffness matrix. For an 8-node, three-dimensional isoparametric element used for this analysis the $[B]$ matrix size is 6×24 while the $[C]$ matrix is 6×6 .

The geometric nature of the hexagonal micromechanics model is one where the material principal axes are aligned with the global coordinate system. Therefore, restricting the most general case of anisotropy to orthotropic behavior, the $[C]$ matrix can be partitioned as

$$[C] = \begin{bmatrix} C_{11} & 0 \\ 0 & C_{22} \end{bmatrix} , \quad (3.4)$$

where C_{11} and C_{22} are 3×3 matrices. Similarly, the strain-displacement matrix may be partitioned as

$$[B] = \begin{bmatrix} B_{11} \\ B_{21} \end{bmatrix} , \quad (3.5)$$

and B_{11} and B_{21} can be further partitioned as

$$B_{11} = [B_{11}^1 \ B_{11}^2 \ B_{11}^3 \ B_{11}^4 \ B_{11}^5 \ B_{11}^6 \ B_{11}^7 \ B_{11}^8] , \quad (3.6)$$

and

$$B_{21} = [B_{21}^1 \ B_{21}^2 \ B_{21}^3 \ B_{21}^4 \ B_{21}^5 \ B_{21}^6 \ B_{21}^7 \ B_{21}^8] , \quad (3.7)$$

respectively, where B_{21}^i and B_{11}^i are now 3×3 matrices. Substituting Equations (3.4-3.7) into Equation (3.3) results in

$$[K_e] = \int_V \begin{bmatrix} B_{11}^{1T} & B_{21}^{1T} \\ \vdots & \vdots \\ B_{11}^{8T} & B_{21}^{8T} \end{bmatrix} \begin{bmatrix} C_{11} & 0 \\ 0 & C_{22} \end{bmatrix} \begin{bmatrix} B_{11}^1 & \cdots & B_{11}^8 \\ B_{21}^1 & \cdots & B_{21}^8 \end{bmatrix} dV. \quad (3.8)$$

Then, carrying out the matrix multiplications yields

$$[K_e] = \int_V \begin{bmatrix} B_{11}^{1T} C_{11} B_{11}^1 + B_{21}^{1T} C_{22} B_{21}^1 & \cdots & B_{11}^{1T} C_{11} B_{11}^8 + B_{21}^{1T} C_{22} B_{21}^8 \\ \vdots & \ddots & \vdots \\ B_{11}^{8T} C_{11} B_{11}^1 + B_{21}^{8T} C_{22} B_{21}^1 & \cdots & B_{11}^{8T} C_{11} B_{11}^8 + B_{21}^{8T} C_{22} B_{21}^8 \end{bmatrix} dV. \quad (3.9)$$

The zero terms of the partitioned stiffness matrix are completely ignored in the above matrix equation, thereby eliminating half of the matrix multiplications. Appendix A details additional manipulations of the stiffness matrix of Equation (3.9) to further reduce the number of multiplications involved when encountering zeros within the individual 3×3 partitioned matrices.

Now consider the formulation of any arbitrary element load vector defined as

$$\{F_e\} = \int_V [B]^T [C] \{Z\} dV, \quad (3.10)$$

where $\{Z\}$ represents an arbitrary dimensionless strain vector. For the analysis considered here, $\{Z\}$ may represent strains produced from thermal loads or viscoelastic creep. If $\{Z\}$ is partitioned as

$$\{Z\} = \begin{Bmatrix} Z_{11} \\ Z_{21} \end{Bmatrix},$$

the procedure outlined above for the element stiffness matrix can be employed in the same manner to give a load vector as

$$\{F_e\} = \int_V \left\{ \begin{array}{c} B_{11}^{1T} C_{11} Z_{11} + B_{21}^{1T} C_{22} Z_{22} \\ \vdots \\ B_{11}^{8T} C_{11} Z_{11} + B_{21}^{8T} C_{22} Z_{22} \end{array} \right\} dV . \quad (3.11)$$

Again, a detailed derivation of the load vector computation is outlined in Appendix A. Numerical integration using Gauss quadrature is then employed to evaluate the integrals of Equations (3.9) and (3.11).

As discussed previously, the hexagonal periodic unit cell can be broken into three symmetric portions as shown in Figure 3.5. To exploit the symmetries, one symmetric region could be rotated about the longitudinal axis passing through the centroid of the unit cell by positive or negative 120 degrees to define the other two symmetric regions.

Consider the micromechanics model of Figure 3.4 with the x_1 direction orientated with the longitudinal axis. Now, consider a coordinate array for a node given by

$$\{x\} = [x_1 \quad x_2 \quad x_3]^T . \quad (3.12)$$

For a two-dimensional rotation of these coordinates about the longitudinal direction as shown in Figure 3.6, the rotation matrix is given by

$$[\alpha] = \begin{bmatrix} 1 & 0 & 0 \\ 0 & \cos(x_2, \bar{x}_2) & \cos(x_2, \bar{x}_3) \\ 0 & \cos(x_3, \bar{x}_2) & \cos(x_3, \bar{x}_3) \end{bmatrix} , \quad (3.13)$$

where the overbar represents the transformed coordinate system.

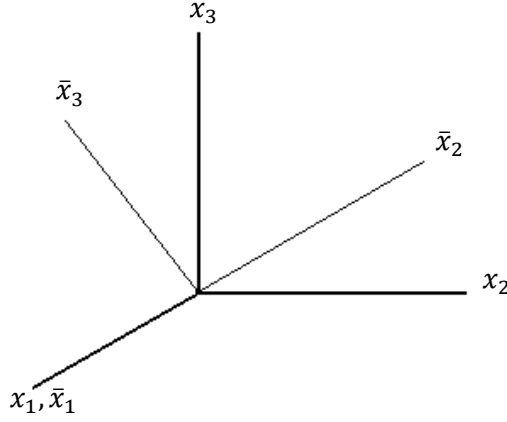


Figure 3.6 Rotated coordinate axes about the longitudinal axis.

For a rotation of 120 degrees, the rotation matrix becomes

$$[\alpha] = \begin{bmatrix} 1 & 0 & 0 \\ 0 & -\frac{1}{2} & -\frac{\sqrt{3}}{2} \\ 0 & \frac{\sqrt{3}}{2} & -\frac{1}{2} \end{bmatrix} . \quad (3.14)$$

The coordinate transform of the vector of Equation (3.12) is given by $\{\bar{x}\} = [\alpha]^T \{x\}$, or

$$\{\bar{x}\} = \begin{bmatrix} 1 & 0 & 0 \\ 0 & -\frac{1}{2} & \frac{\sqrt{3}}{2} \\ 0 & -\frac{\sqrt{3}}{2} & -\frac{1}{2} \end{bmatrix} \begin{Bmatrix} x_1 \\ x_2 \\ x_3 \end{Bmatrix} , \quad (3.15)$$

which is simply

$$\{\bar{x}\} = \begin{Bmatrix} x_1 \\ -\frac{x_2}{2} + \frac{\sqrt{3}}{2}x_3 \\ -\frac{\sqrt{3}}{2}x_2 - \frac{x_3}{2} \end{Bmatrix} . \quad (3.16)$$

Given the transformed coordinates for a symmetry section, the formulation of the element equations proceeds identically to the original (master) section. Finally, to complete the element formulation of the entire model, an identical procedure to that outlined above is employed for the section requiring a -120 degree rotation.

3.4 Implementation

The various numerical techniques outlined in this chapter were implemented in an in-house finite element code developed at the University of Wyoming. The code was purposely limited to only accommodate the hexagonally packed micromechanics model discussed in this work. Code specificity is necessary to implement many of the numerical techniques aimed at computational efficiency.

The program first calculates the nodal coordinates and connectivity for one symmetric portion of the mesh in conjunction with the mesh density analysis detailed in Section 3.3.1. Specific node numbering is introduced to accommodate static condensation routines for the entire model. In particular, node numbering of nodes retained after static condensation is performed in increments of 3. This numbering scheme allows the other two symmetric regions to have nodes numbered as 1 or 2 plus the node number of the master super-element as shown in Figure 3.7. Consequently, the global assembly of the rotated matrices is straightforward.

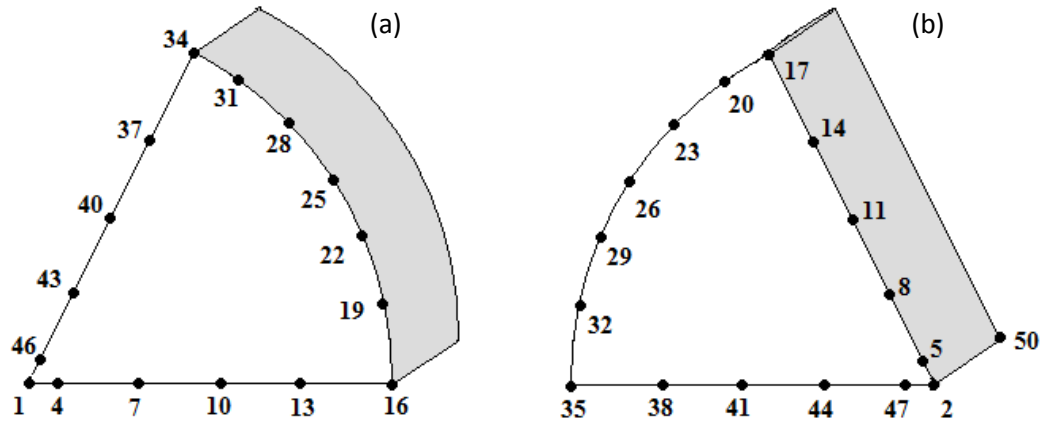


Figure 3.7 Representation of global node numbering for (a) the master fiber super-element and (b) a fiber super-element rotated 120° about the longitudinal axis of the unit cell centroid.

A fiber super-element with a fiber volume fraction of 60% is shown in Figure 3.8 (a). The back face nodes must be condensed first by employing the periodic constraint equations described by Garnich (1996) and utilizing the algorithm detailed in the work of Curiskis (1978). All nodes on the back face are eliminated with the exception of a single node on the back bottom-left corner. The front face interior nodes can then be statically condensed using the algorithm of Wilson (1973) to form the completed fiber super-element shown in Figure 3.8 (b).

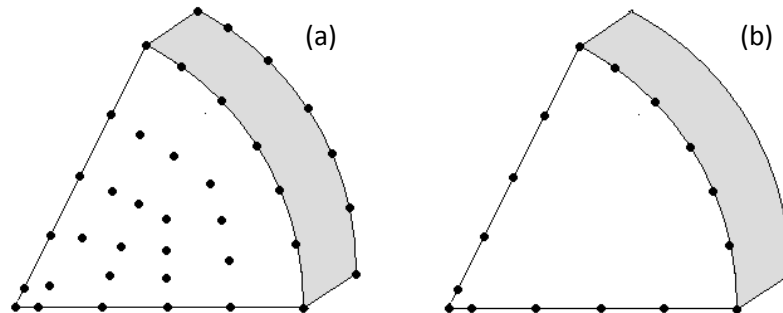


Figure 3.8 Node representation for a fiber volume fraction of 60% for (a) the uncondensed super-element and (b) the condensed super-element. Note some back face nodes are hidden in (a), and the back face corner node is hidden in (b).

The matrix super-elements are formed in a similar matter to the fiber, except the constraint equations utilize different nodes for elimination. A matrix super-element before and after construction is shown in Figure 3.9 (a) and 3.9 (b), respectively.

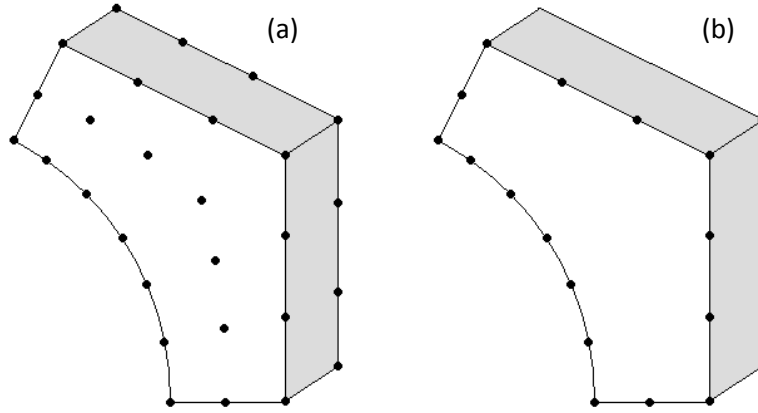


Figure 3.9 Matrix node representation for a fiber volume fraction of 60% for (a) the uncondensed super-element and (b) the condensed matrix super-element. Note some back face nodes are hidden in (a).

Again, a single back-face node remains in the condensed super-element as shown in Figure 3.9 (b). Note for all super-element constructions, the front-face boundary nodes must be kept because other super-elements share these boundaries. Hence, the nodal degrees of freedom on these boundaries effectively tie the entire model together.

After the fiber and matrix super-element stiffness matrices and load vectors are assembled into the global system, several nodes residing on the exterior unit cell boundary are condensed with the remaining periodic constraint equations as outlined in Garnich (1996). Finally, the nodes residing on the back bottom corners and unit cell centroid (Figures 3.8 and 3.9) leftover from the super-element construction are condensed in the same manner. Note, however, the node residing on the top corner of the back face must be retained to constrain the model from rigid body motion.

Finally, before the system of global equations is solved, a renumbering algorithm is employed on the remaining nodes and super-element connectivities as detailed by Sloan (1986). This renumbering process reduces the bandwidth of the global stiffness matrix, thereby further increasing the efficiency of the global stiffness matrix decomposition.

The thermoelastic material properties of a unidirectional composite lamina are generated by forming a load vector for each of six mechanical load cases, and one additional thermal load. The specific mechanical loads are developed in Appendix C. The LU decomposition and back-substitution algorithms employed for linear equation solution are detailed by Press *et. al.* (2007). An important feature of this solution process is that all load cases may be solved using a single factorized stiffness matrix.

The importance of static condensation to solution speed in a progressive failure analysis lies in the assumed material behavior of the fibers. In particular, because the fibers are assumed linearly elastic to failure and do not degrade during a progressive failure analysis, the fiber super-elements need only be formulated once for any specific composite lamina. Moreover, typical fiber volume fractions for high performance composites are on the order of 60%. These features collectively allow one to make significant and permanent reductions in model size.

In contrast to the fibers, static condensation of the matrix super-elements provides less computational benefit. As the matrix material degrades, static condensation must be

implemented at each stage of the degradation process to form the degraded composite material properties. Minor computational savings are achieved by solving the smaller problem three times for each of the super-elements, as opposed to one large solution of all the elements that discretize the matrix.

3.5 Results

Solely by conducting a mesh density analysis with ABAQUS, the total number of equations in the micromechanics model was reduced from 2,517 to 1,149, and the analysis time was cut in half. By following the various numerical efficiency techniques outlined in this chapter, the micromechanics model was further reduced to a remarkable 132 total equations. Wall-clock solution times of fewer than three milliseconds were achieved for the generation of orthotropic material properties, representing a solution speed-up of 3 orders of magnitude over the original ABAQUS model. Moreover, because the fiber super-element stiffness matrices are formed only once, each subsequent call to the hexagonal micromechanics material module led to wall-clock solution times for composite properties of under one millisecond with convergence of material properties within 0.5%.

4. CURE STRESS ANALYSIS

The fabrication process for composite materials varies widely for different fiber/matrix combinations. Inherent in most of these processes is the setting of the resin at elevated temperatures to ensure complete bonding between the fiber and matrix. The process of starting the material at an elevated temperature and eventually reaching a base reference temperature is known as curing. Typical cure cycles involve starting the composite material at a specified temperature and pressure, imposing a prescribed temperature and pressure history, and finally bringing the temperature and pressure to ambient conditions.

Even though the *composite* is at a stress-free state at any temperature for which the structure is not constrained, the constituents of a unidirectional lamina have self-equilibrating residual stresses occurring from thermal strains induced by mismatched coefficients of thermal expansion. It is of particular interest to focus on the residual stresses residing within the matrix during a cure cycle, as they can become very large compared to ultimate strengths and therefore have a dramatic effect on failure predictions.

At elevated temperatures, the resin has very low stiffness and flows freely. As the temperature decreases, the material stiffness of the resin grows and consequently increases the stress interaction between the fiber and matrix. Polymer matrix resins also tend to exhibit a fading memory under thermomechanical loads. Consequently, a reasonable constitutive model to account for the time-temperature behavior of neat resins

is to treat the resin as a linear viscoelastic material with time and temperature dependent material properties.

4.1 Linear Viscoelasticity

Viscoelastic materials are defined as those which exhibit a combination of both solid and fluid like behavior and are often referred to as having an imperfect memory. Specifically, they have a tendency to not return to an undeformed state when a mechanical load is removed. Because the theory of linear viscoelasticity is based upon linear superposition of stress and strain fields, the concept of volume averaging can readily be extended to a linear viscoelastic analysis, and the micromechanics model developed in Chapter 3 can be employed to calculate constituent and composite level stresses and strains. The term linearity used here may be expressed through a general constitutive law as

$$\begin{aligned} \sigma(t) &= \int_{s=0}^{\infty} G(\mu\varepsilon_1(t-s) + \beta\varepsilon_2(t-s)) = \\ &\mu \left[\int_{s=0}^{\infty} G(\varepsilon_1(t-s)) \right] + \beta \left[\int_{s=0}^{\infty} G(\varepsilon_2(t-s)) \right] \end{aligned} \quad (4.1)$$

$$\mu, \beta \in \mathbb{R} \quad ,$$

where G is a function of the strain field and the subscripts on ε illustrate different strain histories.

A one-dimensional theory of linear viscoelasticity begins with the development of the creep compliance. For a constant stress, σ_0 , applied under isothermal loading, the creep compliance is defined as

$$D(t) = \frac{\epsilon(t)}{\sigma_0} , \quad (4.2)$$

(Lakes, 1999). Figures 4.1 and 4.2 illustrate the applied stress and a typical creep compliance response for a viscoelastic polymer.

By direct analogy to linear elasticity, a three-dimensional creep compliance matrix can be formed that completely describes the multiaxial material behavior. Following the derivation of Lakes (1999), linear superposition can be used to model a given stress history and non-constant temperature history, and a hereditary integral for the strain in three-dimensional space can be formed as

$$\epsilon_i(t) = \sum_{j=1}^6 \int_{0^-}^t \frac{d\sigma_j}{d\tau} D_{ij}(t - \tau) d\tau + \int_{0^-}^t \frac{d\theta}{d\tau} \alpha_i(t - \tau) d\tau , \quad (4.3)$$

where $D_{ij}(t)$ is the material compliance matrix, $\sigma_j(t)$ is the applied stress, $\theta(t)$ is a known temperature history, and α_i is the matrix thermal expansion coefficient vector.

For the scope of this work, the thermal expansion vector is assumed to be constant for all time and temperatures, giving

$$\epsilon_i(t) = \sum_{j=1}^6 \int_{0^-}^t \frac{d\sigma_j}{d\tau} D_{ij}(t - \tau) d\tau + \alpha_i \theta(t) . \quad (4.4)$$

The creep compliance functions $D_{ij}(t)$ are assumed to take the mathematical form of exponential functions as

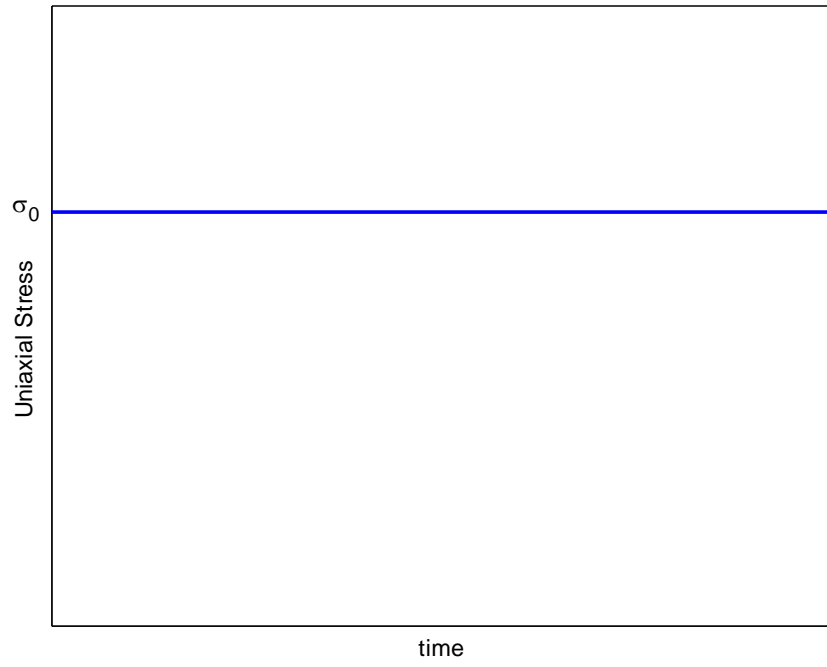


Figure 4.1 Constant applied stress for an isothermal loading.

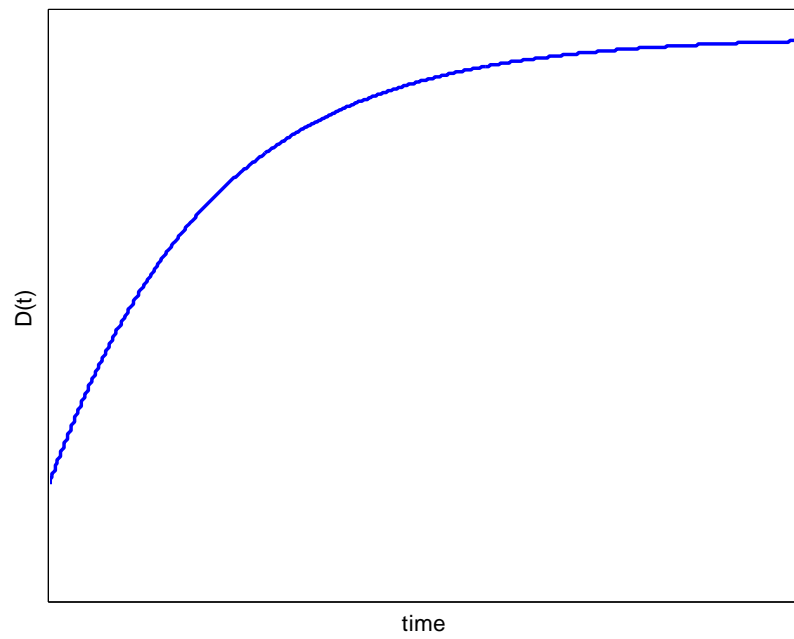


Figure 4.2 Creep compliance resulting from a strain history cause by an applied stress, σ_0 .

$$D_{ij}(t) = D_{ij}^0 + \sum_{L=1}^N D_{ij}^L \exp\left(\frac{-t}{\overline{\Pi}_{ij}^L}\right) , \quad (4.5)$$

where $\overline{\Pi}_{ij}^L$ denotes time constants associated with each exponential term and N is the number of exponential terms required to model the material behavior as a function of time (Lakes, 1999). The work within this chapter focuses on a purely isotropic matrix, giving the material compliance matrix as

$$D_{ij}(t) = \begin{bmatrix} D_{11}(t) & D_{12}(t) & D_{12}(t) & 0 & 0 & 0 \\ D_{12}(t) & D_{11}(t) & D_{12}(t) & 0 & 0 & 0 \\ D_{12}(t) & D_{12}(t) & D_{11}(t) & 0 & 0 & 0 \\ 0 & 0 & 0 & D_{44}(t) & 0 & 0 \\ 0 & 0 & 0 & 0 & D_{44}(t) & 0 \\ 0 & 0 & 0 & 0 & 0 & D_{44}(t) \end{bmatrix} , \quad (4.6)$$

where

$$D_{44}(t) = 2[D_{11}(t) - D_{12}(t)] . \quad (4.7)$$

Hence, the three-dimensional compliance matrix is completely characterized by two functions, $D_{11}(t)$ and $D_{12}(t)$, respectively.

An additional simplification of Equations (4.6) and (4.7) is achieved by assuming the viscoelastic material has a constant bulk modulus, K . In this case, $D_{12}(t)$ may be expressed in terms of $D_{11}(t)$ and K as

$$D_{12}(t) = \frac{1}{2} \left[\frac{1}{3K} - D_{11}(t) \right] . \quad (4.8)$$

Equations (4.6 - 4.8) then provide a complete description of a three-dimensional viscoelastic compliance matrix in terms of a single uniaxial creep function given by $D_{11}(t)$.

To model a viscoelastic material in a finite element sense, the constitutive law of Equation (4.4) must be approximated in an incremental form. Consider an increment in time from n to $n+1$ and define $\Delta t = t_{n+1} - t_n$. Following the work of Garnich and Hansen (1997) an incremental solution of the hereditary integral begins by writing

$$\Delta \epsilon_i = \epsilon_i(t_{n+1}) - \epsilon_i(t_n) \quad , \quad (4.9)$$

or

$$\Delta \epsilon_i = \sum_{j=1}^6 \left[\int_{0^-}^{t_{n+1}} D_{ij}(t_{n+1} - \tau) \frac{d\sigma_j}{d\tau} d\tau - \int_{0^-}^{t_n} D_{ij}(t_n - \tau) \frac{d\sigma_j}{d\tau} d\tau \right] + \alpha_i \Delta \theta \quad . \quad (4.10)$$

For clarity, denote the integral difference pair (IDP) in square brackets as

$$\Delta I_i = \sum_{j=1}^6 \left[\int_{0^-}^{t_{n+1}} D_{ij}(t_{n+1} - \tau) \frac{d\sigma_j}{d\tau} d\tau - \int_{0^-}^{t_n} D_{ij}(t_n - \tau) \frac{d\sigma_j}{d\tau} d\tau \right] \quad . \quad (4.11)$$

An approximate solution to the IDP of Equation (4.11) is achieved by requiring the time step to be sufficiently small so that $\frac{d\sigma_j}{d\tau}$ is well approximated as constant and given by $\frac{\Delta\sigma_j}{\Delta t}$. Noting Equation (4.5), the integrals of Equation (4.11) may then be evaluated explicitly to give

$$\Delta I_i = \sum_{j=1}^6 \left[D_{ij}^0 \Delta \sigma_j + \sum_{L=1}^N \left(1 - \exp\left(\frac{-\Delta t}{\Pi_{ij}^L}\right) \right) \left(D_{ij}^L \Pi_{ij}^L \frac{\Delta \sigma_j}{\Delta t} - P_{ij}^L(t_n) \right) \right] \quad , \quad (4.12)$$

where

$$P_{ij}^L(t_{n+1}) = P_{ij}^L(t_n) \exp\left(\frac{-\Delta t}{\Pi_{ij}^L}\right) + D_{ij}^L \Pi_{ij}^L \frac{\Delta \sigma_j}{\Delta t} \left(1 - \exp\left(\frac{-\Delta t}{\Pi_{ij}^L}\right)\right) , \quad (4.13)$$

and $P_{ij}^L(0^-) = 0$. A detailed development of Equations (4.12) through (4.13) is found in Garnich (1996).

Note that singularities in the form of finite jumps in stress are possible at $t = 0$. For this situation, the response from $t = 0^-$ to $t = 0^+$ is elastic and Garnich (1996) has shown

$$P_{ij}^L(0^+) = D_{ij}^L \sigma_{ij}(0^+) . \quad (4.14)$$

In the above, as in the entire development of this section, there is no implied summation.

The strains generated by the IDP of Equation (4.12) arise from two distinctly different contributions consisting of terms involving the stress increment $\Delta \sigma_j$ and terms independent of $\Delta \sigma_j$. We identify terms independent of $\Delta \sigma_j$ as “flow strains” and write

$$\Delta \epsilon_i^f = \sum_{j=1}^6 \sum_{L=1}^N \left(\exp\left(\frac{-\Delta t}{\Pi_{ij}^L}\right) - 1 \right) P_{ij}^L(t_n) , \quad (4.15)$$

where $\Delta \epsilon_i^f$ denotes the flow strain. The incremental stress is then defined as

$$\begin{aligned} \Delta \sigma_i &= \sum_{j=1}^6 C_{ij} (\Delta \epsilon_j - \Delta \epsilon_j^f - \alpha_j \Delta \theta) \\ &= \sum_{j=1}^6 C_{ij} \Delta \epsilon_j^e . \end{aligned} \quad (4.16)$$

The incremental viscoelastic constitutive law of Equation (4.16) may be implemented in a standard displacement based finite element formulation as follows. For a given loading increment, first compute the flow strains, $\Delta\epsilon_i^f$, and the thermal strains, $\alpha_i\Delta\theta$. Using standard finite element analysis procedures, these strains generate nodal loads defined at the element level as

$$\int_V [B]^T [C] (\{\Delta\epsilon^f\} + \{\alpha\}\Delta\theta) dV \quad . \quad (4.17)$$

Additional incremental mechanical loads given by $\{\Delta F_e\}$ are added to Equation (4.17) to give an element load vector defined by

$$\{\Delta R_e\} = \int_V [B]^T [C] (\{\Delta\epsilon^f\} + \{\alpha\}\Delta\theta) dV + \{\Delta F_e\} \quad . \quad (4.18)$$

Assembly of all elements leads to a global system of equations for the incremental displacement given by

$$[K]\{\Delta u\} = \{\Delta R\} \quad . \quad (4.19)$$

Incremental strains are computed from standard strain-displacement relations given by

$$\{\Delta\epsilon\} = [B]\{\Delta u\} \quad . \quad (4.20)$$

and incremental stresses are given by Equation (4.16).

Using the finite element linear viscoelastic algorithm presented above, the hexagonally packed micromechanics model discussed in Chapter 3 was modified to implement linear viscoelasticity within the matrix. The super-elements were “deconstructed” to allow for element stress calculations at the end of each time increment as required by the

viscoelastic constitutive model. Note the matrix was assumed isotropic, as is generally the case for an undamaged neat resin polymer. Following the approach for a linear elastic analysis, composite stresses and strains were calculated using the corner node forces and displacements as detailed in Appendix C. The fiber and matrix stress/strain fields were volume averaged in order to calculate the multi-continuum constituent stress field and ensure the volume averaged results were correctly predicting the composite stress/strain field.

To test the micromechanics analysis, a combined multiaxial thermomechanical loading was applied based on a test case from Garnich and Hansen (1997). The fibers were assumed to be linear elastic and transversely isotropic with a 60% fiber volume fraction. The matrix was taken to be viscoelastic and isotropic. Table 4.1 gives the matrix and reinforcement material properties, where the x_1 direction is assumed aligned with the fibers.

Table 4.1 Viscoelastic matrix and elastic reinforcement material properties for a 60% fiber volume fraction.

Transversely Isotropic Linear Elastic Fiber Reinforcement Material Properties							
Young's Modulus	<i>GPa</i>	Poisson Ratio		Shear Modulus	<i>GPa</i>	Thermal Expansion	10^{-6} (1/°C)
E_1	220.6	ν_{12}	0.2000	G_{12}	26.00	α_1	-0.3600
E_2	13.35			G_{23}	5.516	α_2	18.00
Linear Viscoelastic Isotropic Epoxy Material Properties							
D^0 (GPa) ⁻¹	D^1 (GPa) ⁻¹	τ ¹ (Sec.)		K (GPa)	Thermal Expansion	10^{-6} (1/°C)	
0.325	-0.08300	107.0		4.309	α	40.00	

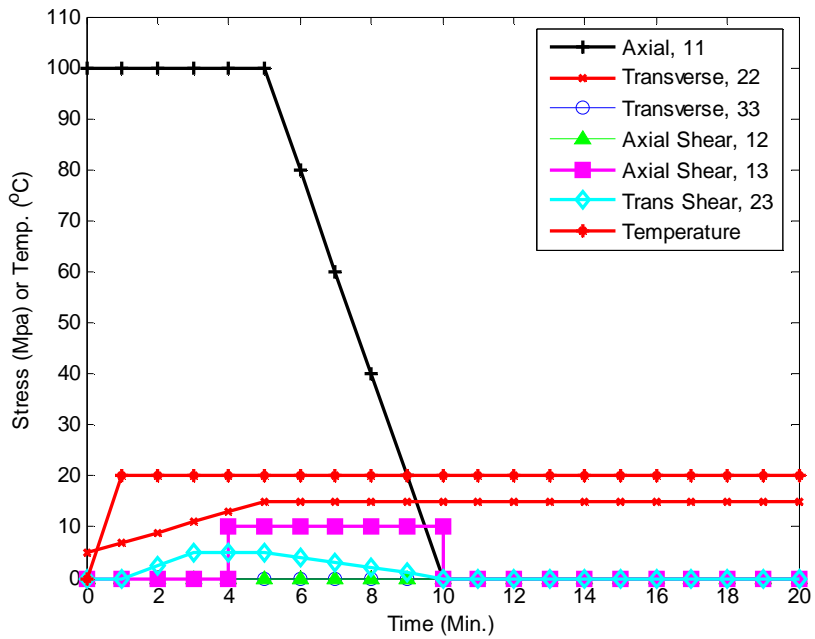


Figure 4.3 Composite stress and applied temperature history for a combined thermomechanical loading.

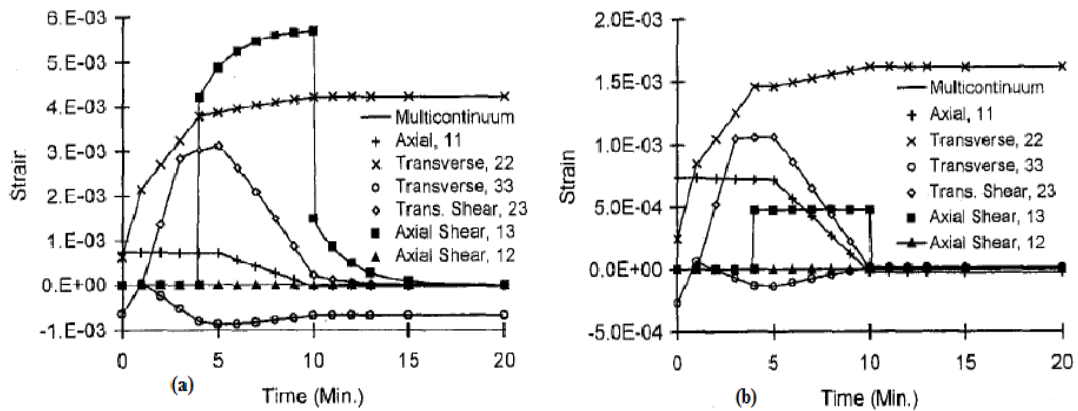


Figure 4.4 (a) Matrix strains and (b) reinforcement strains predicted by Garnich and Hansen (1997).

Figure 4.3 depicts the imposed thermomechanical loads, and Figures 4.4 and 4.5 compare the micromechanics results to those of Garnich and Hansen. The results of the current work are in agreement with the independent results of Garnich and Hansen, indicating the viscoelastic algorithm has been properly implemented.

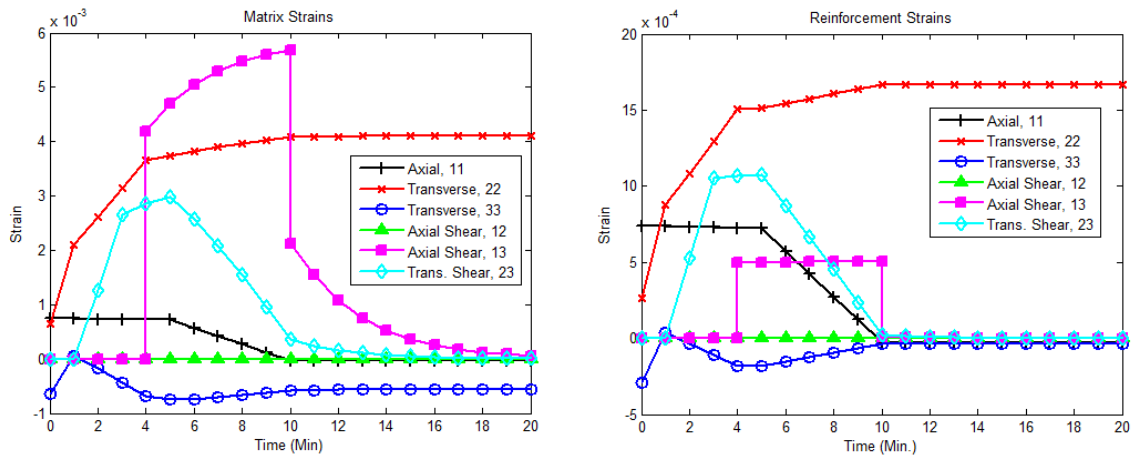


Figure 4.5 Matrix and reinforcement strains as a function of time predicted by the current micromechanics model.

4.2 Time-Temperature Superposition

The discussion of neat resin behavior thus far has been limited in scope to time-dependent behavior. However, the mechanical properties of a polymer also heavily depend on temperature. In order to capture the temperature dependence in a cure stress analysis, the viscoelastic model must be expanded such that creep behavior is modeled as a function of time and temperature.

4.2.1 Theory and Finite Element Implementation

The simplest material model for time and temperature-dependent creep behavior is to assume the material is thermorheologically simple. This assumption implies the viscoelastic response under a change in temperature is equivalent to a shift in logarithmic time. A response of this nature is said to follow time-temperature superposition (TTS). TTS is very useful in the fact that material creep compliance data taken at various

temperatures can be used to extend the model of creep behavior to a very large time scale.

Following the work of Seifert (2002), the creep compliance terms can be written as

$$D(t, T) = D(\xi, T_{ref}) \quad , \quad (4.21)$$

where T_{ref} is defined as the reference temperature and ξ is referred to as the reduced time given by

$$\xi = \frac{t}{a_T(T)} \quad . \quad (4.22)$$

In the above, $a_T(T)$ is defined as the shift factor (Lakes, 1999).

To implement TTS, a reference temperature must be chosen in which the material creep compliance is known. Then, the remaining creep compliance data must be shifted along the reduced time axis to form a master curve around the reference temperature. The data is shifted by calculating the shift factor introduced in Equation (4.22). The most common form of the shift factor, $a_T(T)$, is the Williams-Landel-Ferry (WLF) equation given by

$$\log(a_T) = \frac{-C_1(T - T_{ref})}{C_2 + T - T_{ref}} \quad , \quad (4.23)$$

where C_1 and C_2 are arbitrary real constants, and T is the temperature of the shifted data (Seifert, 2002). Note that the nature of Equation (4.23) requires at least two sets of creep compliance data other than the reference temperature data to completely define the constants C_1 and C_2 . It is desirable to incorporate a set of data with one test temperature

higher than the reference temperature and one test temperature lower than the reference temperature, but this reference temperature selection is not necessary as the constants can be determined regardless.

To develop the constitutive theory behind TTS, consider the work of Christensen (1982) in which an isotropic constitutive law for a thermorheologically simple material is introduced as

$$\epsilon_i(t) = \sum_{j=1}^6 \int_{0^-}^t \frac{d\sigma_j}{d\tau} D_{ij}(\xi - \xi') d\tau + \int_{0^-}^t \frac{d\theta}{d\tau} \alpha_i(t - \tau) d\tau \quad . \quad (4.24)$$

where

$$\xi = \int_0^t \chi(T(\eta)) d\eta \quad ,$$

and

$$\xi' = \int_0^\tau \chi(T(\eta)) d\eta \quad .$$

(4.25)

Keeping with the definition of TTS, ξ and ξ' are reduced time variables, and χ is defined as the inverse of the shift factor given as (Christensen, 1982)

$$\chi(T, t) = [a_T(T, t)]^{-1} \quad . \quad (4.26)$$

Again, the coefficients of thermal expansion are assumed to be constant with both time and temperature for the scope of this work, thereby allowing Equation (4.24) to be written as

$$\epsilon_i(t) = \sum_{j=1}^6 \int_{0^-}^t \frac{d\sigma_j}{d\tau} D_{ij}(\xi - \xi') d\tau + \alpha_i \theta(t) \quad . \quad (4.27)$$

Implementing the above constitutive relation into a finite element program is a direct extension to that of linear viscoelasticity, where the creep compliance is a function of time only. Consider an increment in time from n to $n+1$, and define $\Delta t = t_{n+1} - t_n$ and $\Delta \xi = \xi_{n+1} - \xi_n$. The incremental thermorheological viscoelastic constitutive law of Equation (4.27) then takes the form

$$\Delta \epsilon_i(t) = \sum_{j=1}^6 \left[\int_{0^-}^{t_{n+1}} \frac{d\sigma_j}{d\tau} D_{ij}(\xi_{n+1} - \xi') d\tau - \int_{0^-}^{t_n} \frac{d\sigma_j}{d\tau} D_{ij}(\xi_n - \xi') d\tau \right] + \alpha_i \Delta \theta \quad . \quad (4.28)$$

Assuming constant stress and strain over sufficiently small time steps, the integral difference pair in brackets, denoted by $\Delta I_i(t)$, above can be calculated as (Seifert, 2002)

$$\begin{aligned} \Delta I_i(t) = & \sum_{j=1}^6 \left[D_{ij}^0 \Delta \sigma_j \right. \\ & + \sum_{L=1}^N \left[P_{ij}^L(t_n) \left(\exp\left(\frac{-\Delta \xi}{\Pi_{ij}^L}\right) - 1 \right) \right. \\ & + D_{ij}^L \frac{\Delta \sigma_j \Delta t}{\Delta t} \frac{\Delta t}{6} \exp\left(\frac{-\Delta \xi - \xi_n}{\Pi_{ij}^L}\right) \left(\exp\left(\frac{\xi'_n}{\Pi_{ij}^L}\right) + 4 \exp\left(\frac{\xi'_{n+1}}{\Pi_{ij}^L}\right) \right. \\ & \left. \left. \left. + \exp\left(\frac{\xi'_{n+2}}{\Pi_{ij}^L}\right) \right) \right] \right] . \end{aligned} \quad (4.29)$$

Here ξ' is defined for half points of the defined time increment, i.e.

$$\xi'_n = \xi(t_n) \quad ,$$

$$\xi'_{n+1} = \xi(t_{n+0.5}) \quad , \quad (4.30)$$

$$\xi'_{n+2} = \xi(t_{n+1}) \quad ,$$

and P_{ij}^L is defined as

$$\begin{aligned} & P_{ij}^L(t_{n+1}) \\ &= P_{ij}^L(t_n) \exp\left(\frac{-\Delta\xi}{\prod_{ij}^L}\right) + D_{ij}^L \frac{\Delta\sigma_j \Delta t}{\Delta t} \frac{1}{6} \left(\exp\left(\frac{-\xi_{n+1} + \xi'_n}{\prod_{ij}^L}\right) \right. \\ & \left. + 4 \exp\left(\frac{-\xi_{n+1} + \xi'_{n+1}}{\prod_{ij}^L}\right) + \exp\left(\frac{-\xi_{n+1} + \xi'_{n+2}}{\prod_{ij}^L}\right) \right) . \end{aligned} \quad (4.31)$$

Seifert (2002) gives a detailed derivation of the solution of the integral difference pair given by Equation (4.30) and (4.31). The flow strain increment, defined as the strain increment in Equation (4.29) that is independent of $\Delta\sigma_j$, is given by

$$\Delta\epsilon_i^f = \sum_{j=1}^6 \sum_{L=1}^N \left(\exp\left(\frac{-\Delta\xi}{\prod_{ij}^L}\right) - 1 \right) P_{ij}^L(t_n) \quad . \quad (4.32)$$

The reduced time variables must be calculated in advance of solving the inelastic strain increment. To approximate the reduced time variables, Seifert (2002) utilizes a three point Simpson integration scheme with the WLF definition of the shift factor to arrive at

$$\xi_n \approx \sum_{k=0}^{n-1} \frac{\Delta t}{6} \left[10 \frac{C_1(T(t_k) - T_{ref})}{C_2 + T(t_k) - T_{ref}} + 4 \left(10 \frac{C_1(T(t_{k+0.5}) - T_{ref})}{C_2 + T(t_{k+0.5}) - T_{ref}} \right) + 10 \frac{C_1(T(t_{k+1}) - T_{ref})}{C_2 + T(t_{k+1}) - T_{ref}} \right] \quad (4.33)$$

$n \geq 1 \quad ,$

where $\xi_0 = 0$, and the temperatures are evaluated at half points in time. Similarly,

$$\xi'_m \approx \sum_{k=0}^{m-1} \frac{\Delta\tau}{6} \left[10^{\frac{c_1(T(\tau_k)-T_{ref})}{c_2+T(\tau_k)-T_{ref}}} + 4 \left(10^{\frac{c_1(T(\tau_{k+0.5})-T_{ref})}{c_2+T(\tau_{k+0.5})-T_{ref}}} \right) + 10^{\frac{c_1(T(\tau_{k+1})-T_{ref})}{c_2+T(\tau_{k+1})-T_{ref}}} \right] \quad (4.34)$$

$m \geq 1$,

where $\xi'_0 = 0$, $\Delta\tau = \Delta t/2$, $\tau_k = t_{0.5k}$, $\tau_{k+0.5} = t_{0.5k+0.25}$ and $\tau_{k+1} = t_{0.5k+0.5}$. It is extremely important to note that the temperatures in Equation (4.34) are evaluated at quarter points in time (Seifert, 2002). Note that if the temperature of interest is equivalent to the reference temperature, the terms within the summation of Equations (4.33) and (4.34) simply evaluate to t and τ , respectively. Thus, an increment in reduced time collapses to that of a real time as $\Delta\xi = \Delta t$.

Given the flow strain of Equation (4.32), the element flow strain load vector can be formulated for any time and temperature and assembled into the global system of equations.

Finally, note that the creep compliance of Equation (4.21) implies the elastic response of the neat resin is a function of temperature. The temperature dependence of elastic constants has serious adverse effects on numerical efficiency as the stiffness matrix must be formulated at every increment. Hence, incremental solutions require factorization of the global stiffness matrix at every time step. Therefore, from a numerical viewpoint, TTS represents an enormous jump in computational effort.

4.2.2 Derakane 510 Master Curve

The material chosen to model the resin during a curing cycle of a typical composite material was Derakane 510, a vinylester polymeric resin supplied by the Naval Surface Warfare Center and manufactured by Dow®. This specific resin was chosen because of the known material properties at elevated temperatures, as tested by the University of Wyoming (Seifert, 2002). Table 4.2 gives the neat resin elastic data for a wide range of temperatures, and Table 4.3 gives the neat resin viscoelastic curve fit data for three elevated temperatures based on a creep compliance of the form

$$D(t) = D^0 + \sum_{L=1}^N D^L \exp\left(\frac{-t}{\Pi^L}\right) . \quad (4.35)$$

Table 4.2 Average isotropic material properties of Derakane 510 for various temperatures.

Temperature (°C)	Young's Modulus (GPa)	Poisson's Ratio	Shear Modulus (GPa)
24	3.300	0.3200	1.250
66	2.500	0.3300	0.9400
93	1.500	0.3700	0.5470
121	0.01400	0.4800	0.004730
149	0.008000	0.3300	0.003010

Table 4.3 Derakane 510 neat resin viscoelastic data for various temperatures.

Temperature (°C)	D^0 (GPa) ⁻¹	D^1 (GPa) ⁻¹	D^2 (GPa) ⁻¹	Π^1 (Sec.)	Π^2 (Sec.)	K (GPa)
24	0.327	-0.03000	-0.01100	16040	1623	3.241
66	1.053	-0.2380	-0.4140	873.0	22840	2.451
93	2.774	-1.108	-0.9990	339.0	4686	1.923

The viscoelastic data given in Table 4.3 was utilized to develop a master curve in accordance with TTS. After trial and error modeling of the master curve, the reference temperature was chosen to be 66°C. The shift factors were chosen based upon a “best

eye fit” approach and the two unknown constants were calculated utilizing the WLF equation (Equation (4.23)). To give the reader an intuitive grasp for TTS, an example of shifting experimental data in time is shown in Figure 4.6. Table 4.4 gives the constants C_1 and C_2 calculated for Derakane 510 along with the corresponding shift factors.

Table 4.4 Master curve coefficients for Derakane 510.

Shift Factors	
Temperature ($^{\circ}C$)	a_T
24	3.000×10^4
66	1.400×10^{-2}
Williams-Landel-Ferry Equation Constants	
C_1	C_2 ($^{\circ}C$)
-13.31	166.89

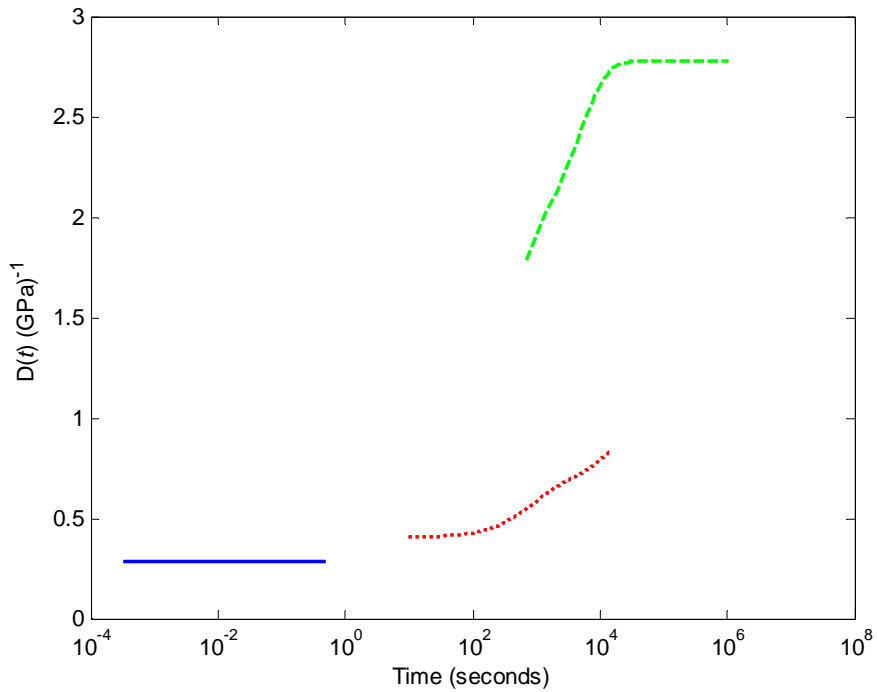


Figure 4.6 Master curve for Derakane 510.

4.3 Micromechanics Cool-Down Study

When a unidirectional composite material is exposed to a temperature change, constituent level residual stresses will develop from a stress-free state as a direct result of mismatched constituent thermomechanical properties. The stress-free state for a cure cycle is the elevated temperature from which cool-down initiates. The cure cycle chosen for this study was a linear temperature profile in time from an elevated temperature to room temperature for one hour at atmospheric pressure. The one-hour time duration is typical of many composites with a vinylester matrix. Because the neat resin elastic data was only known up to 150°C, the elevated temperature was chosen to be this temperature. A plot of the creep compliance indicates that, at this temperature, the matrix behaves as nearly liquid in that the stiffness is virtually nonexistent. Thus, the rationale for choosing the elevated temperature at 150°C is supported in that higher temperatures will produce negligible thermal stresses in cooling to 150°C.

To generalize cool-down results for a range of composite materials, an isotropic glass fiber and a transversely isotropic carbon fiber were employed with the thermoviscoelastic micromechanics model outlined above. Table 4.5 gives the elastic properties for the glass and carbon fibers, and Table 4.6 gives the coefficients of thermal expansion for the neat resin and both fibers.

Table 4.5 Fiber material properties for micromechanics cool-down study.

AS4 Carbon Fiber					
Young's Modulus	<i>GPa</i>	Poisson Ratio	Shear Modulus	<i>GPa</i>	
E_1	227.	ν_{12}	0.245	G_{12}	28.0
E_2	25.0			G_{23}	9.50
EGlass Fiber					
Young's Modulus	<i>GPa</i>	Poisson Ratio	Shear Modulus	<i>GPa</i>	
E	71.0	0.260	G	28.3	

Table 4.6 Coefficients of thermal expansion for micromechanics cool-down study.

Constituent	Longitudinal α_1 $10^{-6} (1/^\circ\text{C})$	Transverse α_2 $10^{-6} (1/^\circ\text{C})$	Transverse α_3 $10^{-6} (1/^\circ\text{C})$
Derakane 510	60.0	60.0	60.0
AS4 Carbon Fiber	-0.70	5.00	5.00
EGlass Fiber	5.04	5.04	5.04

A time sensitivity study was also conducted to ensure that the calculated stresses did not heavily depend on the rate of cooling. The times chosen for the analysis were 10 minutes, 1 hour, and 5 hours. Table 4.7 details the time sensitivity results for a glass/vinylester with a 60% fiber volume fraction, and Table 4.8 details the results for the carbon/vinylester composite with a 60% fiber volume fraction. Note shear stresses are absent as changes in temperature only impact normal stresses. As expected, the stress magnitudes decrease with increasing time but not enough to warrant further investigation or discussion.

Table 4.7 Glass/vinylester composite viscoelastic cool-down constituent stresses (*MPa*) for a fiber volume fraction of 60%. Superscripts represent the constituent.

Time	σ_{11}^m	σ_{22}^m	σ_{33}^m	σ_{11}^f	σ_{22}^f	σ_{33}^f
10 minutes	16.2	6.29	6.29	-10.9	-4.24	-4.24
1 hour	15.7	6.09	6.09	-10.6	-4.11	-4.11
5 hours	15.1	5.88	5.88	-10.2	-3.97	-3.97

Table 4.8 Carbon/vinylester composite viscoelastic cool-down constituent stresses (*MPa*) for a fiber volume fraction of 60%. Superscripts represent the constituent.

Time	σ_{11}^m	σ_{22}^m	σ_{33}^m	σ_{11}^f	σ_{22}^f	σ_{33}^f
10 minutes	17.7	6.37	6.37	-12.0	-4.30	-4.30
1 hour	17.2	6.17	6.17	-11.6	-4.16	-4.16
5 hours	16.6	5.96	5.96	-11.2	-4.02	-4.02

A cool-down was also conducted for a single time step assuming constant elastic material properties at room temperature for both the fiber and matrix. Table 4.9 details the stresses predicted for an elastic increment for the glass/vinylester and carbon/vinylester composites with 60% fiber volume fraction.

Table 4.9 Glass/vinylester and carbon/vinylester composite elastic cool-down constituent stresses (*MPa*) for a fiber volume fraction of 60%. Superscripts represent the constituent.

Material	σ_{11}^m	σ_{22}^m	σ_{33}^m	σ_{11}^f	σ_{22}^f	σ_{33}^f
Glass Vinylester	35.1	13.7	13.7	-23.7	-9.22	-9.22
Carbon Vinylester	38.6	13.8	13.8	-26.0	-9.30	-9.30

Note the elastic stresses are almost two times those predicted by the TTS viscoelastic analysis. This difference is due to the fact that the matrix flows at elevated temperatures, thus relieving the stresses residing in both the fiber and matrix. For an elastic time step the matrix cannot flow, and thus the change in temperature causes larger residual stresses. Therefore, modeling a cool-down elastically does not properly capture the residual stresses produced by a cure cycle.

5. THE IMPACT OF THERMAL LOADS ON FAILURE PREDICTIONS

The current approach to determining constituent-based failure in an MCT analysis relies on the assumption that both the fiber and matrix are at a stress-free state before loading. This assumption is based on the premise that any residual cure stresses residing in the constituents before a strength test are accounted for during the strength test, and the resulting strength parameters intrinsically account for the cure stresses. In other words, if a tested failure strength of a composite at ambient temperature was decomposed to the fiber and matrix, the constituent failure strengths would include the effects of the cure cycle. While this argument is both elegant and desirable from an implementation perspective, the question of thermal cure stresses affecting failure of composite materials presents itself as a viable, and somewhat problematic, possibility.

Thermal loads in a composite structure induce several complexities that are not seen in a purely mechanical problem. For instance, consider free thermal expansion/contraction of a multidirectional composite laminate. Because each individual lamina has its own thermal expansion properties, thermal stresses are introduced at the ply level that are, in total, in equilibrium for the overall laminate. In addition to the various ply-level stresses, self-equilibrating internal stresses at the constituent level arise due to mismatched thermal expansion properties between the fiber and matrix constituents. Hence, even the simplest case of uniform thermal loads produces extremely complex stress states. The problem of analyzing such stress states is compounded by the need to transcend multiple geometric scales.

A key advantage to MCT over conventional composite failure analyses is the ability to compute induced constituent thermal strains and corresponding constituent stress fields in the course of a structural (laminate) level analysis. Because of this capability, a natural and worthy exercise is to investigate the effects of temperature changes on failure predictions.

5.1 Failure Coefficient Modifications for Thermal Cure Stresses

Consider the constituent failure equations given in Chapter 2 as

$$\pm A_1^f (I_1^f)^2 + A_4^f I_4^f = 1 \quad , \quad (5.1)$$

and

$$\pm A_1^m (I_1^m)^2 - \pm A_2^m (I_2^m)^2 + A_3^m I_3^m + A_4^m I_4^m - \pm A_5^m I_1^m I_2^m = 1 \quad , \quad (5.2)$$

where the superscripts m and f represent the fiber and matrix constituents, respectively.

The A_i^β ($\beta = f, m$) terms are failure coefficients determined from composite strength data and the MCT decomposition. Finally, the I_i^β terms are the transversely isotropic stress invariants given by Equation (2.17), where the longitudinal axis of symmetry is assumed aligned with the x_1 axis.

5.1.1 Purely Mechanical Approach

Consider the fiber failure criterion given by Equation (5.1). Three coefficients, given by

$^+A_1^f$, $^-A_1^f$, and A_4^f , are required to completely characterize fiber failure.

To determine ${}^+A_1^f$, a longitudinal tension test for a composite is assumed to result in fiber failure. Thus, the longitudinal composite tensile strength can be decomposed to that of the fiber, and Equation (5.1) can be solved as

$${}^+A_1^f = \frac{1}{({}^+S_{11}^f)^2} \quad , \quad (5.3)$$

where ${}^+S_{11}^f$ represents the longitudinal stress in the fiber at composite longitudinal tensile failure. The procedure outlined above can also be completed for longitudinal compression, as this failure state is assumed to be governed by fiber kinking (buckling). Therefore, one can write

$${}^-A_1^f = \frac{1}{({}^-S_{11}^f)^2} \quad . \quad (5.4)$$

The remaining term, A_4^f , is calculated from composite longitudinal shear data. In particular, given a longitudinal composite shear stress of σ_{12} , Equation (5.1) reduces to

$$A_4^f = \frac{1}{(S_{12}^f)^2} \quad , \quad (5.5)$$

where S_{12}^f represents the longitudinal fiber shear stress at failure. While this approach appears straightforward, the actual value computed in Equation (5.5) is problematic as the type of test used to determine the composite longitudinal shear strength can significantly alter the results. For example, if the test utilizes wound cylinders consisting of a $\pm 45^\circ$

laminate to generate the data, failure is assumed to be fiber dominated due to the inherent continuous fiber fabrication of the cylinder. In contrast, if the test utilizes a unidirectional laminate, such as in an Iosipescu shear test, the failure is assumed to be matrix dominated. Excessive deflections are typically observed in Iosipescu shear tests indicating large matrix strains are occurring. For a shear test governed by matrix failure, fiber failure due to longitudinal shear must be estimated. Based on data from the WWFE, fiber failure for a *matrix failure dominated* longitudinal shear test is modeled as

$$A_4^f = \frac{1}{\left((1.25)S_{12}^f\right)^2} , \quad (5.6)$$

where S_{12}^f is the fiber stress at composite longitudinal shear failure. The fiber shear strength at composite shear failure is scaled by a factor of 1.25 to enforce fiber failure at a larger composite stress state than that of matrix longitudinal shear failure.

The failure coefficients for the matrix failure criterion of Equation (5.2) are much more difficult to determine, as there are multiple interacting terms making it difficult to isolate individual coefficients. To begin, consider the matrix stress state under composite longitudinal tensile failure. As discussed previously, this failure is assumed to be fiber dominated. Moreover, matrix failure is assumed to occur at stresses greater than those at composite longitudinal failure. Next note that under composite longitudinal tension or compression $\sigma_{11}^m \gg \sigma_{22}^m = \sigma_{33}^m$. Thus, the transverse stresses in the matrix at longitudinal failure are disregarded, and the matrix stress state is assumed to be one-dimensional leading to the isolation of $\pm A_1^m$ in the matrix failure criterion. Because the precise value

of matrix strength is unknown in longitudinal tension and compression, the failure coefficients ${}^{\pm}A_1^m$ are expressed as

$${}^+A_1^m = \frac{\lambda}{({}^+S_{11}^m)^2} \quad , \quad (5.7)$$

and

$${}^-A_1^m = \frac{\kappa}{({}^-S_{11}^m)^2} \quad , \quad (5.8)$$

where ${}^{\pm}S_{11}^m$ is the matrix stress at composite failure in uniaxial tension and compression, respectively. The coefficients λ and κ are arbitrary scaling factors that are adjusted to provide a best fit of biaxial composite data (σ_{11} - σ_{22}). In the absence of biaxial data, data from the WWFE suggests good values for λ and κ are 0.8.

The coefficient A_4^m is determined from an Iosipescu shear test of a unidirectional composite as

$$A_4^m = \frac{1}{(S_{12}^m)^2} \quad , \quad (5.9)$$

where S_{12}^m is the matrix stress at composite longitudinal shear failure. Failure in transverse shear is also assumed to be matrix dominated and hence the coefficient A_3^m can be calculated from a transverse shear test to failure as

$$A_3^m = \frac{1}{(S_{23}^m)^2} \quad , \quad (5.10)$$

where S_{23}^m is the matrix stress at composite transverse shear failure.

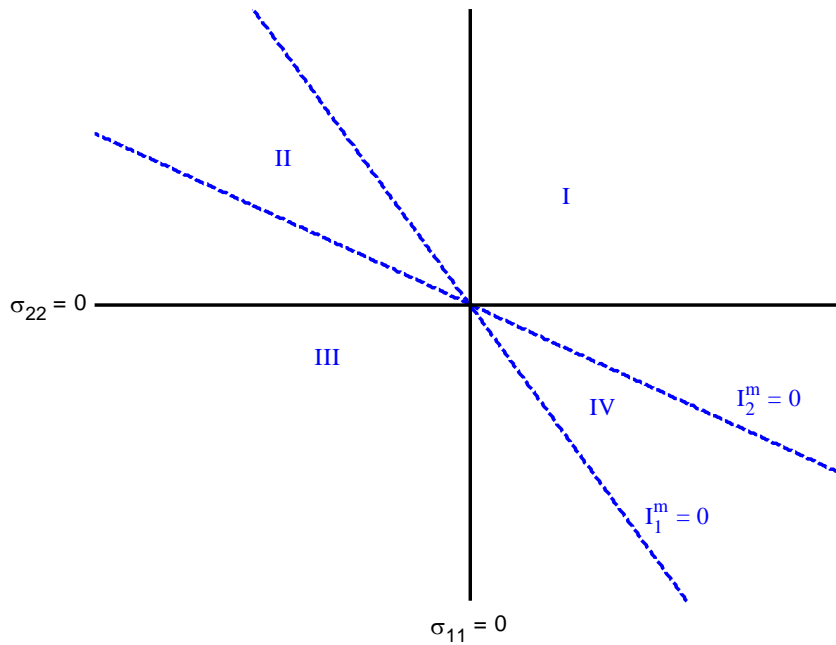


Figure 5.1 Matrix invariant axes plotted against composite biaxial stress space.

The remaining coefficients, $^+A_2^m$, $^-A_2^m$, $^+A_5^m$, $^\pm A_5^m$, $^-A_5^m$, and $^\mp A_5^m$, are more difficult to determine as they cannot be isolated with a standard test. An additional complicating factor is that “quadrants” of matrix stress space, defined by $I_1^m = 0$ and $I_2^m = 0$, are not comparable to the biaxial quadrants defined by composite stress space. Figure 5.1 shows typical quadrants of matrix stress-space plotted in the context of the quadrants of a composite loaded biaxially ($\sigma_{11} - \sigma_{22}$).

Matrix stress space is defined in terms of stress invariants as opposed to stress components because any biaxial lamina stress state usually results in a three-dimensional state of stress within the constituents. Defining the matrix quadrants in terms of the invariants allows one to view these stresses in a two-dimensional form, and this definition will provide the basis of the discussion for the remainder of the coefficients.

Referring to Figure 5.1, determination of $^{-}A_2^m$ is achieved by loading the composite biaxially such that $I_1^m = 0$ and $I_2^m < 0$. Along this load path, the matrix failure criterion collapses to

$$-^{-}A_2^m(I_2^m)^2 + A_3^m I_3^m = 1 \quad . \quad (5.11)$$

Thus, knowing the term A_3^m from Equation (5.10), parameter $^{-}A_2^m$ can be calculated easily provided biaxial composite data is available in quadrant IV of composite stress space. If no biaxial data is available along the load path $I_1^m = 0$, there exists two ways of determining parameter $^{-}A_2^m$ depending on the type of reinforcement used in the composite. If the composite utilizes a glass fiber reinforcement, the failure criteria of Hill (1950) for anisotropic materials is employed, as experimental data indicates that composite failure is reasonably represented by this criterion. In contrast, if the reinforcement is a carbon fiber, experimental data shows that a max-transverse stress criterion should be employed. The difference between glass/epoxy and carbon/epoxy behavior may be explained by the longitudinal modulus of the fibers. Specifically, the longitudinal carbon modulus is approximately three times that of glass. As a result, axial *matrix* stress in carbon/epoxy composites does not have the opportunity to build to sufficient values to impact failure under biaxial loading.

Parameter $^{+}A_2^m$ is calculated in a similar manner to that of $^{-}A_2^m$ in that the composite is loaded biaxially such that $I_1^m = 0$ and $I_2^m > 0$. However, a max-stress criterion is employed for both glass/epoxy and carbon/epoxy unidirectional lamina as tensile failure is generally governed by a max stress phenomenon.

Now that parameters ${}^+A_2^m$ and ${}^-A_2^m$ are known, the remaining parameters ${}^+A_5^m$, ${}^\pm A_5^m$, ${}^-A_5^m$, and ${}^\mp A_5^m$ can be determined. Specifically, parameter ${}^\pm A_5^m$ is calculated by following any biaxial load path in quadrant IV of matrix stress space. In the absence of biaxial data, the anisotropic yield criterion of Hill is again employed for a glass/epoxy unidirectional composite, and a max transverse stress criterion is again employed for carbon/epoxy unidirectional laminates.

${}^+A_5^m$ is determined from loading the composite in transverse tension, as matrix stresses from transverse tension reside in quadrant I of matrix stress space. ${}^-A_5^m$ is calculated in a similar manner by loading the composite in transverse compression. Lastly, ${}^\mp A_5^m$ is calculated by enforcing a max transverse stress criterion for an arbitrary load path in quadrant II of matrix stress space.

5.1.2 Cure Stress Approach

The discussion presented in Section 5.1.1 assumes both the fiber and matrix are at a stress-free state when determining failure coefficients. When investigating the effects of cure stresses on failure predictions of unidirectional composites, the coefficients of the failure criteria in Equations (5.1) and (5.2) must be determined differently than the process followed in Section 5.1.1.

To introduce cure stress effects into a failure analysis, one must first determine the values of the cure stresses at ambient (reference) temperatures. Computing precise values of

cure stresses for all possible materials studied here-in is unreasonable due to the onerous material characterization required. However, one can rely on the cure stress analysis presented in Chapter 4 as a means of providing reasonable values of cure stresses for glass/epoxy and carbon/epoxy unidirectional composites. In particular, the cure stresses for a one hour linear cool-down given in Tables 4.7 and 4.8 are considered to represent the constituent stresses for a typical curing cycle. These cure stresses are utilized within this chapter to analyze the effects of cure stresses on failure predictions.

Now consider the fiber failure criterion of Equation (5.1). The process described in Section 5.1.1 for computing ${}^+A_1^f$ and ${}^-A_1^f$ does not change as transverse stresses are not included in the fiber failure criterion. However, the longitudinal stresses found in Tables 4.7 and 4.8 for a cure cycle must be added to the stresses from the MCT decomposition at failure. Thus, the coefficients ${}^+A_1^f$ and ${}^-A_1^f$ are represented as

$${}^+A_1^f = \frac{1}{\left({}^+S_{11}^f + \sigma_{11}^{f(cure)} \right)^2} , \quad (5.12)$$

and

$${}^-A_1^f = \frac{1}{\left(-S_{11}^f + \sigma_{11}^{f(cure)} \right)^2} . \quad (5.13)$$

Here, ${}^+S_{11}^f$ and ${}^-S_{11}^f$ are the fiber stresses at composite longitudinal tension and compression failure, respectively, and $\sigma_{11}^{f(cure)}$ is the longitudinal stress in the fiber resulting from the cure cycle.

Following Section 5.1.1, coefficient A_4^f is calculated based on longitudinal shear failure data. However, because cure stresses have been introduced, the fiber stress tensor is inherently three-dimensional, even in a simple longitudinal shear loading. Thus, the fiber failure criterion becomes

$$-A_1^f (I_1^f)^2 + A_4^f I_4^f = 1 \quad , \quad (5.14)$$

where $-A_1^f$ has been calculated previously, I_1^f contains the longitudinal stress in the fiber from the curing cycle as

$$I_1^f = \sigma_{11}^{f(cure)} \quad , \quad (5.15)$$

and I_4^f contains the fiber shear stress from the composite failure in longitudinal shear as

$$I_4^f = S_{12}^f \quad . \quad (5.16)$$

Noting the above, parameter A_4^f is solved for as

$$A_4^f = \frac{1 - -A_1^f (I_1^f)^2}{I_4^f} \quad . \quad (5.17)$$

Note that the composite longitudinal shear stress at failure may be scaled to capture the type of test used to determine the longitudinal shear strength.

Determination of $+A_1^m$ and $-A_1^m$ follows the same process as Section 5.1.1, but the matrix stresses from the cure cycle must again be added to the stresses at failure. Again note the stresses residing in the matrix for a typical curing cycle are shown in Tables 4.7 and 4.8. The longitudinal cure stress exceeds the transverse cure stresses by approximately a factor of three, thereby preserving the assumption presented in Section

5.1.1 that $\sigma_{11}^m \gg \sigma_{22}^m = \sigma_{33}^m$ for the matrix stresses at composite longitudinal failure.

Thus, ${}^+A_1^m$ and ${}^-A_1^m$ are represented as

$${}^+A_1^m = \frac{\lambda}{\left({}^+S_{11}^m + \sigma_{11}^{m(cure)}\right)^2} , \quad (5.18)$$

and

$${}^-A_1^m = \frac{\kappa}{\left({}^-S_{11}^m + \sigma_{11}^{m(cure)}\right)^2} , \quad (5.19)$$

respectively. Here ${}^+S_{11}^m$ and ${}^-S_{11}^m$ represent the matrix stresses at composite tension and compression failure, respectively, and $\sigma_{11}^{m(cure)}$ represents the residual stress in the matrix from the cure cycle. Also, λ and κ represent the same scaling coefficients identified and discussed in the purely mechanical derivation presented in Section 5.1.1.

The shear coefficient A_3^m is calculated similarly to the purely mechanical analysis by considering a transverse shear loading. However, following the discussion for fiber failure in longitudinal shear, incorporating thermal cure stresses results in a three-dimensional matrix stress state, and the matrix failure criterion becomes

$${}^+A_1^m(I_1^m)^2 - {}^+A_2^m(I_2^m)^2 + A_3^m I_3^m - {}^+A_5^m I_1^m I_2^m = 1 , \quad (5.20)$$

where I_1^m , I_2^m , and I_3^m are given by

$$I_1^m = \sigma_{11}^{m(cure)} , \quad (5.21)$$

$$I_2^m = \sigma_{22}^{m(cure)} + \sigma_{33}^{m(cure)} ,$$

and

$$I_3^m = \left(\sigma_{22}^{m(cure)}\right)^2 + \left(\sigma_{33}^{m(cure)}\right)^2 + 2(S_{23}^m)^2 \quad .$$

Note the only known failure coefficient in Equation (5.20) is ${}^+A_1^m$, and thus no other terms can be solved for explicitly.

Next consider a composite loaded in longitudinal shear to failure. For this loading, the matrix failure criterion collapses to

$${}^+A_1^m(I_1^m)^2 - {}^+A_2^m(I_2^m)^2 + A_3^m I_3^m + A_4^m I_4^m - {}^+A_5^m I_1^m I_2^m = 1 \quad , \quad (5.22)$$

where

$$I_1^m = \sigma_{11}^{m(cure)} \quad ,$$

$$I_2^m = \sigma_{22}^{m(cure)} + \sigma_{33}^{m(cure)} \quad ,$$

$$I_3^m = \left(\sigma_{22}^{m(cure)}\right)^2 + \left(\sigma_{33}^{m(cure)}\right)^2 \quad , \quad (5.23)$$

and

$$I_4^m = (S_{12}^m)^2 \quad .$$

To obtain closure for determining the remaining coefficients, ${}^+A_2^m$, ${}^-A_2^m$, ${}^+A_5^m$, ${}^\pm A_5^m$, ${}^-A_5^m$, and ${}^\mp A_5^m$, the procedure outlined in Section 5.1.1 is closely followed. However, the matrix stress space delineated by the bisecting axes $I_1^m = 0$ and $I_2^m = 0$ must shift, as

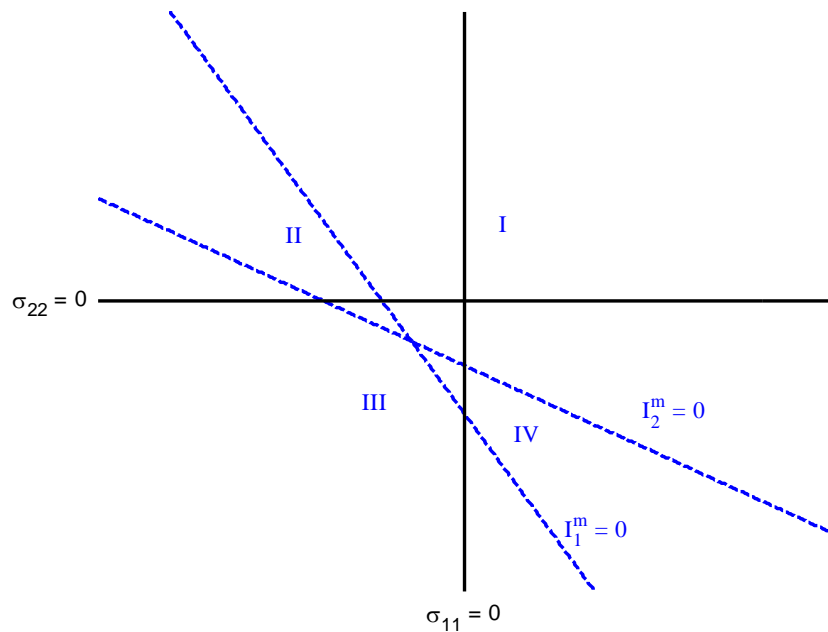


Figure 5.2 Matrix invariant axes incorporating matrix cure stresses plotted against biaxial composite stress space.

a zero composite stress results in nonzero matrix stresses. Figure 5.2 depicts the matrix stress space plotted against composite biaxial stress space with residual stresses included.

Coefficient $^{-}A_2^m$ is utilized by loading the composite biaxially such that $I_1^m = 0$ and $I_2^m < 0$. As discussed in Section 5.1.1, two different failure criteria, depending on the type of reinforcement, are employed when biaxial data along this load path is absent. In particular, a max-stress criterion is enforced for a carbon/epoxy lamina, and Hill's (1950) anisotropic yield criterion is employed for a glass/epoxy lamina. Similarly, $^{+}A_2^m$ is used by enforcing a max-stress criterion along the load path $I_1^m = 0$ and $I_2^m > 0$.

An equation involving the matrix failure coefficient $\pm A_5^m$ is formulated by following a load path in quadrant IV of matrix stress space to failure. Again, in the absence of biaxial data, the anisotropic yield criterion of Hill is employed for glass/epoxy unidirectional laminae, and a max transverse stress criterion is employed for carbon/epoxy unidirectional laminae. An equation for $\mp A_5^m$ is formed by following an arbitrary load path in quadrant II of matrix stress space, and enforcing a max-transverse stress criterion. Lastly, equations involving matrix failure coefficients $+A_5^m$ and $-A_5^m$ are formed by considering the transverse strengths of the composite in tension and compression, respectively. Note that when decomposing the composite stress field to the matrix for the failure coefficients $\pm A_5^m$, $\mp A_5^m$, $+A_5^m$, and $-A_5^m$, the thermal residual stresses from cure must be added to the decomposed stresses to gain an accurate description of the stresses residing in the matrix.

In summary, determining the matrix failure coefficients with residual stresses from a thermal cure cycle generates eight failure coefficients that cannot be solved for directly due to coupling of the equations, namely $A_3^m, A_4^m, +A_2^m, -A_2^m, \pm A_5^m, \mp A_5^m, +A_5^m$, and $-A_5^m$. However, it is a simple manner to solve the system of eight equations and eight unknowns for the linear system by employing matrix algebra solution techniques.

5.2 Unidirectional Lamina Room Temperature Failure Predictions

The failure coefficients outlined in Section 5.1 were computed for a carbon/epoxy and two glass/epoxy unidirectional composites with 60% fiber volume fractions. Table 5.1 provides the fiber, matrix, and composite material properties for an EGlass/LY556

transversely isotropic composite, Table 5.2 gives properties for a Silenka/MY750 glass/epoxy transversely isotropic composite, and Table 5.3 gives properties for a T300/BSL914C carbon/epoxy transversely isotropic composite. All material data is explained in detail in Hinton *et. al.* (2004). However, it should be noted that the constituent material properties were modified to give the same set of composite material stiffness properties provided by Hinton *et. al.* while also being consistent with the micromechanics model. Finally, note that for transverse isotropy with symmetry about the x_1 axis: $E_2 = E_3$, $\nu_{12} = \nu_{13}$, $G_{12} = G_{13}$, and $\alpha_2 = \alpha_3$. Moreover, the transverse shear modulus may be written as

$$G_{23} = \frac{E_2}{2(1 + \nu_{23})} \quad (5.24)$$

Table 5.1 Fiber, matrix, and composite transversely isotropic material properties for EGlass/LY556.

EGlass/LY556 Transversely Isotropic Composite Material Properties with 60% Fiber Volume Fraction						
E_1 (GPa)	E_2 (GPa)	ν_{12}	ν_{23}	G_{12} (GPa)	$\alpha_1 10^{-6}$ (1/°C)	$\alpha_2 10^{-6}$ (1/°C)
53.5	17.7	0.278	0.400	5.83	8.60	26.4

EGlass/LY556 Transversely Isotropic Composite Strengths with 60% Fiber Volume Fraction					
S_{11}^+ (GPa)	S_{11}^- (MPa)	S_{22}^+ (MPa)	S_{22}^- (MPa)	S_{12} (MPa)	S_{23} (MPa)
1.14	-570.	35.0	-113.	72.0	50.0

EGlass Isotropic Glass Fiber						
E_1 (GPa)	E_2 (GPa)	ν_{12}	ν_{23}	G_{12} (GPa)	$\alpha_1 10^{-6}$ (1/°C)	$\alpha_2 10^{-6}$ (1/°C)
80.0	80.0	0.200	0.200	33.3	4.90	4.90

LY556 Isotropic Matrix						
E_1 (GPa)	E_2 (GPa)	ν_{12}	ν_{23}	G_{12} (GPa)	$\alpha_1 10^{-6}$ (1/°C)	$\alpha_2 10^{-6}$ (1/°C)
3.35	3.35	0.350	0.350	1.24	58.0	58.0

Table 5.2 Fiber, matrix, and composite transversely isotropic material properties for Silenka/MY750.

Silenka/MY750 Transversely Isotropic Composite Material Properties with 60% Fiber Volume Fraction						
E_1 (GPa)	E_2 (GPa)	ν_{12}	ν_{23}	G_{12} (GPa)	$\alpha_1 10^{-6}$ (1/°C)	$\alpha_2 10^{-6}$ (1/°C)
45.6	16.2	0.278	0.400	5.83	8.60	26.4
Silenka/MY750 Transversely Isotropic Composite Strengths with 60% Fiber Volume Fraction						
S_{11}^+ (GPa)	S_{11}^- (MPa)	S_{22}^+ (MPa)	S_{22}^- (MPa)	S_{12} (MPa)	S_{23} (MPa)	
1.28	-800.	40.0	-145.	73.0	50.0	
Silenka Isotropic Glass Fiber						
E_1 (GPa)	E_2 (GPa)	ν_{12}	ν_{23}	G_{12} (GPa)	$\alpha_1 10^{-6}$ (1/°C)	$\alpha_2 10^{-6}$ (1/°C)
73.0	73.0	0.200	0.200	30.8	4.10	4.10
MY750 Isotropic Matrix						
E_1 (GPa)	E_2 (GPa)	ν_{12}	ν_{23}	G_{12} (GPa)	$\alpha_1 10^{-6}$ (1/°C)	$\alpha_2 10^{-6}$ (1/°C)
3.35	3.35	0.350	0.350	1.24	58.0	58.0

Table 5.3 Fiber, matrix, and composite transversely isotropic material properties for T300/BSL914C.

T300/BSL914C Transversely Isotropic Composite Material Properties with 60% Fiber Volume Fraction						
E_1 (GPa)	E_2 (GPa)	ν_{12}	ν_{23}	G_{12} (GPa)	$\alpha_1 10^{-6}$ (1/°C)	$\alpha_2 10^{-6}$ (1/°C)
138.	11.00	0.280	0.400	5.50	-1.00	26.0
T300/BSL914C Transversely Isotropic Composite Strengths with 60% Fiber Volume Fraction						
S_{11}^+ (GPa)	S_{11}^- (MPa)	S_{22}^+ (MPa)	S_{22}^- (MPa)	S_{12} (MPa)	S_{23} (MPa)	
1.500	-900.	27.0	-200.	80.0	74.3	
T300 Transversely Isotropic Carbon Fiber						
E_1 (GPa)	E_2 (GPa)	ν_{12}	ν_{23}	G_{12} (GPa)	$\alpha_1 10^{-6}$ (1/°C)	$\alpha_2 10^{-6}$ (1/°C)
230.	15.0	0.200	0.0710	15.0	-0.700	12.0
BSL914C Isotropic Matrix						
E_1 (GPa)	E_2 (GPa)	ν_{12}	ν_{23}	G_{12} (GPa)	$\alpha_1 10^{-6}$ (1/°C)	$\alpha_2 10^{-6}$ (1/°C)
4.00	4.00	0.350	0.350	1.48	55.0	55.0

In the WWFE, the first three failure envelope predictions requested by the organizers were for unidirectional laminates (Hinton *et. al.*, 2004). In particular, Case 1 was for an EGlass/LY556 unidirectional lamina loaded under longitudinal shear and transverse tension/compression. Using this case as a benchmark, failure envelopes were generated with and without residual stresses to determine the effects of cure stresses on failure

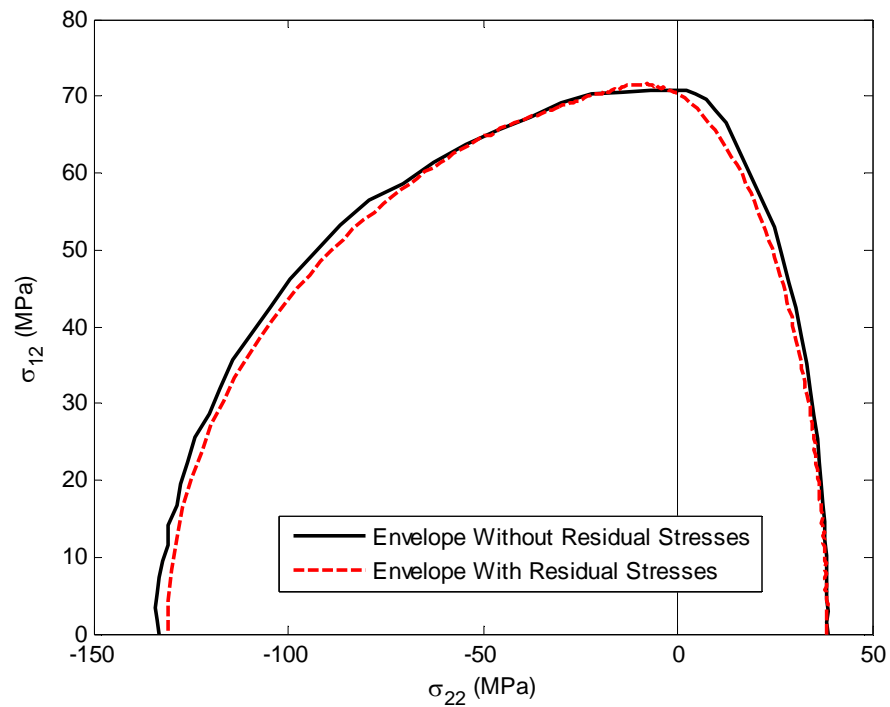


Figure 5.3 Room temperature failure envelope comparison for an EGlass/LY556 glass/epoxy unidirectional lamina.

predictions. Figure 5.3 depicts the failure envelope comparison. The two failure envelopes are, for practical purposes, identical, thereby indicating that cure stresses are intrinsically accounted for by the failure data generated at ambient temperature. It should be noted that Mayes and Hansen (2004) argued for this position in their original submission of the WWFE.

Figure 5.4 compares failure predictions for combined longitudinal shear and longitudinal tension/compression of a T300/BSL914C carbon/epoxy unidirectional lamina with and without residual cure stresses. Again, any difference in the two envelopes is negligible.

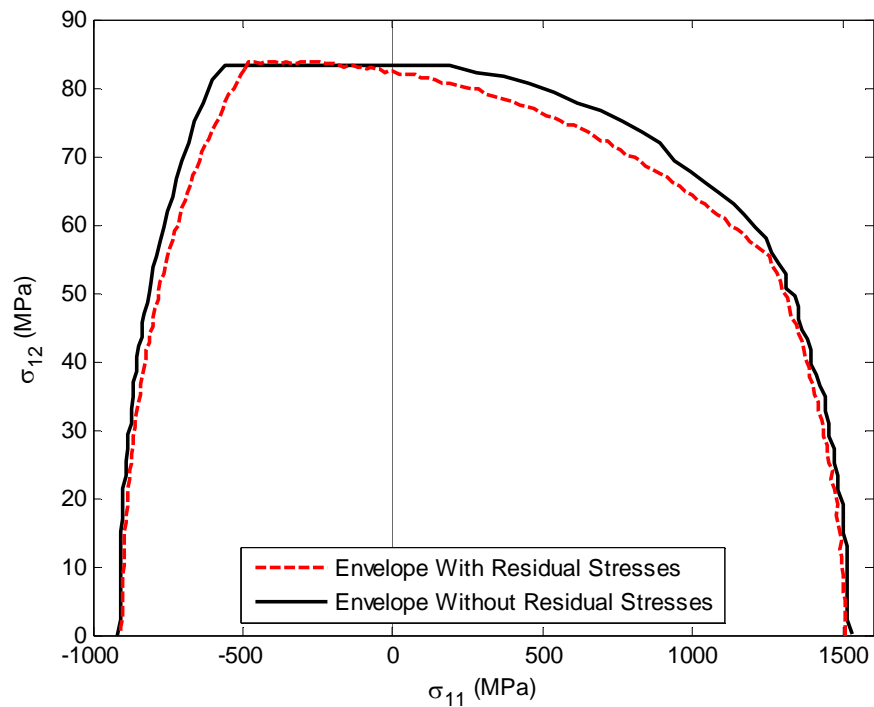


Figure 5.4 Room temperature failure envelope comparison for a T300/BSL914C carbon/epoxy unidirectional lamina.

The last room temperature failure envelope studied was biaxial loading of a Silenka/MY750 glass/epoxy unidirectional lamina. Figure 5.5 depicts the room temperature failure envelope comparison for the analysis conducted with and without thermal curing stresses. Once again, incorporating thermally induced cure stresses did not alter the failure envelope predictions by assuming a stress-free state under no mechanical load.

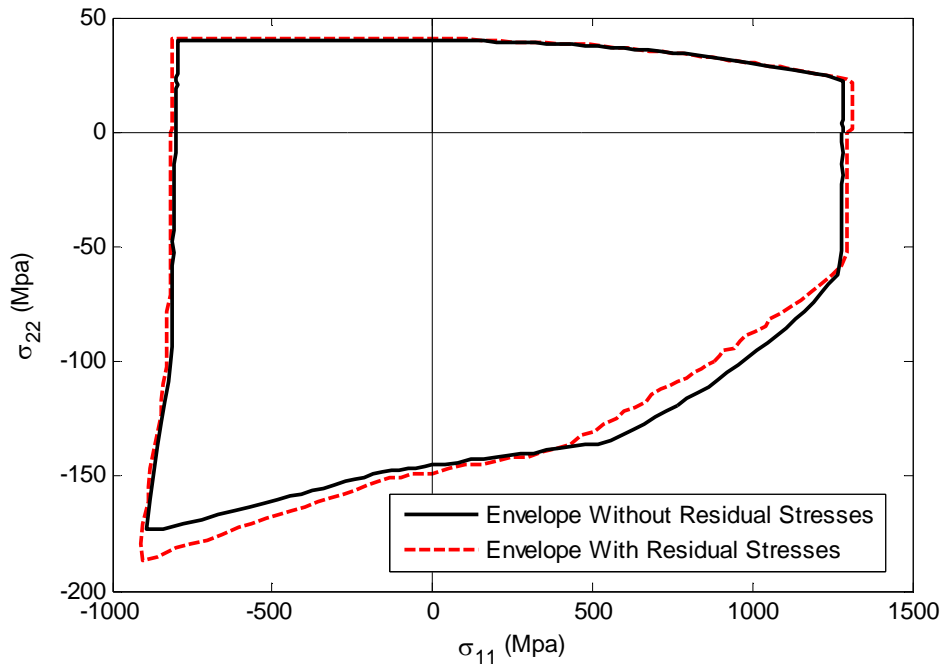


Figure 5.5 Room temperature failure envelope comparison for a Silenka/MY750 glass/epoxy unidirectional lamina.

The conclusion from Figures 5.3-5.5 is that residual stress effects from cure cycles on room temperature failure predictions are negligible for unidirectional composite materials whose failure strengths are determined from standard ambient reference temperature tests.

To enforce the importance of this result, it is useful to compare failure envelopes generated with and without thermal residual stresses utilizing the *purely mechanical failure coefficients*. Figure 5.6 provides this comparison for the biaxial glass/epoxy failure envelope that is also shown in Figure 5.5. The results clearly indicate the residual stresses are large enough in magnitude to alter the failure envelope, thereby predicting lower failure strengths. It must be emphasized that this apparent reduction in strength

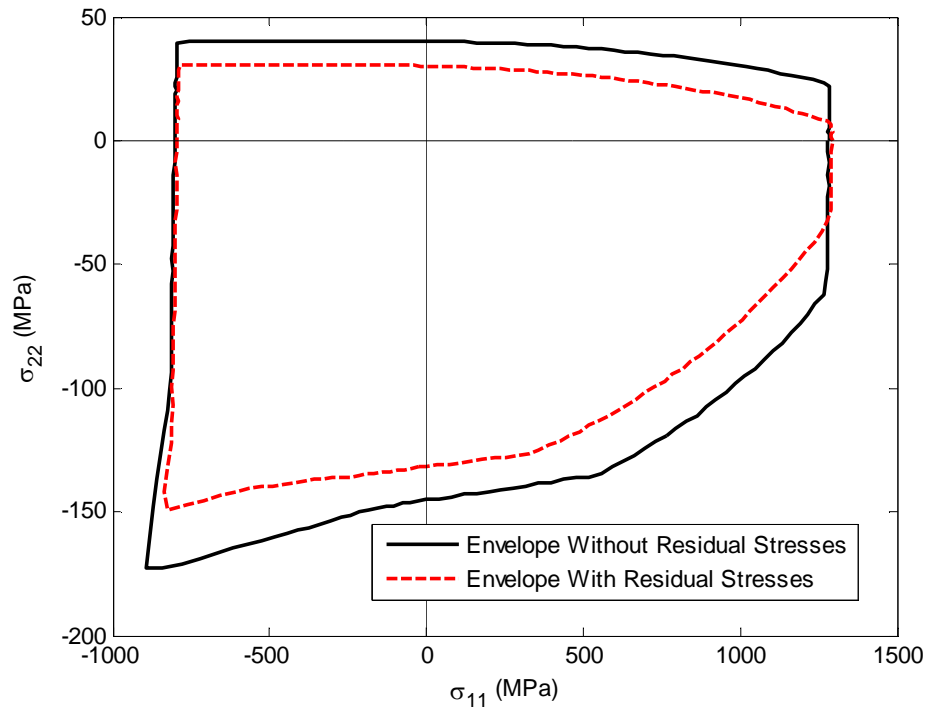


Figure 5.6 Room temperature failure envelope comparison incorporating only mechanical failure coefficients for a Silenka/MY750 glass/epoxy unidirectional lamina.

predictions is incorrect in that the effect of thermal stresses were neglected in the determination of the failure coefficients.

While the above discussion argues a very good case for neglecting the cure stresses in unidirectional lamina failure predictions, it does not guarantee that the effects of cure stresses can be neglected for multidirectional laminate predictions. To determine the effects of cure stresses in a laminate, a TTS analysis must be conducted for the laminate of interest. Such an analysis would require a TTS viscoelastic solution with MCT capability. Currently, MCT viscoelastic modeling is restricted to isothermal creep compliance material behavior.

While a detailed TTS analysis of multidirectional laminates cannot be conducted, we have investigated the significance of thermal stresses induced by mismatched thermal expansion of individual plies compared to thermally induced constituent level stresses within a ply. Table 5.4 compares the ply-level stresses and the constituent stresses for a $[90^\circ / \pm 30^\circ]_s$ EGlass/LY556 laminate subjected to a cool-down of 150°C assuming linear elastic behavior. The table shows stresses in the 90° ply only. In general, ply level thermal stresses are on the same order of magnitude as the thermally induced constituent stresses. Therefore, further investigation of thermal residual stresses for multidirectional laminates must be conducted.

Table 5.4 Comparison of ply level and constituent level stresses for a linear elastic cool-down of 150°C for a $[90^\circ / \pm 30^\circ]_s$ EGlass/LY556 laminate.

90° Ply Stresses			
Stress	Ply (MPa)	Fiber (MPa)	Matrix (MPa)
σ_{11}	-34.5	-60.7	4.83
σ_{22}	24.2	28.1	18.4
σ_{33}	1.51	0.198	3.48

5.3 Unidirectional Lamina Cryogenic Failure Envelope Comparisons

As discussed previously, an extremely large advantage of MCT is that constituent thermal stress contributions are completely accounted for in any thermomechanical problem. Hence, these self-equilibrating stresses generated in a thermal problem are readily available to an analyst. These stresses can have a pronounced effect on matrix failure predictions in particular, as thermal stresses alone can cause matrix cracking at cryogenic temperatures.

It is of interest to determine the effects of the residual stresses from a cure cycle at cryogenic temperatures. Here only carbon/epoxy laminates are considered as most glass/epoxy laminates cannot withstand such temperature changes because the strength of these material systems are not suited to cryogenic environments.

To analyze the effects of large temperature drops on failure predictions, the load cases of Section 5.2 were conducted at cryogenic temperatures with the T300/BSL914C carbon/epoxy whose properties are given in Table 5.3. Material properties and strength data were assumed to stay constant during the temperature change due to a lack of available low temperature data.

The temperature change chosen to model the thermal loading was $\Delta T = -150^{\circ}\text{C}$. Temperature changes larger than -150°C , such as cryogenic applications with liquid nitrogen ($\Delta T = -219^{\circ}\text{C}$), were not achievable as failure of the resin used in this material is predicted well before the complete temperature change could be reached.

The first load case considered was for longitudinal shear and transverse tension/compression of a unidirectional lamina with and without residual stresses from a cure cycle. Figure 5.7 depicts the failure envelope comparison for this load case. It is evident from the predictions that the large temperature change induces failure at

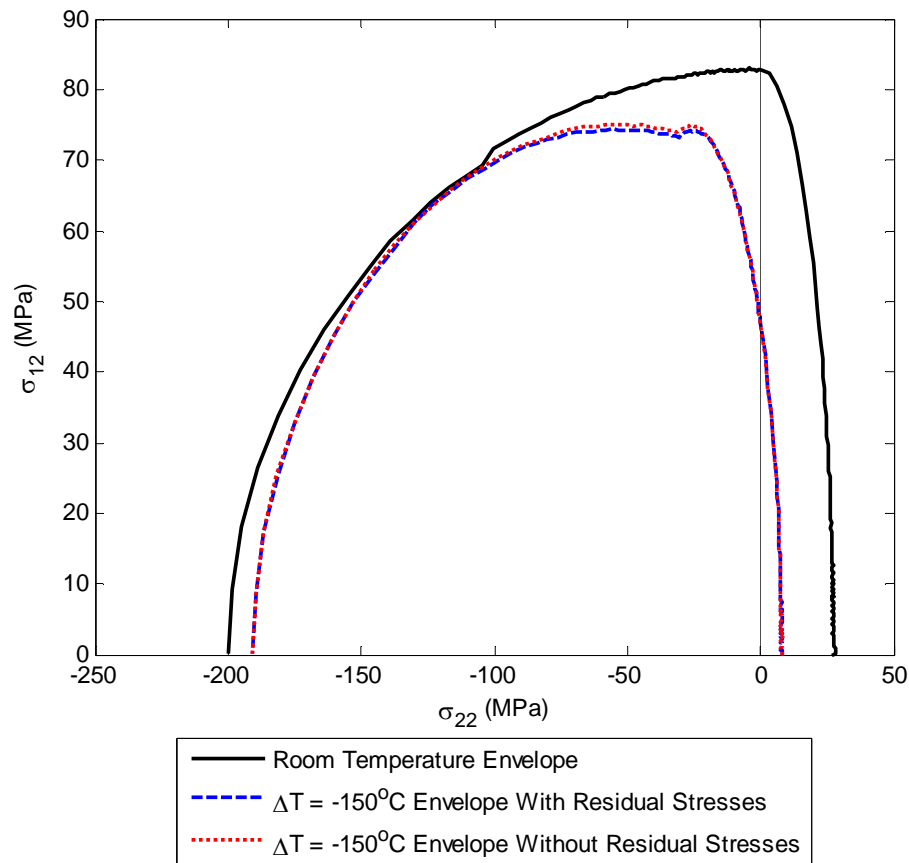


Figure 5.7 Failure envelope comparisons for a T300/BSL914C carbon/epoxy unidirectional lamina at cryogenic temperatures for combined transverse tension/compression and longitudinal shear.

significantly lower stress states. Furthermore, it is evident that the effects of the thermal residual stresses from a cure cycle are negligible.

Next, a failure envelope for longitudinal shear and longitudinal tension/compression was generated for a unidirectional lamina subjected first to a thermal load of $\Delta T = -150^{\circ}\text{C}$. A comparison of the failure envelope with and without residual stresses is depicted in Figure 5.8. The large temperature change induces failure early under longitudinal tension and combined longitudinal shear. However, the temperature change only slightly alters

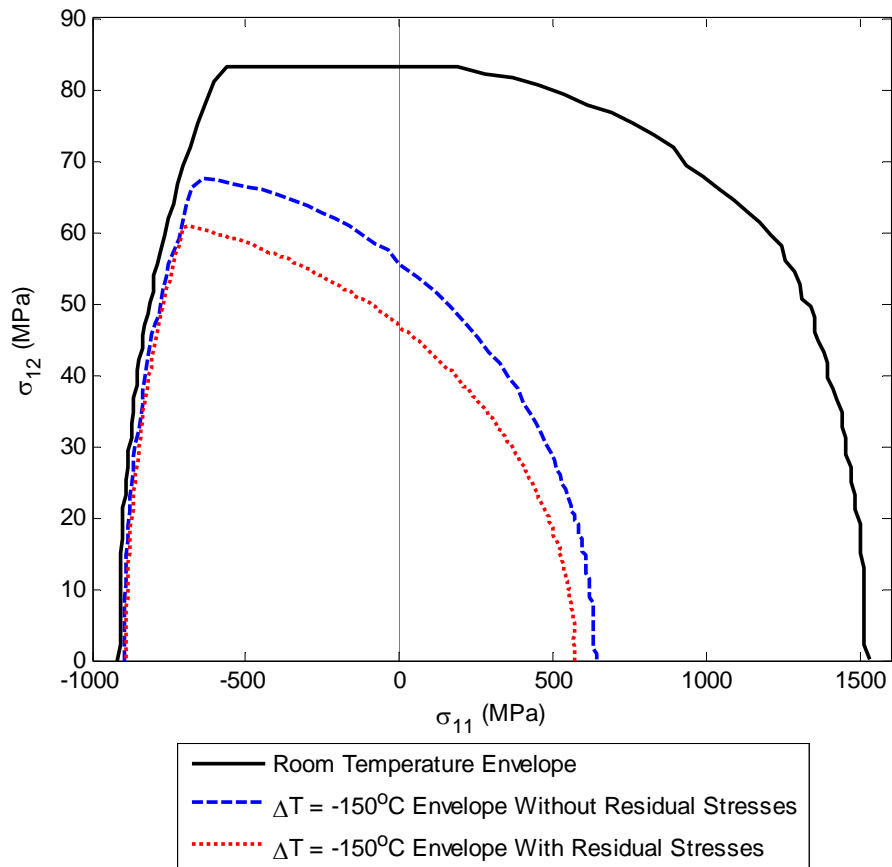


Figure 5.8 Failure envelope comparisons for a T300/BSL914C carbon/epoxy unidirectional lamina at cryogenic temperatures for combined longitudinal tension/compression and longitudinal shear.

the predictions under longitudinal compression. Moreover, the predictions incorporating thermal residual stresses from cure deviate from those not incorporating the cure stresses when the lamina is loaded in longitudinal shear.

The last loading considered was biaxial loading in the x_1 and x_2 directions. Figure 5.9 depicts failure envelope comparisons for reference temperature and $\Delta T = -150^\circ\text{C}$, respectively. The low temperature predictions show results for an assumed constituent

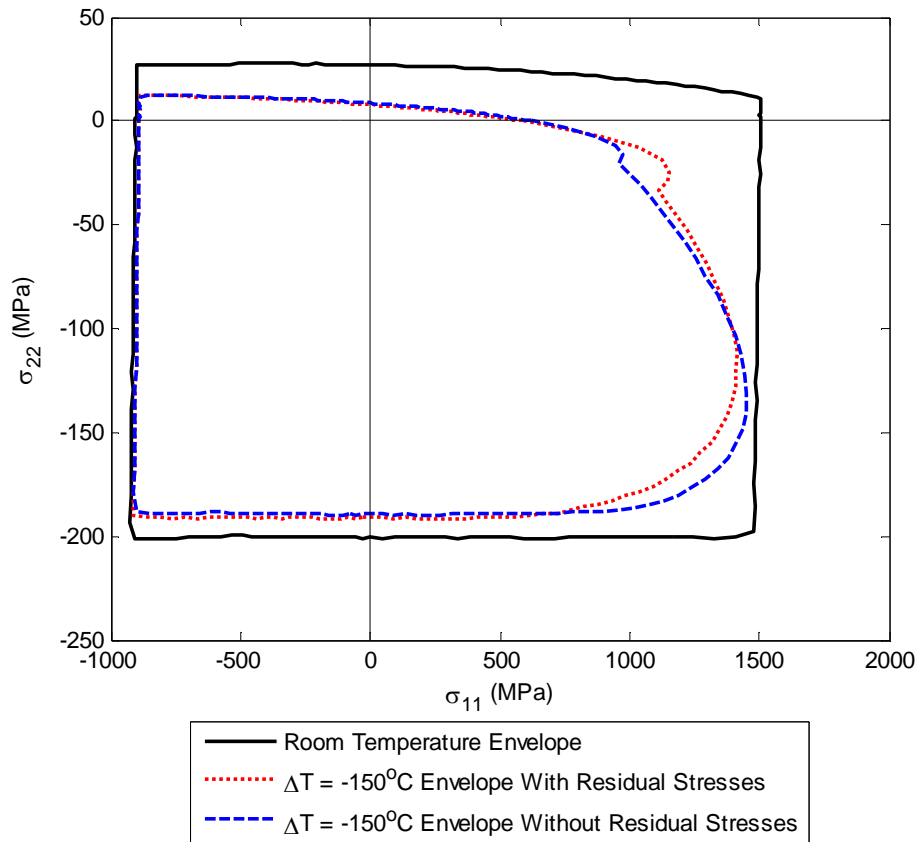


Figure 5.9 Failure envelope comparisons for a T300/BSL914C carbon/epoxy unidirectional lamina at cryogenic temperatures under biaxial loading.

stress-free state at reference temperature as well as incorporating residual stresses from a cure cycle.

Collectively, Figures 5.7 through 5.9 show that cure stresses have an effect on failure predictions at low temperatures involving longitudinal shearing and uniaxial longitudinal loading, while having a minimal effect on the other load cases studied. While cure stresses often have a negligible effect on failure predictions, the large self-equilibrating

thermal stresses caused by the $\Delta T = -150^\circ\text{C}$ cool-down dramatically alter the predicted failure envelopes.

Finally, in order to fully characterize a thermomechanical failure analysis at temperatures far from a reference state, an investigation of failure strengths at low temperatures should be conducted. Such a study should include temperature dependent material characterization in addition to determining failure strengths at the final temperature.

5.4 Laminate Cryogenic Failure Envelope Comparisons

The importance of thermal stresses arising from large temperature differences is also of interest in multidirectional laminates. In the absence of the capability to model cure stress effects using a TTS viscoelastic analysis, we adopt the assumption of a stress-free state at room temperature.

Two T300/BSL914C carbon/epoxy laminates consisting of a $[90^\circ / \pm 30^\circ]_s$ and a $[0^\circ / \pm 45^\circ / 90^\circ]_s$ were chosen to study low temperature effects on failure predictions. Hinton *et. al.* (2004) provide detailed descriptions of the laminate lay-ups, and all material properties are given in Table 5.3. Both configurations were loaded biaxially in the plane of the laminate after being exposed to a temperature change of -150°C , and the results were compared to the predictions for room temperature.

Figure 5.10 depicts the results for the $[90^\circ / \pm 30^\circ]_s$, while Figure 5.11 shows those for the $[0^\circ / \pm 45^\circ / 90^\circ]_s$ laminate. The figures show that large temperature changes have a distinct effect on matrix failure. The significance of thermal loads on matrix failure may be explained by the fact that matrix coefficients of thermal expansion are generally large, and consequently large temperature changes introduce significant thermal strains in the matrix. The resulting thermally induced matrix stresses, combined with the relatively low failure strengths of the matrix, have a prominent effect on matrix failure prediction.

In contrast to the matrix constituent, fiber failure is largely unaffected by the temperature change as the thermally induced fiber stresses are small compared to ultimate fiber failure strengths. Moreover, ultimate failure of multidirectional composite laminates studied here-in is generally predicted by fiber failure. As a result, there is little difference in the ultimate failure predictions at room temperature compared to the low temperature environment.

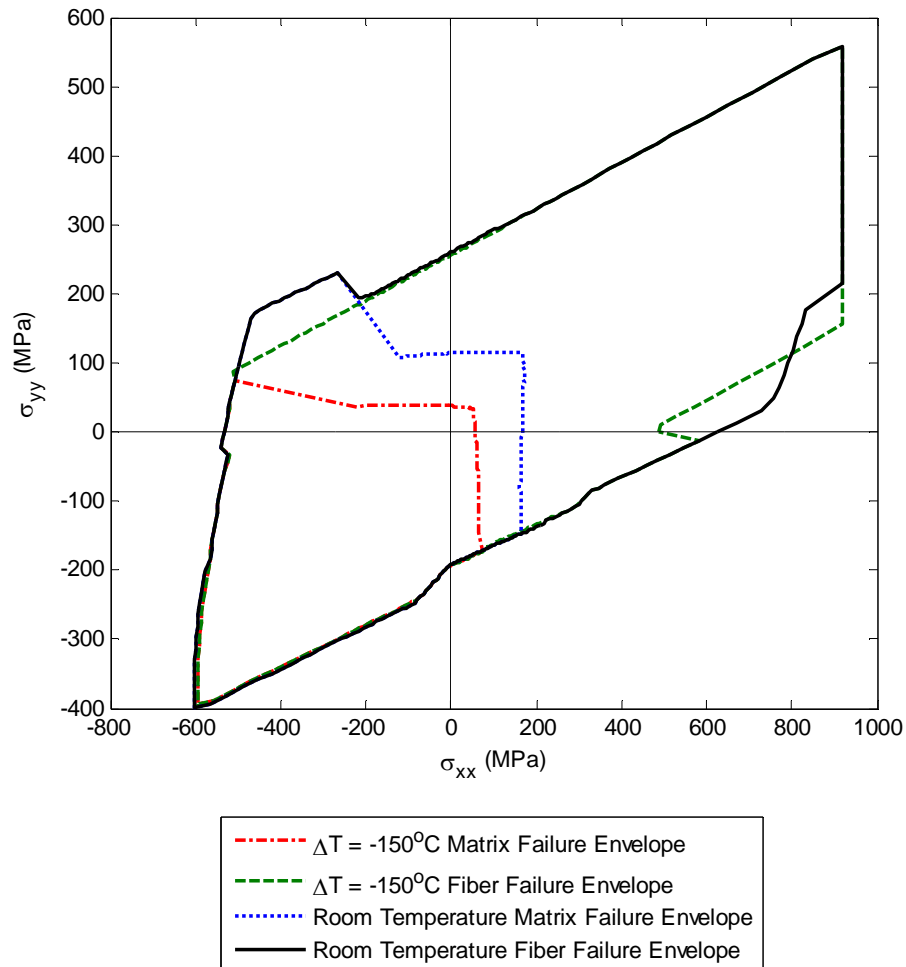


Figure 5.10 Biaxial failure envelope comparison for a $[90^\circ / \pm 30^\circ]_s$ T300/BSL914C laminate at $\Delta T = -150^\circ\text{C}$ and room temperature.

While considering matrix failure may seem trivial in the context of ultimate failure loads, many aerospace applications utilize multidirectional composites laminates similar to those considered here to store liquids and gasses in cryogenic environments. If the matrix cracks, these fluids may “weep” from the laminate and could produce a catastrophic failure and/or precious loss of liquid fuels.

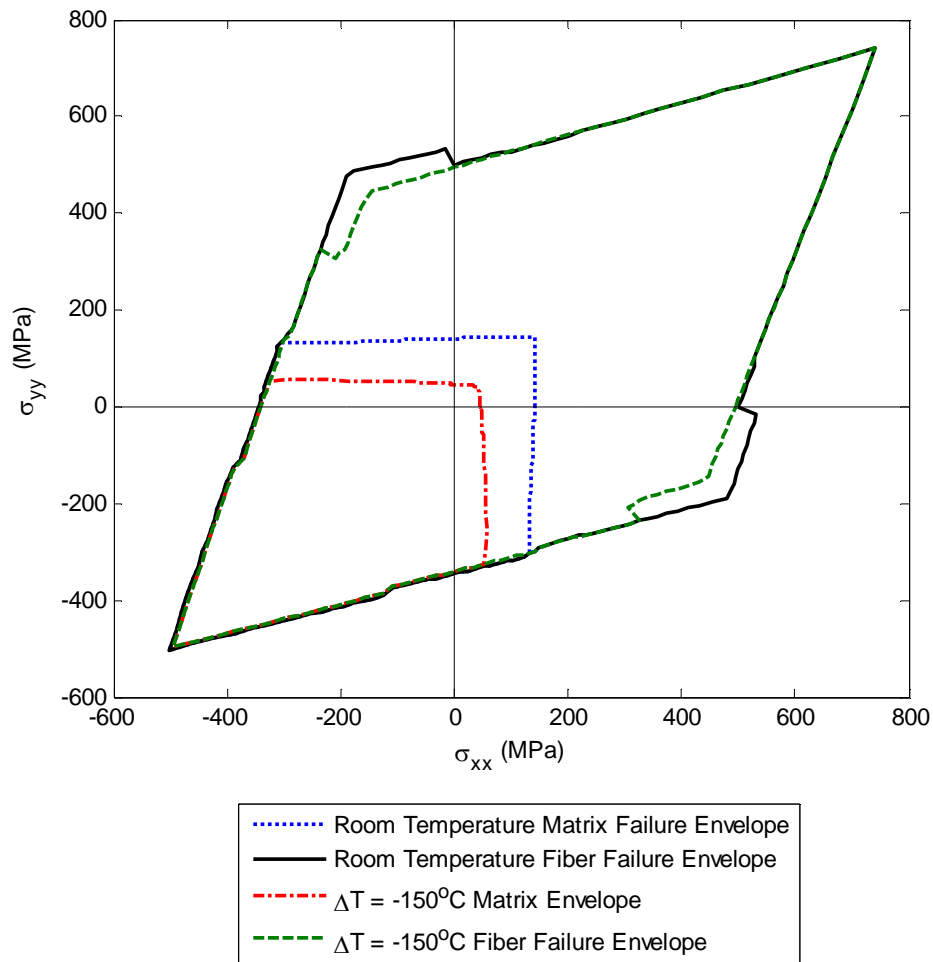


Figure 5.11 Biaxial failure envelope comparison for a $[0^\circ / \pm 45^\circ / 90^\circ]_s$ T300/BSL914C laminate at $\Delta T = -150^\circ\text{C}$ and room temperature.

The conclusion then is that thermal constituent stresses must be accounted for in any thermomechanical problem where the environment deviates substantially from the assumed stress-free reference temperature. The ability to capture thermal stresses at the constituent level is a hallmark of MCT that truly separates the analysis from conventional finite element analysis.

6. ORTHOTROPIC MATERIAL DEGRADATION

In an MCT progressive failure analysis of a composite laminate, failure mechanisms cross multiple geometric scales. Specifically, ultimate (catastrophic) failure of a laminate is often preceded by failure and/or intermediate damage occurring within individual lamina. Ply-level failure itself is multi-scale in nature as failure within a lamina may take the form of fiber failure or matrix failure.

When considering constituent failure mechanisms within an individual lamina, fiber failure and matrix failure are treated differently. In the case of the fibers, linear elastic behavior is assumed up to a critical failure load. The subsequent failure is assumed to result in a complete loss of load carrying capacity, and fiber material properties are set to near zero values with loads redistributed to neighboring plies.

In contrast to fiber failure, matrix failure within a ply is much more complex. Damage is assumed to occur at loads well below ultimate failure and initiate in the form of submicrocrack (void) accumulation. This type of damage is well documented in polymer behavior (Zhurkov and Kuksenko, 1974) and results in nonlinear stress-strain behavior at the macroscopic level. As loads continue to increase, the matrix reaches a critical stress state, typically resulting in transverse cracking within the laminate. In the case of unidirectional composites, a transverse crack (failure) in the matrix is assumed catastrophic for the entire laminate. However, in the case of multidirectional laminates matrix failure is not catastrophic in that the deformation near the crack zone is highly localized and the constituent is able to support loads a short distance from the crack

through complex load paths utilizing adjacent plies. The post-failure response of the matrix is characterized by an increasing number of transverse ply cracks. Eventually, a crack saturation limit is reached where the matrix has largely lost its load carrying capacity. Knopps and Bögle (2004) used a unique set of experiments to quantify the material phenomenon of increasing transverse crack density in a post matrix failure response.

Inelastic behavior caused by the variety of matrix deformation mechanisms noted above is further complicated by the effect damage has on the matrix material properties. In an undamaged state, the matrix is assumed to be isotropic. Submicrocrack accumulation is assumed to affect the longitudinal shear behavior of the matrix, immediately causing the matrix to be transversely isotropic. The presence of transverse ply cracks introduces an even more complex matrix response that is *orthotropic* in nature.

6.1 Ply-Level Material Degradation

6.1.1 Submicrocrack (Void) Accumulation

In the present MCT failure analysis, nonlinearity caused by submicrocrack accumulation, such as typically seen in longitudinal shear behavior of unidirectional composite laminates, is modeled as follows. Material degradation is assumed to be driven by the longitudinal shear contribution to the matrix failure criterion given by

$$\eta_{Sm} = A_4^m I_4^m \quad . \quad (6.1)$$

At low levels of η_{Sm} , the matrix material properties are assumed linear elastic, implying that low levels of stress cause no damage. However, upon exceeding a threshold value of η_{Sm} , the composite moduli are degraded functionally as

$$G_{13}^d = G_{12}^d = G_{12}^d(\eta_{Sm}) \quad , \quad (6.2)$$

where the superscript d denotes a degraded property. The degradation curve defined by Equation (6.2) is determined functionally from composite longitudinal shear stress-strain data.

When composite properties are altered due to matrix damage, the properties of the matrix material must also be degraded in order to maintain consistent relationships through the micromechanics analysis. This consistency is enforced *a priori* to structural analysis by generating composite material property curves as a function of matrix damage. The development of these curves begins with isotropic matrix material properties, say E_m and G_m , representing Young's modulus and the shear modulus, respectively. Modulus G_m is allowed to degrade in longitudinal shear to G_{13m}^d and G_{12m}^d . Transverse isotropy is enforced, requiring

$$G_{12m}^d = G_{13m}^d \quad . \quad (6.3)$$

Given the degradation scheme outlined above, it is a straightforward matter to relate degraded composite longitudinal shear properties to degraded matrix longitudinal shear properties as functions of simple curves for any composite material (Mayes, 1999).

These curves are generated by repeated execution of the micromechanics material property module with steadily decreasing values of the matrix longitudinal shear moduli.

6.1.2 Transverse Cracking

A critical aspect of modeling the development of transverse ply cracks of increasing crack density is to determine the effect of the cracks on the matrix material properties and the composite properties of the lamina. A schematic of a transverse ply crack is shown in Figure 6.1 where a unit normal to the crack is oriented in the x_2 direction of the lamina.

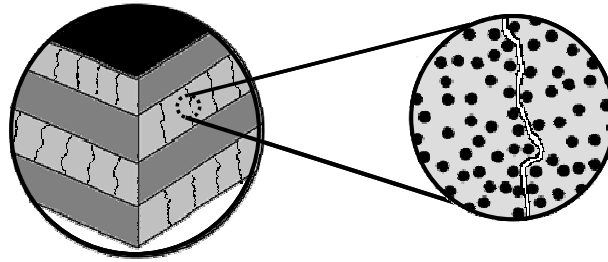


Figure 6.1 Schematic of transverse ply cracking, Akula (2007).

Akula (2007) presented work on ply-level material degradation as a function of increasing transverse ply crack density. Finite element micromechanics models of increasing crack density were developed and a set of periodic boundary conditions were enforced to model transverse cracking through the thickness of a ply within a laminate. The results were compared to a range of experimental data, and it was found that the micromechanics model predicted ply level material degradation in very good agreement with experimental data. A significant result of Akula's work was that only selected ply level material properties were found to degrade as a function of increasing crack density.

In particular, if the fibers of the ply are aligned with the x_1 direction, it was found that of 9 possible independent orthotropic constants, only 5 constants given by E_2 , ν_{21} , ν_{23} , G_{12} and G_{23} were found to degrade in the presence of transverse ply cracks. Furthermore, an equally important observation was that E_2 , ν_{21} , and ν_{23} were found to degrade by a consistent percentage as a function of increasing crack density.

Now consider the compliance matrix for an orthotropic matrix material. Since principal material axes are aligned with the local (lamina) axes, one can write

$$[S] = \begin{bmatrix} 1/E_1 & -\nu_{12}/E_1 & -\nu_{13}/E_1 & 0 & 0 & 0 \\ -\nu_{12}/E_1 & 1/E_2 & -\nu_{23}/E_2 & 0 & 0 & 0 \\ -\nu_{13}/E_1 & -\nu_{23}/E_2 & 1/E_3 & 0 & 0 & 0 \\ 0 & 0 & 0 & 1/G_{12} & 0 & 0 \\ 0 & 0 & 0 & 0 & 1/G_{13} & 0 \\ 0 & 0 & 0 & 0 & 0 & 1/G_{23} \end{bmatrix} . \quad (6.4)$$

Note that even though ν_{21} is changing as a function of crack density, ν_{12} does not. This result can be proven by considering the Maxwell-Betti theorem as

$$\frac{\nu_{12}^d}{E_1^d} = \frac{\nu_{21}^d}{E_2^d} . \quad (6.5)$$

Since the modulus E_1 is not affected by transverse cracks, the above can be rearranged to give

$$\nu_{12}^d = E_1 \frac{\nu_{21}^d}{E_2^d} . \quad (6.6)$$

Because ν_{21} and E_2 are degraded by the same amount, ν_{12} does not change as a function of transverse crack density.

Now consider S_{23} of the compliance matrix given by

$$S_{23} = -\frac{v_{23}^d}{E_2^d} . \quad (6.7)$$

Since both v_{23}^d and E_2^d degrade by the same percentage, this term is also unaffected by transverse cracks. In summary, a degraded compliance matrix takes the form

$$[S^d] = \begin{bmatrix} 1/E_1 & -v_{12}/E_1 & -v_{13}/E_1 & 0 & 0 & 0 \\ -v_{12}/E_1 & 1/E_2^d & -v_{23}/E_2 & 0 & 0 & 0 \\ -v_{13}/E_1 & -v_{23}/E_2 & 1/E_3 & 0 & 0 & 0 \\ 0 & 0 & 0 & 1/G_{12}^d & 0 & 0 \\ 0 & 0 & 0 & 0 & 1/G_{13} & 0 \\ 0 & 0 & 0 & 0 & 0 & 1/G_{23}^d \end{bmatrix} . \quad (6.8)$$

The surprising conclusion is that only 3 diagonal terms in the compliance matrix are affected by degradation due to transverse cracks.

6.2 Orthotropic Degradation

Figures 6.2 through 6.4 depict the findings of Akula for material property degradation as a function of normalized transverse crack density, given by

$$\zeta = \frac{\# \text{ cracks}}{\text{millimeter}} * h ,$$

where h represents the thickness of the lamina in *millimeters*. Note that a value of $\zeta = 1$ implies the distance between cracks is equal to the thickness of the ply. The work

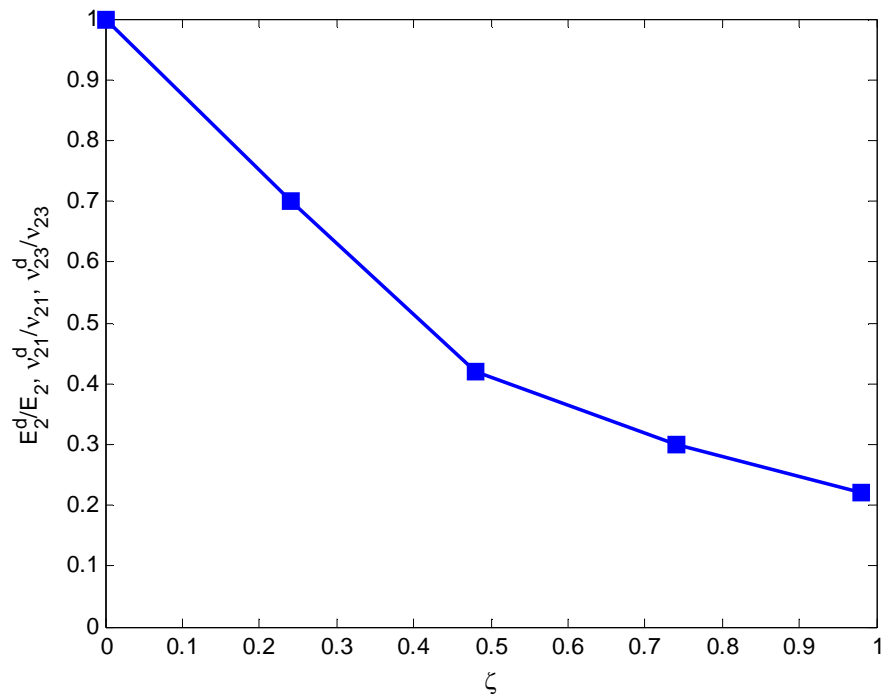


Figure 6.2 E_2^d/E_2 , ν_{21}^d/ν_{21} , and ν_{23}^d/ν_{23} lamina degradation as a function of normalized transverse crack density as presented by Akula (2007). Symbols represent FEA data.

completed by Akula considers normalized transverse crack densities up to 1.0, as most experimental data used for comparison did not consider crack densities greater than this.

It is obvious from Figures 6.2 through 6.4 that material degradation does not stay constant for normalized crack densities greater than 1.0. To extend degradation functions beyond 1.0, the data presented was extrapolated using a “best eye fit” until a leveling off of degraded properties was achieved, which was identified as crack saturation.

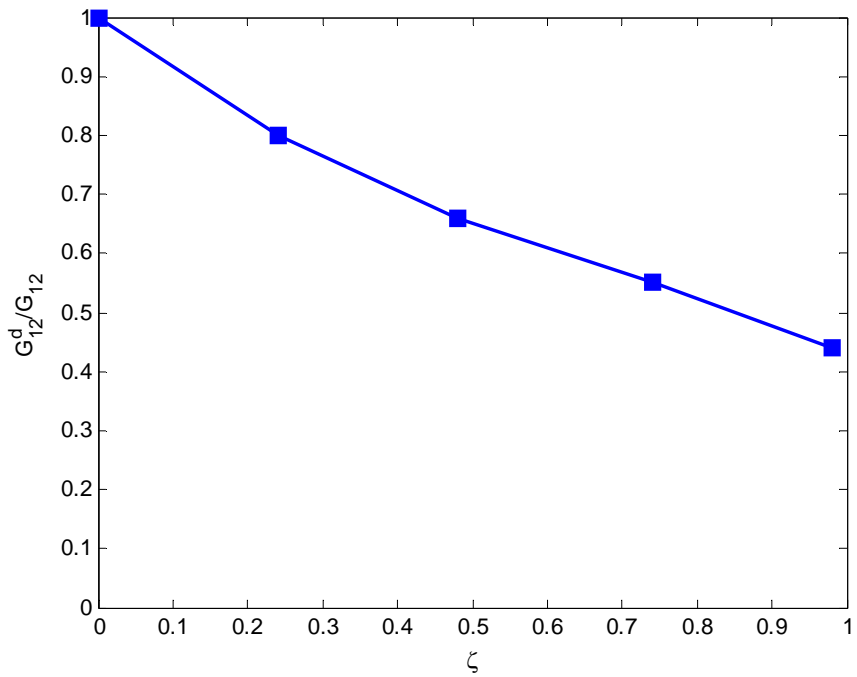


Figure 6.3 G_{12}^d/G_{12} lamina degradation as a function of normalized transverse crack density as presented by Akula (2007). Symbols represent FEA data.

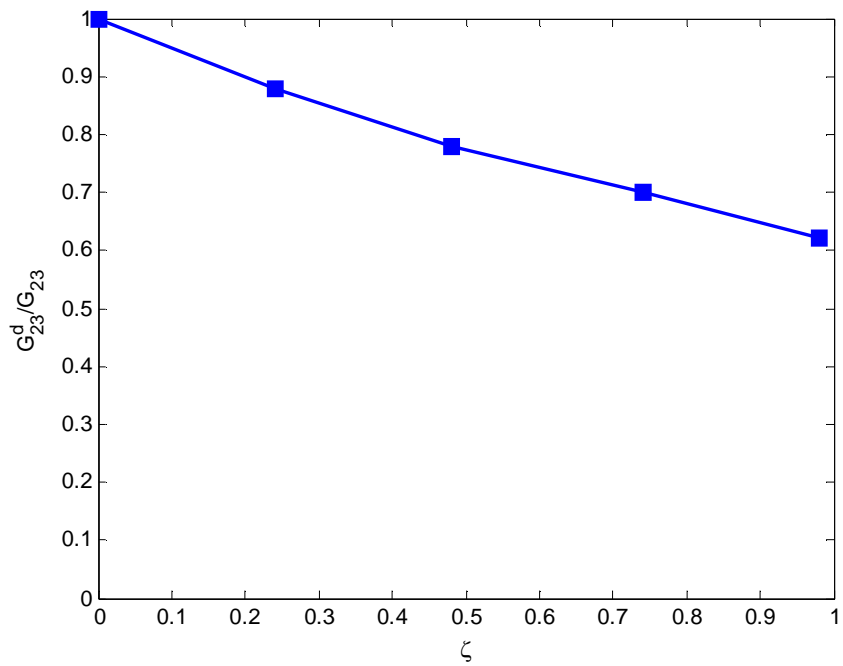


Figure 6.4 G_{23}^d/G_{23} lamina degradation as a function of normalized transverse crack density as presented by Akula (2007). Symbols represent FEA data.

6.2.1 Degradation Parameters

For the purposes of an MCT progressive failure analysis, it is necessary to have *both* the matrix and composite mechanical property degradation as a function of transverse crack density to enforce a consistent relationship between matrix and composite properties. To accomplish this, a program was implemented following the development in Key (2000) in which orthotropic matrix material properties could be “reverse engineered” from known composite and reinforcement material data using an iterative process. The process was completed for both glass/epoxy and carbon/epoxy laminae, as fiber reinforcement properties strongly influence matrix degradation. Figures 6.5 - 6.7 depict matrix and composite degradation as a function of normalized transverse crack density. It is assumed that the glass/epoxy and carbon/epoxy lamina material properties generated here represent the entire collection of their respective reinforcement and matrix combinations.

From Figures 6.6 and 6.7, it is clear that matrix shear stiffness degradation is independent of the type of reinforcement used, and thus only analytical representations of four curves need be developed for the matrix degradation parameters. Namely, one for glass/epoxy E_2 and ν_{23} , one for carbon/epoxy E_2 and ν_{23} , one for G_{12} , and one for G_{23} . Analytical representations of the three composite curves in Figures 6.5 through 6.7 must also be developed.

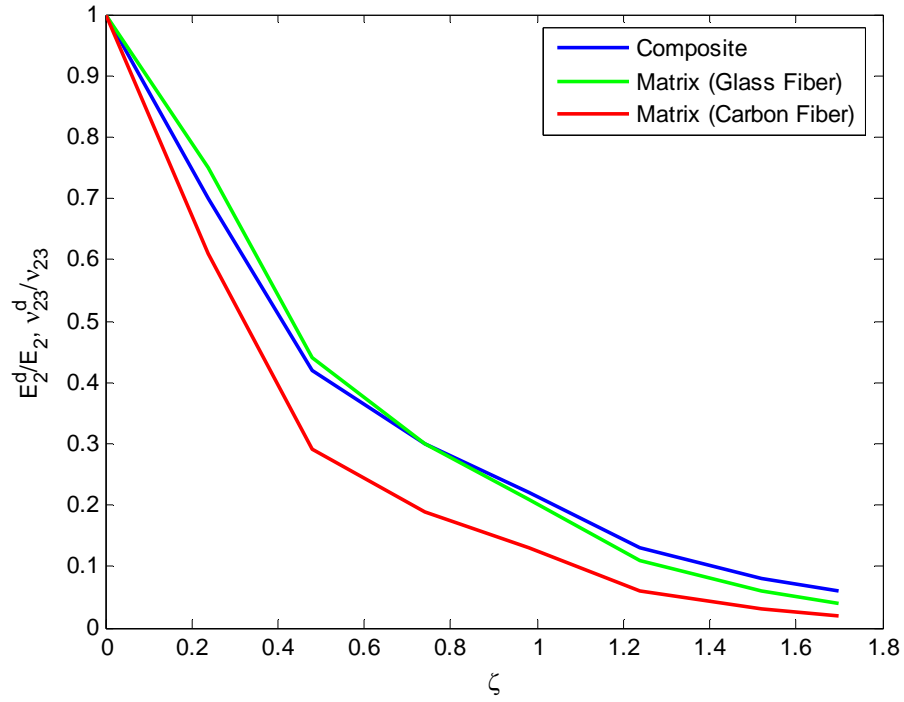


Figure 6.5 E_2^d/E_2 and ν_{23}^d/ν_{23} as a function of normalized transverse crack density.

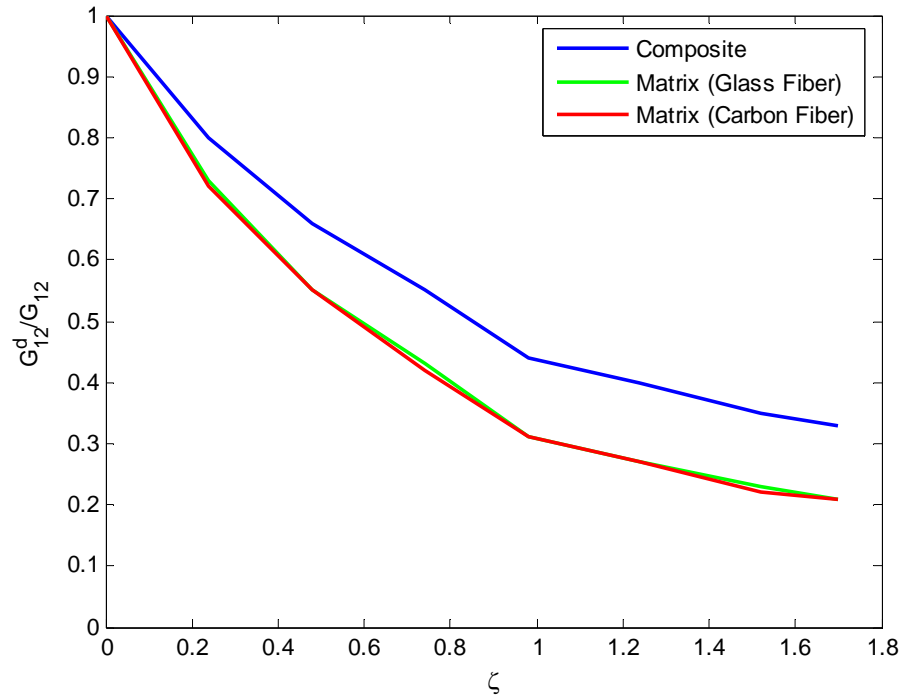


Figure 6.6 G_{12}^d/G_{12} as a function of normalized transverse crack density.

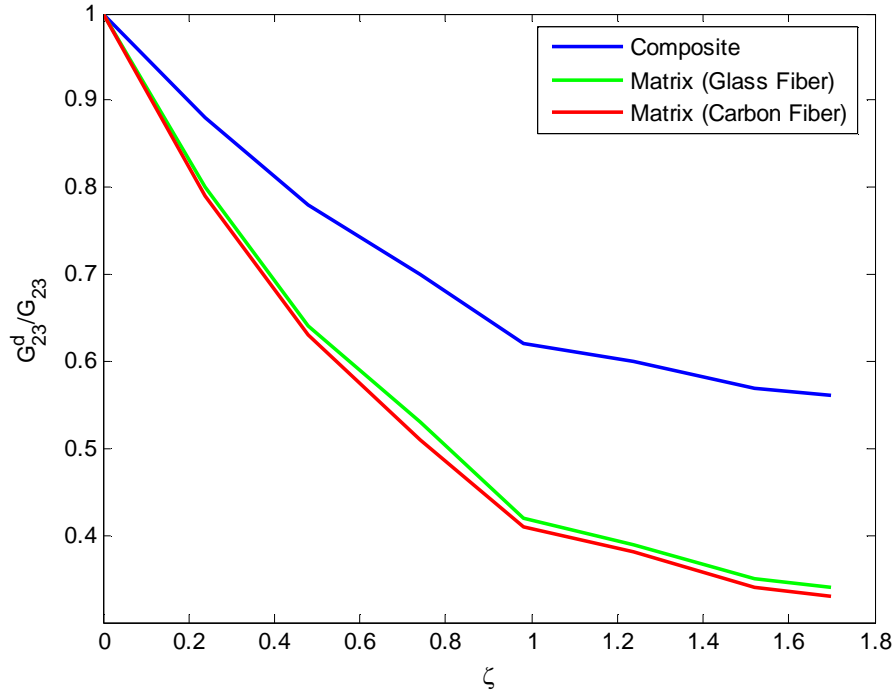


Figure 6.7 G_{23}^d/G_{23} as a function of normalized transverse crack density.

While knowing degraded property curves as a function of crack density describes the material behavior of the matrix and homogenized composite to its full extent, determining the transverse crack density after failure is a difficult task to accomplish. In order to relate transverse crack density to easy calculated parameters during a routine analysis, a strain measure was chosen to model the crack density. In particular, consider the third strain invariant of the matrix constituent given by

$$I_3^m = (\varepsilon_{22}^m)^2 + (\varepsilon_{33}^m)^2 + 2(\varepsilon_{23}^m)^2 \quad . \quad (6.9)$$

The third invariant was chosen to relate to transverse crack density because the invariant is a function of transverse normal strains and transverse shear strain.

To give an identifiable measure of transverse crack density, the third strain invariant was calculated for the matrix at composite transverse tension failure and set to a value ψ_0 . Then the same parameter was calculated for subsequent crack densities at the same composite stress state, denoted by ψ , and degradation curves were generated for the matrix as a function of $(\psi - \psi_0)^{1/3}$. The exponent of 1/3 was chosen to produce curves that were easily fit to a simple polynomial. Figures 6.8 - 6.10 show matrix and composite degradation as a function of $(\psi - \psi_0)^{1/3}$.

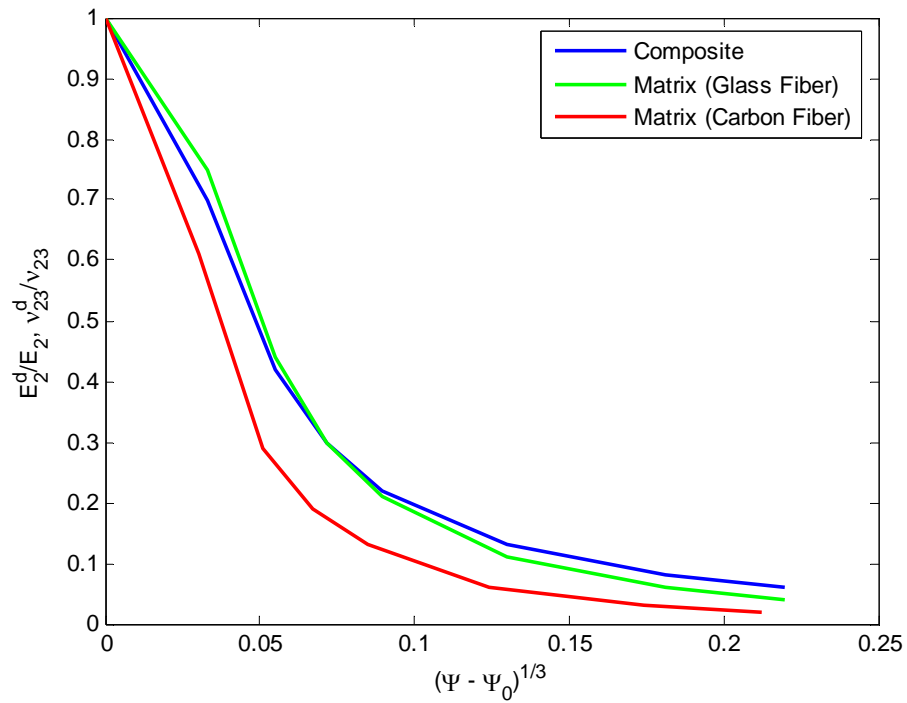


Figure 6.8 E_2^d/E_2 and ν_{23}^d/ν_{23} as a function of the third strain invariant.

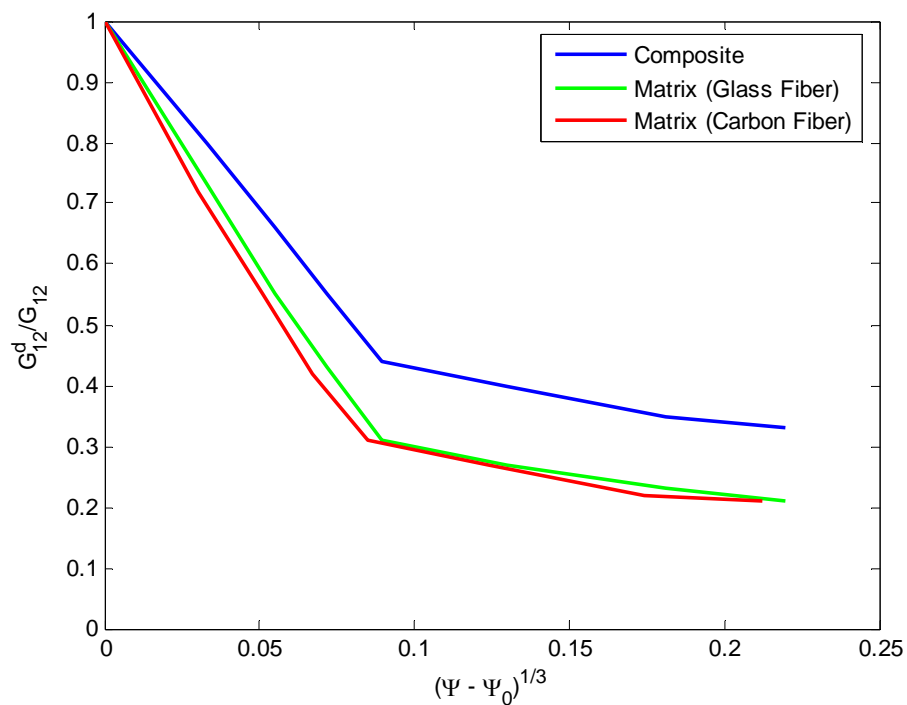


Figure 6.9 G_{12}^d/G_{12} as a function of the third strain invariant.

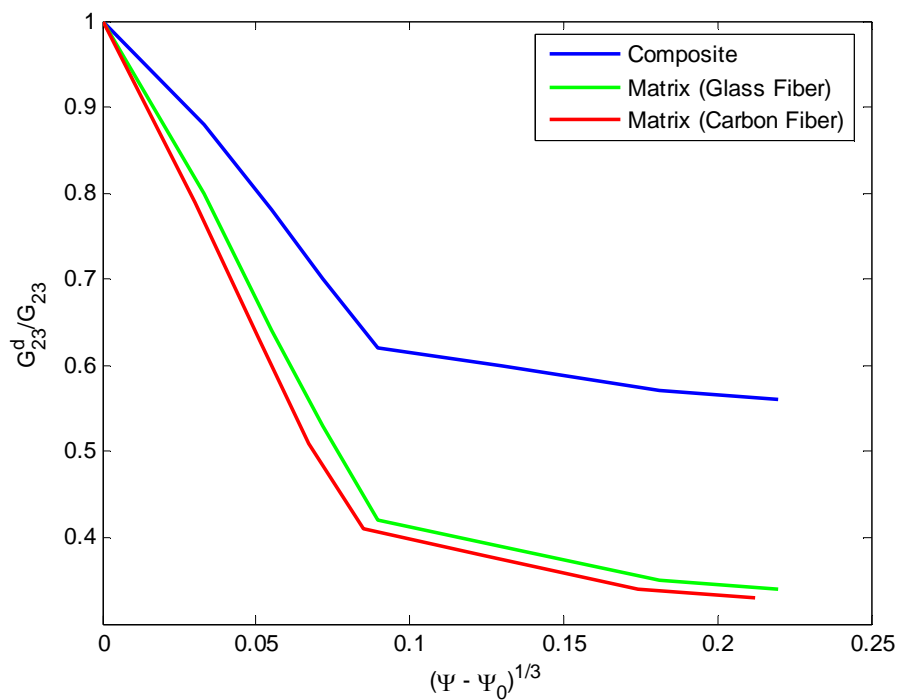


Figure 6.10 G_{23}^d/G_{23} as a function of the third strain invariant.

Table 6.1 details the curve fitting coefficients for the composite, and Table 6.2 provides the coefficients for matrix. The composite degradation can be modeled by

$$\varphi^c = 1 + C_1 z + C_2 z^2 + C_3 z^3 + C_4 z^4, \quad (6.10)$$

and the matrix degradation can be modeled by

$$\varphi^m = 1 + C_1 z + C_2 z^2 + C_3 z^3 + C_4 z^4 + C_5 z^5, \quad (6.11)$$

where z is the strain parameter $(\psi - \psi_0)^{1/3}$, and φ is the reduction multiplier to the original material property of interest.

Table 6.1 Lamina curve fitting coefficients for composite degradation based on Equation (6.10).

E_2^d/E_2 ν_{23}^d/ν_{23}			
C_1	C_2	C_3	C_4
104.7	-147.5	69.74	-13.60
G_{12}^d/G_{12}			
C_1	C_2	C_3	C_4
34.22	-71.11	40.09	-8.82
G_{23}^d/G_{23}			
C_1	C_2	C_3	C_4
-50.22	5.130	15.10	-5.060

Table 6.2 Matrix curve fitting coefficients for matrix degradation based on Equation (6.11).

E_2^d/E_2 and ν_{23}^d/ν_{23} for Glass Fiber Reinforcement				
C_1	C_2	C_3	C_4	C_5
0.0000	102.0	-135.5	64.73	-13.14
E_2^d/E_2 and ν_{23}^d/ν_{23} for Carbon Fiber Reinforcement				
C_1	C_2	C_3	C_4	C_5
-363.5	666.17	-439.8	132.3	-18.52
G_{12}^d/G_{12}				
C_1	C_2	C_3	C_4	C_5
-123.1	241.4	-182.3	66.25	-11.67
G_{23}^d/G_{23}				
C_1	C_2	C_3	C_4	C_5
0.00	116.0	-134.2	56.29	-10.20

6.2.2 Degradation Under Transverse Compression

Transverse compression is fundamentally different than transverse tension when considering the formation of cracks. Specifically, transverse compression can be thought to push cracks together instead of pull them apart. At first blush, the distinction between compressive and tensile behavior is important as tensile induced cracks will cause a reduction in stiffness. Under compression transverse cracks will close and one may expect no stiffness reduction due to *cracking*. Puck (1998) and Liu and Tsai (1998) both realized this fundamental difference in crack behavior and adjusted material properties accordingly.

A similar approach to Puck (1998), and Liu and Tsai (1998), was initially investigated to model transverse cracking in the present work. Recall, the second transversely isotropic invariant for the matrix stress tensor is given by

$$I_2^m = \sigma_{22}^m + \sigma_{33}^m \quad . \quad (6.12)$$

This invariant was calculated for the matrix to form an identifier for transverse compression. If $I_2^m < 0$, the matrix was assumed to be in transverse compression as compressive stresses are dominating, whereas $I_2^m > 0$ was assumed to be a tensile dominated stress state.

Given a value for I_2^m , matrix and composite transverse stiffness E_2^m and E_2^c were only degraded when I_2^m was found to be positive. This approach was utilized to generate a variety of failure envelopes for known experimental data. For comparison, a second set of results were generated by degrading E_2^c and E_2^m under transverse compression. It was

found that degrading transverse stiffness properties in tension and compression produced a more realistic failure envelope. This phenomenon can be explained by assuming the matrix behaves plastically under compressive loading. Plastic behavior can produce a nonlinear response very similar to that caused by cracking. Based on these results, the dependence of the second stress invariant was thrown out, and all material properties were degraded regardless of the transverse loads being tensile or compressive.

6.3 Implementation of the Post-Failure Response for Transverse Cracking

The orthotropic degradation scheme outlined in Section 6.2 is essentially a post-failure response based on increasing density of transverse cracks. The implementation of this model begins when initial failure is detected in the matrix. At initial failure, the third transversely isotropic strain invariant is calculated from Equation (6.9) and stored for use in all subsequent calculations. The value of the third matrix strain invariant at initial failure is denoted by ψ_0 . For every subsequent load increment, if the current value of ψ exceeds the maximum recorded value of ψ , material property degradation is calculated for the matrix and composite from the curves described in Section 6.2, and compliance matrices are reformulated according to Equation (6.8).

If submicrocrack damage has occurred from shear nonlinearities prior to initial matrix failure, cracking damage is assumed to compound the degradation. Hence, the values of G_{12} and G_{12}^m at failure represent the “original” values of G_{12} and G_{12}^m for degradation calculations due to cracking.

The progressive failure analysis continues in this manner until either fiber failure is detected within the ply, or matrix saturation is detected. For the latter case, further deformation results in the material properties being held constant at the lowest calculated values. For fiber failure, the lamina is considered completely failed, and the fiber material properties are set to zero.

6.4 Results

Given the numerical degradation method outlined above with the MCT constituent-based failure criteria, the multidirectional laminate load cases from the WWFE were run to determine the accuracy of the orthotropic degradation algorithm. Here, chosen failure predictions are compared to those of a prior version of the MCT constituent-based failure criteria and known experimental data. There are two important distinguishing features of the orthotropic degradation scheme developed here compared to the previous MCT constituent-based progressive failure analysis. First, degradation in the previous analysis required transverse isotropy of the composite and matrix properties. Akula (2007), has clearly shown that the assumption of transverse isotropy in the matrix is not general enough in that under transverse cracking

$$E_2 \neq E_3 \quad .$$

A second important feature of the current orthotropic degradation scheme is that all stress-strain behavior is treated as being continuous. In contrast, the prior version of the MCT constituent-based progressive failure analysis utilized piecewise continuous stress-strain curves that allowed for jumps in the secant modulus. This approach was adopted for numerical efficiencies.

For discussion purposes, the term “transversely isotropic” (TI) will be used to identify the previous MCT constituent-based progressive failure analysis approach. All lay-up configuration information is detailed in Hinton *et. al.* (2004), and the material properties used are given in Tables 5.1, 5.2, and 5.3.

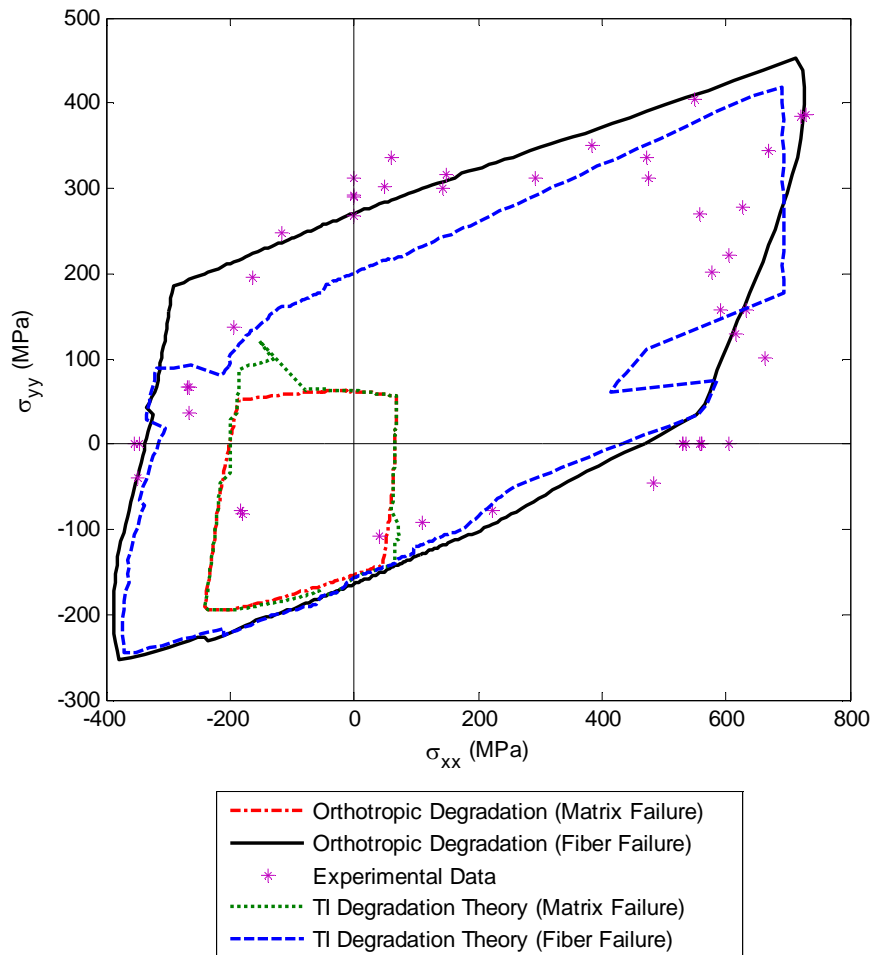


Figure 6.11 Biaxial failure envelope comparison for a $[90^\circ / \pm 30^\circ]_s$ EGlass/LY556 laminate.

Figure 6.11 compares predictions of a $[90^\circ / \pm 30^\circ]_s$ glass/epoxy laminate loaded biaxially in the x and y directions. Also, Figure 6.12 gives a comparison for a $[90^\circ / \pm 30^\circ]_s$ glass/epoxy laminate loaded under combined longitudinal tension/compression and

longitudinal shear. It is obvious from these figures that the failure envelopes developed using the orthotropic degradation algorithm predict failure much more accurately than the TI progressive failure theory.

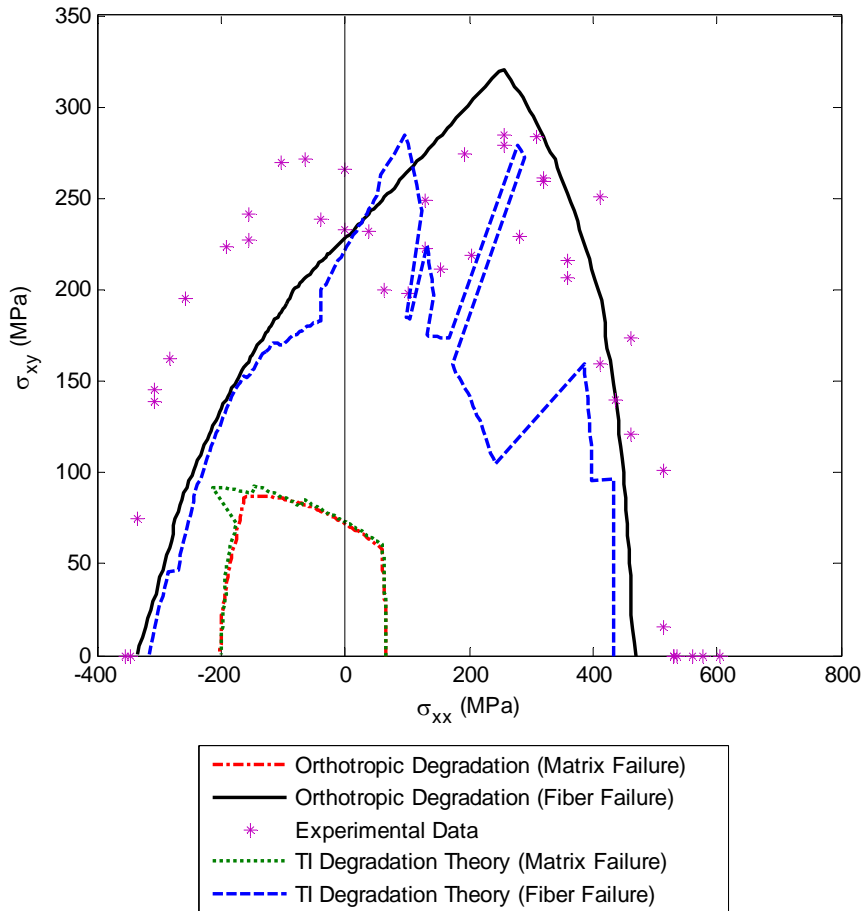


Figure 6.12 Failure envelope comparison for a $[90^\circ / \pm 30^\circ]_s$ EGlass/LY556 laminate.

Furthermore, the theory using orthotropic degradation predicts a smooth failure envelope, while the TI theory predicts one that is choppy. The choppy appearance of the TI envelope can be attributed to the use of conditionals when post-failure degradation is employed within the TI theory. The conditionals cause degradation parameters to be turned on or off depending on the strains encountered within the composite. Thus, when

composite straining from different loading is on either side of the conditional statement, a discontinuous failure surface is formed.

Figure 6.13 depicts a comparison for stress-strain curves of a $[\pm 55^\circ]_s$ EGlass/MY750 laminate loaded biaxially under $\sigma_{xx}:\sigma_{yy} = 1:2$. This loading configuration was chosen because it exhibits extreme amounts of nonlinearity after initial matrix failure, and transverse cracking is considered a large factor in the nonlinear response. Note the experimental and theoretical strains in the x direction differ by a large amount for strains in excess of 1%. While strains above this limit will rarely be designed for, it is useful to compare this data with other sources of experimental data to give insight to the discrepancies. In particular, the experiments conducted by Knopps and Bögle (2004) for the same laminate and loading yielded data closely resembling that produced by the orthotropic degradation curves.

Figure 6.14 highlights the same curves of Figure 6.13 for strains only up to 0.9% for a more detailed comparison. The results indicate that degrading material properties orthotropically results in a theoretical prediction in very good agreement to the experimental data, particularly for strains up to 0.5%, which are still considered large. A prominent and undesirable feature of the TI approach is the very large jumps in strain occurring near $\sigma_{yy} = 250 \text{ MPa}$.

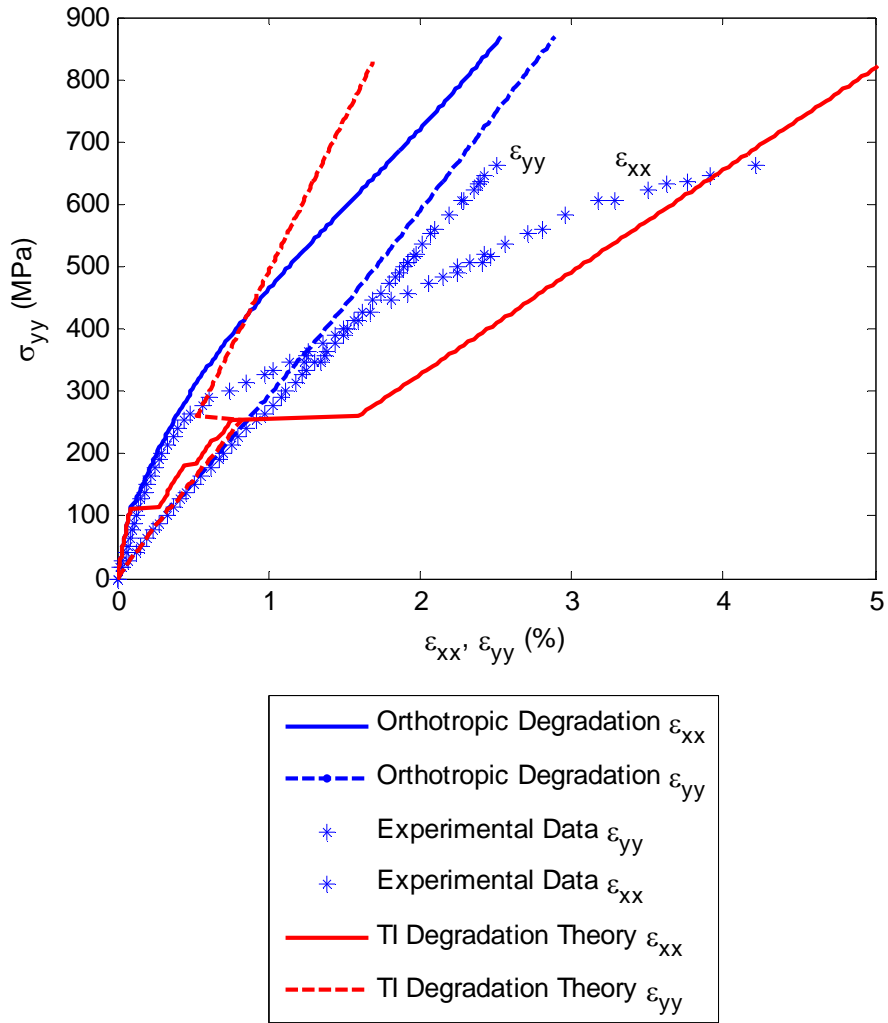


Figure 6.13 Stress-strain curve comparison for a $[\pm 55^\circ]_s$ EGlass/MY750 laminate loaded under $\sigma_{xx}:\sigma_{yy} = 1:2$.

Finally, consider loading of a $[\pm 55^\circ]_s$ EGlass/MY750 laminate under $\sigma_{xx}:\sigma_{yy} = 0:1$ as shown in Figure 6.15. This loading configuration produces substantial nonlinear shearing and transverse cracking within the plies. As such, the loading configuration tests the ability to couple submicrocracking and transverse cracking during a progressive failure analysis.

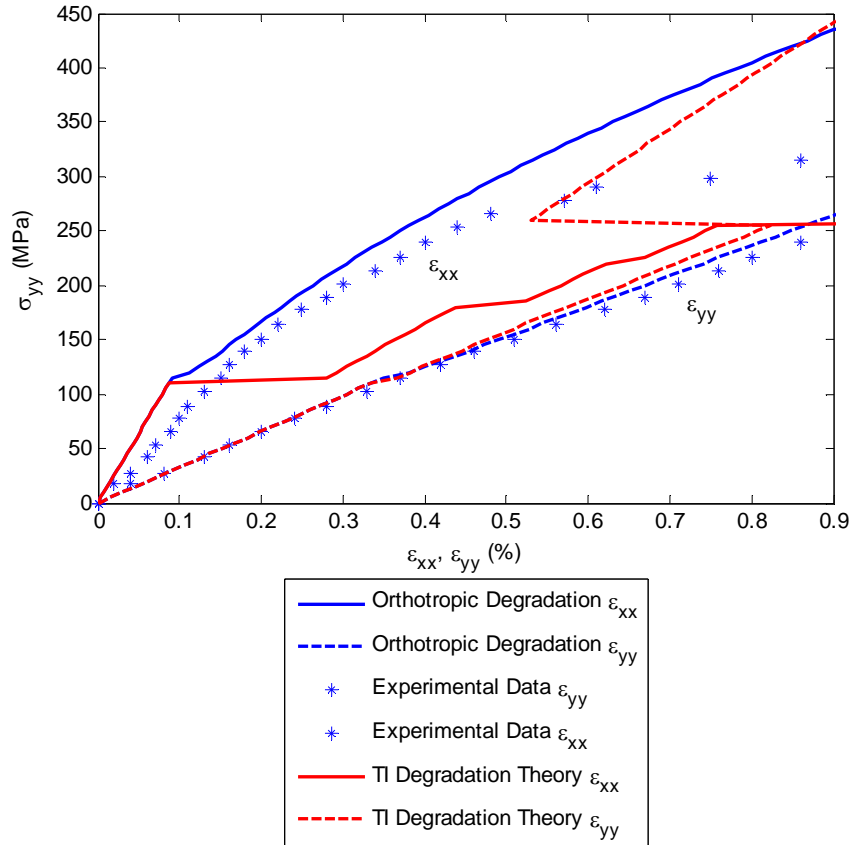


Figure 6.14 Close up stress-strain curve comparison for a $[\pm 55^\circ]_s$ EGlass/MY750 laminate loaded under $\sigma_{xx}:\sigma_{yy} = 1:2$.

The orthotropic degradation approach developed in this thesis performs extremely well for strains approaching 1.5%. These strains are extremely large and are likely well in excess of any strains encountered for service loads of such a structure.

In conclusion, the numerical orthotropic degradation progressive failure analysis modeled after the work of Akula (2007) was implemented into the MCT constituent-based failure criterion as outlined in this chapter. Laminate failure envelope predictions for the orthotropic degradation model compares favorably with results from the WWFE.

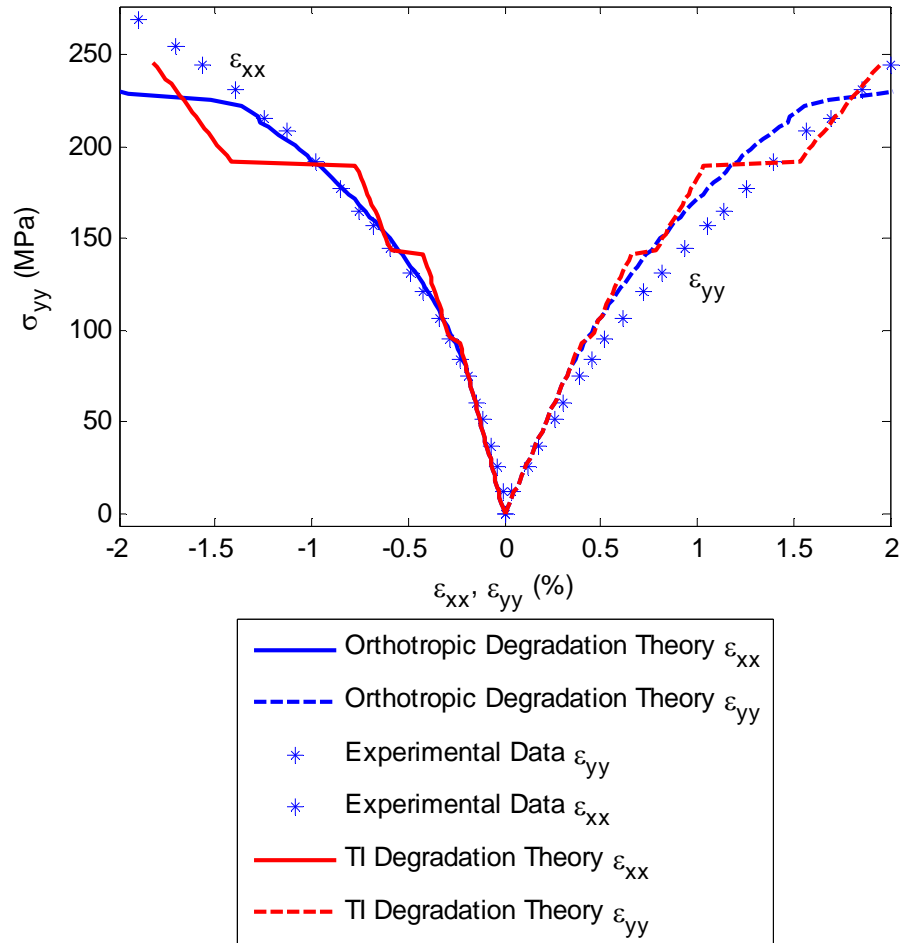


Figure 6.15 Stress-strain curve comparison for a $[\pm 55^\circ]_s$ EGlass/MY750 laminate loaded under $\sigma_{xx}:\sigma_{yy} = 0:1$.

Two important features of the orthotropic degradation scheme are the continuous nature of the stress-strain curves along with the ability to generalize degradation from transverse isotropy to orthotropy. Moreover, the theory captures the critical failure mechanisms known to occur in progressive failure including submicrocrack damage, transverse matrix cracking, crack saturation, and ultimately fiber failure.

7. CONCLUSIONS AND RECOMMENDATIONS

The entire basis of this thesis has been to provide means to enhance the progressive failure analysis of composite structures under combined thermomechanical loading by the use of numerically efficient techniques. A detailed discussion of several advanced techniques for progressive failure analysis of composite structures has been presented.

7.1 Micromechanics Enhancements

An optimized micromechanics model was created to calculate composite material properties from those of the constituents. The analysis was completed by use of an in-house finite element code. Numerical procedures aimed at reducing the size of the global stiffness matrix were carried out in an attempt to decrease solution times. Results were remarkable in that thermoelastic properties for a composite may be computed on the order of milliseconds.

The micromechanics model was then extended to allow for time and temperature dependent material properties. The matrix was taken to be a temperature dependent viscoelastic material, while the fibers were assumed to be linear elastic. Time-temperature-superposition (TTS) was implemented within the finite element formulation.

A consideration for future work is to decrease solution speeds for the TTS viscoelastic micromechanics model. An avenue worth exploring is partitioning the elastic modulus into sets defined by temperatures. Partitioning the elastic modulus into discrete sets will allow the global stiffness matrix to be factorized at specific time increments as opposed to every time increment, thereby decreasing solution times dramatically. Furthermore, assembling the elemental load vectors for the flow strain as discussed in Appendix A will further increase solution speeds.

Another micromechanics problem spiking interest in the composite materials community is the analysis of composite weaves. Woven fabric composite materials consist of two-dimensional, and even three-dimensional, fiber tows that interlace to form a complex microstructure. Simply obtaining macroscopic material properties has become a very large obstacle due to a paucity of experimental data.

Finite element micromechanics provides a powerful means to predict mechanical properties of weaves with complex microstructures. For instance, each fiber tow, or bundle, is merely a two-constituent continuous fiber composite whose longitudinal direction is constantly changing orientation due to the undulation of the tows. Therefore, the weave bundle properties may be readily computed using a continuous fiber micromechanics model such as the hexagonal packed model used here-in. A micromechanics model of the entire weave, using the previously computed bundle

properties, provides a means of predicting thermomechanical properties. Key (2000) provides an excellent example of micromechanics modeling of a plain weave.

The techniques used to decrease solution times for the hexagonally packed micromechanics model can be extended to a micromechanics model of a weave. The potential gains in solution time for such a micromechanics model are far greater than those of the hexagonally packed unit cell, as a weave micromechanics model represents a complex geometry that involves a greater number of nodes, elements, and periodic multipoint constraints.

7.2 Effects of Cure Stresses on Composite Laminates

In order to evaluate the significance of residual thermal stresses caused by fabrication, a cure cycle modeling a temperature cool-down from a resin set temperature was conducted. Failure envelopes incorporating residual cure stresses were computed for three unidirectional composites. Results indicate that failure strength data at ambient temperature inherently accounts for the effect of residual cure stresses.

Unlike unidirectional composites, multidirectional laminates present an added dimension of difficulty in a cure stress study because ply level residual stresses are generated in addition to constituent level residual stresses with a ply. An analysis of cure stresses in multidirectional laminates requires extending the TTS algorithm of the micromechanics

analysis to accommodate anisotropic viscoelastic behavior of a composite lamina. The work completed thus far lays the groundwork to extend the TTS theory to laminates. Specifically, the micromechanics model incorporated with TTS can be used to generate master curves for a unidirectional laminate, and these can be used to compute the stress/strain field for a cool-down of a multidirectional laminate.

7.3 Analysis of Failure at Cryogenic Temperatures

Cryogenic environments place composite materials under severe thermal loads and are commonly encountered in the aerospace industry. The mismatch of ply-level thermomechanical properties give rise to ply stresses, and the mismatch of constituent thermomechanical properties gives rise to large interaction stresses between the constituents. To provide insight on the effects of such environments on failure, an investigation of cryogenic temperatures was conducted for both unidirectional laminae and multidirectional laminates assuming a carbon/epoxy composite.

From the results for unidirectional laminates, it was found that cryogenic temperatures have a large impact on matrix dominated failure and fiber dominated tensile failure, while fiber dominated compressive failure is hardly impacted. Residual stresses caused during curing may have an effect on specific load cases and should be considered when possible.

Failure envelopes were also generated for multidirectional laminates under cryogenic temperature loadings. It was found that such temperature changes have a large effect on matrix failure when compared to predictions at room temperature, while fiber failure is largely unaltered. An investigation of residual cure stresses for multidirectional laminates at cryogenic temperatures could not be completed due to the lack of accurate ply-level stresses from a cure cycle.

Finally, to fully characterize the failure of unidirectional laminae at cryogenic temperatures, thermomechanical properties and strengths should be generated at such environments to allow for accurate failure predictions.

7.4 Orthotropic Degradation

Damage progression involving orthotropic degradation of the matrix material under transverse cracking was implemented to the multi-continuum theory (MCT) constituent-based progressive failure analysis. The specific form of orthotropic degradation of the matrix was based on detailed experimental and analytical work in accordance with the results obtained from Akula (2007). The resulting failure envelopes and stress-strain curves compared very well against known experimental data.

An important failure mechanism that has not been studied here-in is that of delamination, or separation, of adjacent plies. Future work in the area of degradation includes

extending the degradation scheme to account for delamination, thus helping to account for a very complex failure mechanism in multidirectional laminates.

7.5 Progressive Failure at Elevated Temperatures

Finally, an important extension to the work completed in this thesis is to model the impact of the “hot-wet” environment on progressive failure of composite structures, where large temperature swings and moisture diffusion have the ability to induce failure much earlier than ambient conditions. Composite structures routinely see elevated temperature environments with moisture, and moisture diffusion produces similar effects to thermal loads.

In order to complete a progressive failure analysis of composite structures in the hot-wet environment, many factors must be considered in the analysis of the failure propagation. In particular, TTS must be incorporated for multidirectional laminates, and failure propagation must be modeled with the use of viscoelasticity. Furthermore, moisture effects, as well as thermal effects, would have to be incorporated in the analysis. To compound the problem further, constituent strengths may be heavily dependent on moisture and temperature.

The hot-wet failure problem poses a serious challenge to accurately model. However, the techniques developed in this thesis provide the fundamental groundwork to launch such an effort.

REFERENCES

- ABAQUS, 2007, ABAQUS Theory Manual, SIMULIA, Providence, RI
- Akula, Venkata M. K., 2007, Constitutive Modeling of Damaged Unidirectional Composite Laminae, Ph.D. Dissertation, University of Wyoming, Department of Mechanical Engineering
- Christensen, Richard M., 1982, Theory of Viscoelasticity an Introduction, 2nd Ed., Academic Press, Inc., New York, NY
- Cook, R. D., D. S. Malkus, M. E. Plesha and R. J. Witt, 1974, Concepts and Applications of Finite Element Analysis, 4th Ed., John Wiley and Sons, Inc., New York, NY
- Cuntze, R. G. and A. Freund, 2004, “The Predictive Capability of Failure Mode Concept – Based Strength Criteria for Multidirectional Laminates,” Composites Science and Technology, Vol.64, pp.343-377
- Curiskis, J. I. and S. Valliappan, 1978, “A Solution Algorithm for Linear Constraint Equations in Finite Element Analysis,” Computers and Structures, Vol.8, pp.117-124
- Dalgarno, Richard W., 2007, Thermal Fatigue Induced Microcracking in Graphite-Epoxy Laminated Composites, M.S. Thesis, University of Wyoming, Department of Mechanical Engineering
- Garnich, M. R., 1996, A Multicontinuum Theory for Structural Analysis of Composite Materials, Ph.D. Dissertation, University of Wyoming, Department of Mechanical Engineering
- Garnich, M. R. and A. C. Hansen, 1997, “A Multicontinuum Approach to Structural Analysis of Linear Viscoelastic Composite Materials,” Journal of Applied Mechanics, Vol. 64, pp.795-803
- Gotsis, P. K., C. C. Chamis, and L. Minnetyan, 1998, “Prediction of Composite Laminate Fracture: Micromechanics and Progressive Fracture,” Composites Science and Technology, Vol. 58, pp.1137-1150
- Hansen, A. C., D. M. Blackketter, and D.E. Walrath, 1991, “An Invariant-Based Flow Rule for Anisotropic Plasticity Applied to Composite Materials,” Journal of Applied Mechanics, Vol.58, pp.881-888
- Hashin, Z., 1980, “Failure Criteria for Unidirectional Fiber Composites,” Journal of Applied Mechanics, Vol.47, pp.329-334
- Hill, R., 1950, The Mathematical Theory of Plasticity, Oxford University Press, New York, NY

- Hinton, M. J., A. S. Kaddour, and P. D. Soden, 2004, Failure Criteria in Fibre Reinforced Polymer Composites: The World-Wide Failure Exercise, Elsevier Ltd., Oxford, England
- Huang, Z. M., 2004, "A Bridging Model Prediction of the Tensile Strength of Composite Laminates Subjected to Biaxial Loads," Science and Technology, Vol. 64, pp.395-448
- Key, C. T, 2000, A Progressive Failure Analysis of a Plain Weave, Woven Roving, Composite Material, M.S. Thesis, University of Wyoming, Department of Mechanical Engineering
- Knopps, M. and C. Bögle, 2004, "Gradual Failure in Fibre/Polymer Laminates," Composites Science and Technology, Vol.66, pp.616-625
- Lakes, Roderic S, 1999, Viscoelastic Solids, CRC Press LLC., Boca Raton, FL
- Laws, N., 1980, "Physics of Modern Materials," International Atomic Energy, Series SMR-46/107, pp.465-520
- Liu, K-S and S. W. Tsai, 1998, "A Progressive Quadratic Failure Criterion of a Laminate," Composites Science and Technology, Vol. 58, pp.1023-1032
- Mayes, J. S, 1999, Multicontinuum Failure Analysis of Composite Structural Laminates, Ph.D. Dissertation, University of Wyoming, Department of Mechanical Engineering
- Mayes, J. S. and A. C. Hansen, 2002, "A Comparison of Multicontinuum Theory Based Failure Simulation with Experimental Results," Composites Science and Technology, Vol. 64, pp.517-527
- Mayes, J. S. and A. C. Hansen, 2004, "Composite Laminate Failure Analysis Using Multicontinuum Theory," Composites Science and Technology, Vol. 64, pp.379-394
- Puck, A. and H. Schürmann, 1998, "Failure Analysis of FRP Laminates by Means of Physically Based Phenomenological Models," Composites Science and Technology, Vol. 58, pp.1045-1068
- Puck, A., J. Kopp and M. Knops, 2001, "Guidelines for the Determination of the Parameters in Puck's Action Plane Strength Criterion," Composites Science and Technology, Vol.62, pp.371-378
- Press, W. H., S. A. Teukolsky, W. T. Vetterling and B. P. Flannery, 2007, Numerical Recipes: The Art of Scientific Computing, 3rd Ed., Cambridge University Press, Cambridge, NY
- Rotem, A., 1998, "Prediction of Laminate Failure with Rotem Failure Criterion," Composites Science and Technology, Vol. 58, pp.1083-1094

- Seifert, Ole E., 2002, Structural Analysis of a Plain Open Weave Composite at Elevated Temperatures, M.S. Thesis, University of Wyoming, Department of Mechanical Engineering
- Sloan, S.W., 1986, "An Algorithm for Profile and Wavefront Reduction of Sparse Matrices," International Journal for Numerical Methods in Engineering, Vol.23, pp.239-251
- Wilson, Edward L., 1973, "The Static Condensation Algorithm," Short Communications, pp.198-203
- Zhurkov, S. N. and V. S. Kuksenko, 1974, "The Micromechanics of Polymer Fracture," International Journal of Fracture, Vol.11, pp.629-639
- Zhurkov, S. N., 1965, "Kinetic Concept of the Strength of Solids," International Journal of Fracture Mechanics, Vol.1, No.4, pp.311-322

APPENDIX A. MATRIX MULTIPLICATION PARTITIONING

The finite element method requires the formulation of element stiffness matrices of the form

$$[K_e] = \int_V [B]^T [C] [B] dV , \quad (\text{A.1})$$

where $[B]$ is the strain-displacement matrix and $[C]$ is the material stiffness matrix. For an 8-node isoparametric element, $[B]$ and $[C]$ have dimensions 6×24 and 6×6 , respectively.

Following the work of Chapter 3, these matrices may be partitioned into a collection of 3×3 submatrices of the form

$$[C] = \begin{bmatrix} C_{11} & 0 \\ 0 & C_{22} \end{bmatrix} , \quad (\text{A.2})$$

and

$$[B] = \begin{bmatrix} B_{11}^1 & B_{11}^2 & B_{11}^3 & B_{11}^4 & B_{11}^5 & B_{11}^6 & B_{11}^7 & B_{11}^8 \\ B_{21}^1 & B_{21}^2 & B_{21}^3 & B_{21}^4 & B_{21}^5 & B_{21}^6 & B_{21}^7 & B_{21}^8 \end{bmatrix} . \quad (\text{A.3})$$

Utilizing the partitioned forms of $[B]$ and $[C]$, direct expansion of Equation (A.1) leads to

$$[K_e] = \int_V \begin{bmatrix} B_{11}^1{}^T C_{11} B_{11}^1 + B_{21}^1{}^T C_{22} B_{21}^1 & \cdots & B_{11}^1{}^T C_{11} B_{11}^8 + B_{21}^1{}^T C_{22} B_{21}^8 \\ \vdots & \ddots & \vdots \\ B_{11}^8{}^T C_{11} B_{11}^1 + B_{21}^8{}^T C_{22} B_{21}^1 & \cdots & B_{11}^8{}^T C_{11} B_{11}^8 + B_{21}^8{}^T C_{22} B_{21}^8 \end{bmatrix} dV , \quad (\text{A.4})$$

where all apparent zero multiplications have been eliminated. Because the material principal axes are orientated with the global axes, C_{11} is a symmetric matrix given by

$$C_{11} = \begin{bmatrix} c_{11} & c_{12} & c_{13} \\ c_{12} & c_{22} & c_{23} \\ c_{13} & c_{23} & c_{33} \end{bmatrix}, \quad (\text{A.5})$$

whereas C_{22} is a diagonal matrix given by

$$C_{22} = \begin{bmatrix} c_{44} & 0 & 0 \\ 0 & c_{55} & 0 \\ 0 & 0 & c_{66} \end{bmatrix}. \quad (\text{A.6})$$

Also, B_{11}^i can be represented as

$$B_{11}^i = \begin{bmatrix} b_{11}^i & 0 & 0 \\ 0 & b_{22}^i & 0 \\ 0 & 0 & b_{33}^i \end{bmatrix}, \quad (\text{A.7})$$

where i ranges from 1 to 8. Similarly, B_{21}^i can be represented as

$$B_{21}^i = \begin{bmatrix} b_{41}^i & b_{42}^i & 0 \\ b_{51}^i & 0 & b_{53}^i \\ 0 & b_{62}^i & b_{63}^i \end{bmatrix}, \quad (\text{A.8})$$

where again, i ranges from 1 to 8. Taking a single term from Equation (A.4) and substituting Equations (A.5 - A.8) gives

$$\begin{aligned} & B_{11}^{i T} C_{11} B_{11}^j + B_{21}^{i T} C_{22} B_{21}^j \\ &= \begin{bmatrix} b_{11}^i & 0 & 0 \\ 0 & b_{22}^i & 0 \\ 0 & 0 & b_{33}^i \end{bmatrix} \begin{bmatrix} c_{11} & c_{12} & c_{13} \\ c_{12} & c_{22} & c_{23} \\ c_{13} & c_{23} & c_{33} \end{bmatrix} \begin{bmatrix} b_{11}^j & 0 & 0 \\ 0 & b_{22}^j & 0 \\ 0 & 0 & b_{33}^j \end{bmatrix} \\ &+ \begin{bmatrix} b_{41}^i & b_{51}^i & 0 \\ b_{42}^i & 0 & b_{62}^i \\ 0 & b_{53}^i & b_{63}^i \end{bmatrix} \begin{bmatrix} c_{44} & 0 & 0 \\ 0 & c_{55} & 0 \\ 0 & 0 & c_{66} \end{bmatrix} \begin{bmatrix} b_{41}^j & b_{42}^j & 0 \\ b_{51}^j & 0 & b_{53}^j \\ 0 & b_{62}^j & b_{63}^j \end{bmatrix}, \end{aligned} \quad (\text{A.9})$$

Carrying out the nonzero matrix multiplications gives

$$[[B]^T[C][B]]_{ij} = \begin{bmatrix} b_{11}^i c_{11} b_{11}^j & b_{11}^i c_{12} b_{22}^j & b_{11}^i c_{13} b_{33}^j \\ b_{22}^i c_{12} b_{11}^j & b_{22}^i c_{22} b_{22}^j & b_{22}^i c_{23} b_{33}^j \\ b_{33}^i c_{13} b_{11}^j & b_{33}^i c_{23} b_{22}^j & b_{33}^i c_{33} b_{33}^j \end{bmatrix} + \quad (\text{A.10})$$

$$\begin{bmatrix} b_{41}^i c_{44} b_{41}^j + b_{66}^i c_{55} b_{66}^j & b_{51}^i c_{44} b_{42}^j & b_{51}^i c_{55} b_{53}^j \\ b_{42}^i c_{44} b_{41}^j & b_{42}^i c_{44} b_{42}^j + b_{62}^i c_{66} b_{62}^j & b_{62}^i c_{66} b_{63}^j \\ b_{53}^i c_{55} b_{51}^j & b_{63}^i c_{66} b_{62}^j & b_{53}^i c_{55} b_{53}^j + b_{63}^i c_{66} b_{63}^j \end{bmatrix} .$$

Thus the element stiffness matrix can be completely formed by ranging both i and j from 1 to 8 independently, giving a 24×24 elemental stiffness matrix.

The global load vector for the micromechanics model is composed of nodal loads applied at the corners of the model and element loads resulting from strains such as those caused by thermal loads or viscoelastic creep. Of interest here are the element load vectors, as formulation of these vectors requires large numbers of matrix multiplications.

To begin, an arbitrary element load vector assumes the form

$$[F_e] = \int_V [B]^T [C] \{Z\} dV , \quad (\text{A.11})$$

where $\{Z\}$ represents an arbitrary initial strain vector for a specific loading increment.

Upon partitioning $\{Z\}$ and $[B]$ as before, Equation (A.11) becomes

$$\{F\} = \begin{Bmatrix} B_{11}^1{}^T C_{11} Z_1 + B_{21}^1{}^T C_{22} Z_2 \\ \vdots \\ B_{11}^8{}^T C_{11} Z_1 + B_{21}^8{}^T C_{22} Z_2 \end{Bmatrix} , \quad (\text{A.12})$$

where $\{Z\}$ was also partitioned as

$$\{Z\} = \begin{Bmatrix} Z_1 \\ Z_2 \end{Bmatrix} , \quad (\text{A.13})$$

and

$$Z_1 = \begin{Bmatrix} \zeta_1 \\ \zeta_2 \\ \zeta_3 \end{Bmatrix}, \quad (A.14)$$

$$Z_2 = \begin{Bmatrix} \zeta_4 \\ \zeta_5 \\ \zeta_6 \end{Bmatrix},$$

respectively. Utilizing Equations (A.5 - A.8) and Equations (A.12 - A.14) gives one term of the partitioned load vector as

$$\begin{aligned} \{F\}_i = & \begin{bmatrix} b_{11}^i & 0 & 0 \\ 0 & b_{22}^i & 0 \\ 0 & 0 & b_{33}^i \end{bmatrix} \begin{bmatrix} c_{11} & c_{12} & c_{13} \\ c_{12} & c_{22} & c_{23} \\ c_{13} & c_{23} & c_{33} \end{bmatrix} \begin{Bmatrix} \zeta_1 \\ \zeta_2 \\ \zeta_3 \end{Bmatrix} \\ & + \begin{bmatrix} b_{41}^i & b_{51}^i & 0 \\ b_{42}^i & 0 & b_{62}^i \\ 0 & b_{53}^i & b_{63}^i \end{bmatrix} \begin{bmatrix} c_{44} & 0 & 0 \\ 0 & c_{55} & 0 \\ 0 & 0 & c_{66} \end{bmatrix} \begin{Bmatrix} \zeta_4 \\ \zeta_5 \\ \zeta_6 \end{Bmatrix}. \end{aligned} \quad (A.15)$$

Carrying out the matrix multiplications gives the final result

$$\{F\}_i = \begin{Bmatrix} b_{11}^i(c_{11}\gamma_1 + c_{12}\gamma_2 + c_{13}\gamma_3) \\ b_{22}^i(c_{12}\gamma_1 + c_{22}\gamma_2 + c_{23}\gamma_3) \\ b_{33}^i(c_{13}\gamma_1 + c_{23}\gamma_2 + c_{33}\gamma_3) \end{Bmatrix} + \begin{Bmatrix} b_{41}^i c_{44} \gamma_4 + b_{51}^i c_{55} \gamma_5 \\ b_{42}^i c_{44} \gamma_4 + b_{62}^i c_{66} \gamma_6 \\ b_{53}^i c_{55} \gamma_5 + b_{63}^i c_{66} \gamma_6 \end{Bmatrix}. \quad (A.16)$$

Hence, ranging i from 1 to 8 gives the formulated load vector. Moreover, it should be noted that if the load vector is for a thermal load case, the latter column vector of Equation (A.16) vanishes, as the shear strains are zero. The remaining terms in the load vector take the form

$$\{F\}_i = \begin{Bmatrix} b_{11}^i(c_{11}\alpha_1 + c_{12}\alpha_2 + c_{13}\alpha_3) \\ b_{22}^i(c_{12}\alpha_1 + c_{22}\alpha_2 + c_{23}\alpha_3) \\ b_{33}^i(c_{13}\alpha_1 + c_{23}\alpha_2 + c_{33}\alpha_3) \end{Bmatrix} \Delta T, \quad (A.17)$$

where α_i represents the coefficients of thermal expansion, and ΔT represents the change in temperature.

APPENDIX B.

VOLUME AVERAGING RELATIONS FOR SPATIALLY VARYING STRESS/STRAIN FIELDS IN A COMPOSITE RVE

Given a representative volume element (RVE) for a composite material, the continuum definitions of stress and strain are defined by the volume average of these quantities within the RVE. Moreover, determining effective composite properties for a material represented by the RVE requires knowledge of these volume averaged fields. In the interest of numerical efficiency, it is desirable to relate the volume averaged stress and strain fields to surface quantities defined on the boundary of the RVE. The expressions for the volume averaged fields follows the development of Laws (1980).

To begin, the strain tensor for small strain theory is defined as

$$\tilde{\varepsilon} = \frac{1}{2} [(\nabla \bar{u}) + (\nabla \bar{u})^T] \quad , \quad (\text{B.1})$$

where $(\nabla \bar{u})$ is the displacement gradient. The volume average of the spatially varying displacement gradient is given by

$$\langle (\nabla \bar{u}) \rangle = \frac{1}{V} \int_D (\nabla \bar{u}) dV \quad , \quad (\text{B.2})$$

where D represents the domain of the RVE. The “diamond brackets” $\langle \rangle$ are used to identify a volume averaged quantity.

An expanded form of the divergence theorem from tensor calculus may be used to transform the volume integral in Equation (B.2) into a surface integral as

$$\int_D (\nabla \bar{u}) dV = \int_S (\bar{u} \bar{n}) dA \quad , \quad (\text{B.3})$$

where $(\bar{u} \bar{n})$ is the dyad of the vectors \bar{u} and \bar{n} , and \bar{n} is the unit normal outward to the surface S of the RVE. The average displacement gradient is then given by

$$\langle (\nabla \bar{u}) \rangle = \frac{1}{V} \int_S (\bar{u} \bar{n}) dA \quad , \quad (\text{B.4})$$

and further

$$\langle (\nabla \bar{u})^T \rangle = \frac{1}{V} \int_S (\bar{n} \bar{u}) dA \quad . \quad (\text{B.5})$$

Substituting Equations (B.4) and (B.5) into the definition of the strain gives

$$\langle \tilde{\varepsilon} \rangle = \frac{1}{2V} \int_S [(\bar{u} \bar{n}) + (\bar{n} \bar{u})] dA \quad . \quad (\text{B.6})$$

Thus, the volume averaged strain field of the RVE is completely defined in terms of displacements of the boundaries of the RVE.

Now let's look at the volume averaged stresses and relate them to the edge tractions for easy calculation. Consider the definition of the volume averaged stress for the RVE as

$$\langle \tilde{\sigma} \rangle = \frac{1}{V} \int_D \tilde{\sigma} dV \quad . \quad (\text{B.7})$$

Yet another expanded form of the divergence theorem is given by

$$\int_S (\bar{\nu} \{ \tilde{\mathbf{B}}^T \cdot \bar{\mathbf{n}} \}) dA = \int_D [(\nabla \bar{\nu}) \cdot \tilde{\mathbf{B}} + (\bar{\nu} \{ \nabla \cdot \tilde{\mathbf{B}}^T \})] dV \quad , \quad (\text{B.8})$$

where $\bar{\nu}$ is a vector field, and $\tilde{\mathbf{B}}$ is a second order tensor field. Now choose $\bar{\nu}$ to be the position vector, $\bar{\mathbf{x}}$, such that $(\nabla \bar{\mathbf{x}}) = \tilde{\mathbf{I}}$, where $\tilde{\mathbf{I}}$ is the identity tensor. Further, choose $\tilde{\mathbf{B}}$ to be the symmetric stress tensor, $\tilde{\sigma}$. Equation (B.8) can then be rewritten as

$$\int_S (\bar{\mathbf{x}} \{ \tilde{\sigma} \cdot \bar{\mathbf{n}} \}) dA = \int_D [\tilde{\sigma} + (\bar{\mathbf{x}} \{ \nabla \cdot \tilde{\sigma} \})] dV \quad . \quad (\text{B.9})$$

Rearranging the above gives

$$\int_D \tilde{\sigma} dV = - \int_D (\bar{\mathbf{x}} \{ \nabla \cdot \tilde{\sigma} \}) dV + \int_S (\bar{\mathbf{x}} \{ \tilde{\sigma} \cdot \bar{\mathbf{n}} \}) dA \quad . \quad (\text{B.10})$$

Neglecting body forces, equilibrium requires the divergence of the stress tensor to be zero, and thus the above collapses to

$$\int_D \tilde{\sigma} dV = \int_S (\bar{\mathbf{x}} \{ \tilde{\sigma} \cdot \bar{\mathbf{n}} \}) dA \quad . \quad (\text{B.11})$$

The term $\tilde{\sigma} \cdot \bar{\mathbf{n}}$ is equivalent to the traction on the surface S for the outward normal $\bar{\mathbf{n}}$, denoted by $\bar{\mathbf{t}}$. Substituting this result into the above gives

$$\int_D \tilde{\sigma} dV = \int_S (\bar{x}\bar{t}) dA. \quad (\text{B.12})$$

The expression on the left side of Equation (B.12) is precisely the volume average of the stress multiplied by the volume of the RVE. Hence, one can write

$$\langle \tilde{\sigma} \rangle = \frac{1}{V} \int_S (\bar{x}\bar{t}) dA. \quad (\text{B.13})$$

Now we have completely related the volume average stresses to the tractions along the boundary for any RVE.

Now consider the hexagonally packed unit cell (or RVE) as shown in Figure B.1. Equations (B.6) and (B.13) show that one can relate the volume averaged stresses and strains to integrals along the boundary of the RVE.

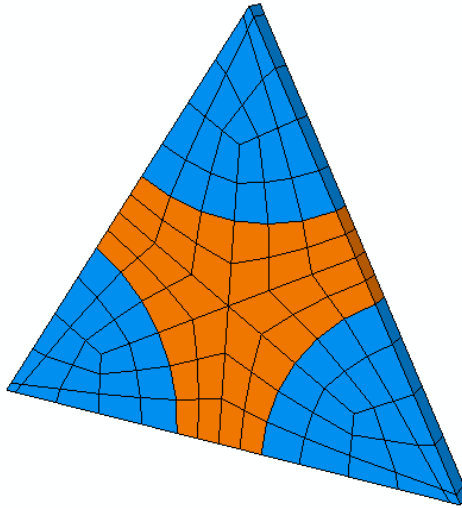


Figure B.1 Hexagonally packed representative volume element (RVE).

In a finite element implementation, the tractions and the displacements are known for every node on the boundary of the RVE. Thus, one could potentially utilize an approximate integration technique to determine the volume averaged stress and strain field for any given load case.

APPENDIX C. MACROSCOPIC STRESS AND STRAIN CALCULATIONS

A critical element of the hexagonally packed micromechanics analysis presented in this thesis is the ability to compute macroscopic stress and strain fields from corner node forces and displacements, respectively. An equally important feature of the analysis is that all 6 stress and strain states may be computed with the identical fixity of the corner nodes. This allows all load cases of interest to be computed with a single factorization of the stiffness matrix. Consider Figure C.1 as shown below. If b represents the length of the sides of the equilateral unit cell, the height of the triangle can be calculated from simple trigonometry as

$$h = \frac{\sqrt{3}}{2} b \quad . \quad (C.1)$$

To load the model, the work of Garnich (1996) is considered in detail. To prevent rigid body translation, the back face node pair of node 3 is fixed in all three degrees-of-freedom. Node 3 is fixed in all but the x_1 -direction to constrain rigid body rotation about the x_2 and x_3 axes. Lastly, node 1 is fixed in the x_2 -direction to constrain rigid body rotation about the x_1 -axis.

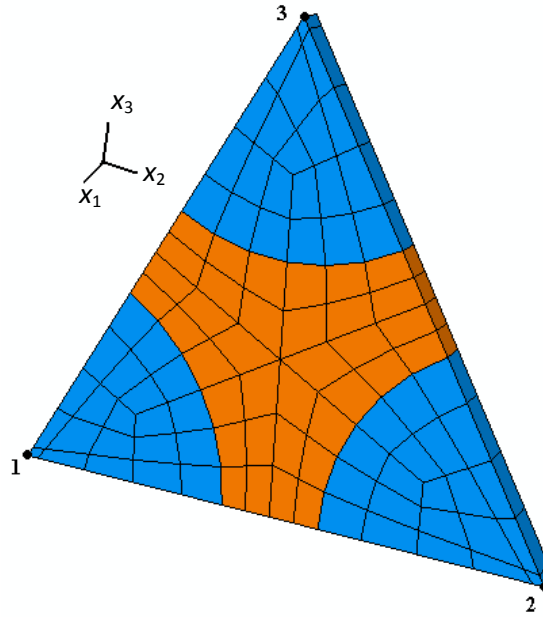


Figure C.1 Optimized mesh representation of unit cell with corner node labels.

C.1 Macroscopic Stress Calculation

To calculate the stresses resulting from nodal loads, one must consider the cross sectional area from the geometry of the unit cell. Keeping with the nodal definitions of Figure C.1, node 3 is the only node to be loaded for a longitudinal stress state. Because the constraint equations force the distance of the nodal pairs on the front and back faces to be the same as the distance between the top corner nodes on the front and back face, the stress is simply the nodal load divided by the area of the front face as

$$\sigma_{11} = \frac{F_{x_1}^{(3)}}{A_{x_1}} , \quad (\text{C.2})$$

where the subscript on F denotes the direction of the loading, the superscript denotes the specified node, and A_{x_1} is the face area defined by

$$A_{x_1} = \frac{\sqrt{3}}{4} b^2 \quad . \quad (C.3)$$

Substituting the above into the expression for the longitudinal stress gives

$$\sigma_{11} = F_{x_1}^{(3)} \frac{4}{\sqrt{3} b^2} \quad . \quad (C.4)$$

To apply a stress solely in the x_2 -direction, only node 2 need be loaded along the x_2 -axis because node 1 is constrained in this degree of freedom. The stress in the x_2 -direction is calculated again by the nodal load divided by the cross sectional area in the x_2 -direction. The average area of the x_2 face of the unit cell is simply the height of the unit cell multiplied by the thickness as

$$A_{x_2} = \frac{\sqrt{3}}{4} b d \quad , \quad (C.5)$$

where d is the thickness of the RVE. Substituting for the definition of stress gives the final stress in the x_2 -direction as

$$\sigma_{22} = \frac{4F_{x_2}^{(2)}}{\sqrt{3} b d} \quad . \quad (C.6)$$

Similarly, for a stress in the x_3 -direction, both nodes 1 and 2 need be loaded equally along the x_3 -axis, giving the stress as

$$\sigma_{33} = \frac{2F_{x_3}^{(1,2)}}{A_{x_3}} \quad , \quad (C.7)$$

where A_{x_3} is the average area of the unit cell's x_3 face given by

$$A_{x_3} = \frac{bd}{2} . \quad (C.8)$$

Substituting the above definition into the Equation (C.7) gives

$$\sigma_{33} = \frac{4F_{x_3}^{(1,2)}}{bd} . \quad (C.9)$$

The shear stresses are much more difficult to calculate as they involve multiple nodal loads. Consider Figure C.2 depicting shearing about the x_3 -axis.

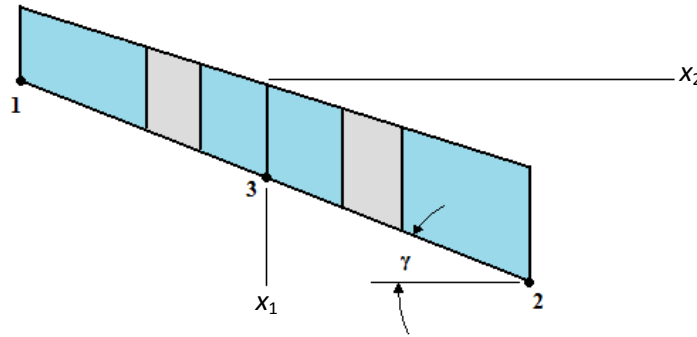


Figure C.2 Representation of shearing about the x_3 -axis for the micromechanics unit cell.

Here, only equal and opposite loads need be applied to nodes 1 and 2 to produce the desired stress-state. The stress is then defined as

$$\sigma_{12} = \frac{2F_{x_1}^{(1,2)}}{A_{x_2}} , \quad (C.10)$$

or knowing A_{x_2} the expression reduces to

$$\sigma_{12} = \frac{8F_{x_1}^{(1,2)}}{\sqrt{3}bd} . \quad (C.11)$$

To define the shear stress σ_{13} , it is desirable to cause the unit cell to have angle changes solely about the x_2 axis. To enforce this idea, consider Figure C.3.

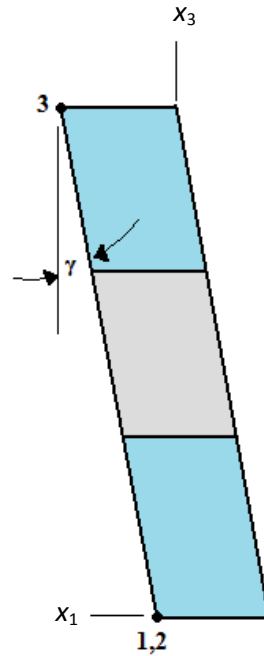


Figure C.3 Representation of shearing about the x_2 -axis for the unit cell.

To achieve this stress state, nodes 1 and 2 must be loaded equally along the x_1 axis, and node 3 must be loaded in the opposite direction with a magnitude equal to the sum of the nodal loads on 1 and 2. Because these loads are acting to increase the angle, they must be summed as

$$\sigma_{13} = \frac{2F_{x_1}^{(1,2)}}{A_{x_3}} + \frac{F_{x_1}^{(3)}}{A_{x_3}} . \quad (\text{C.12})$$

Substituting the known expression for A_{x_3} and knowing the load on node 3 is twice that of the load on nodes 1 and 2 gives the final expression as

$$\sigma_{13} = \frac{4F_{x_1}^{(1,2)}}{bd} \quad . \quad (C.13)$$

Shear stress σ_{23} is much more difficult to comprehend as it involves multiple degrees of freedom. Consider Figure C.4 depicting shearing about the x_1 -axis.

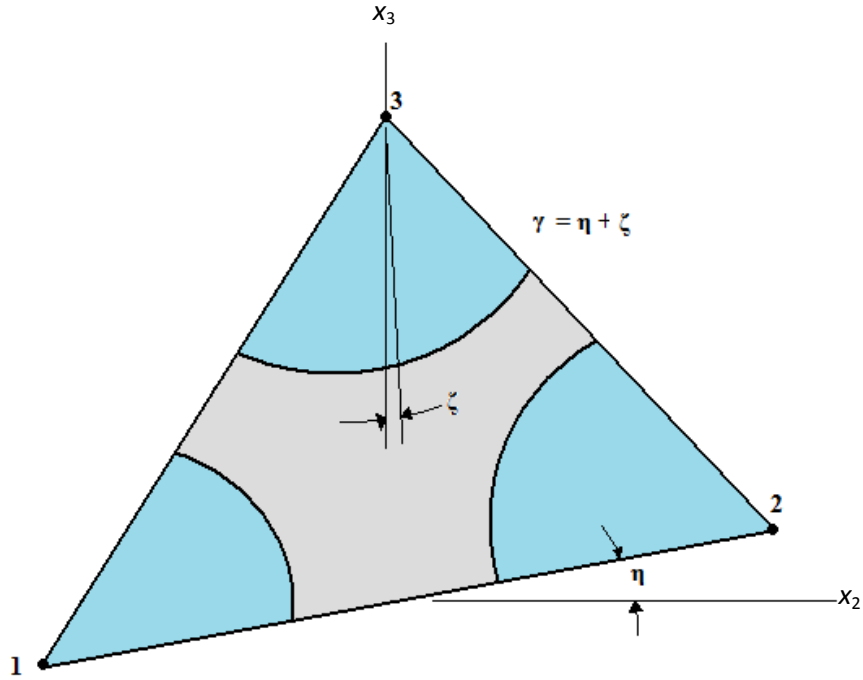


Figure C.4 Representation of shearing about the x_1 -axis for the micromechanics unit cell.

To generate the transverse shear, nodes 1 and 2 must be loaded in an equal and opposite manner in the x_3 -direction, but because node 1 is fixed in the x_2 -direction a resulting moment occurs within the unit cell. To counteract the moment, node 2 must be loaded in the x_2 -direction. The transverse shear stress is then given by

$$\sigma_{23} = \frac{2F_{x_2}^{(1,2)}}{A_{x_3}} - \frac{F_{x_3}^{(2)}}{A_{x_2}} \quad . \quad (C.14)$$

Substituting the known areas in the above gives the final expression for the transverse shear as

$$\sigma_{23} = \frac{8F_y^{(1,2)}}{\sqrt{3}bd} - \frac{2F_z^{(2)}}{bd} . \quad (\text{C.15})$$

Hence, for any combinations of loading, the stresses can be calculated in a very efficient manner.

C.2 Macroscopic Strain Calculation

For an arbitrary load on the unit cell, the strains can be determined from the corner node displacements on the front face. In particular, consider the strain components given by

$$\varepsilon = [\varepsilon_{11} \quad \varepsilon_{22} \quad \varepsilon_{33} \quad \gamma_{12} \quad \gamma_{13} \quad \gamma_{23}]^T , \quad (\text{C.16})$$

where it is emphasized that engineering shear strains are being computed. Now take u representing the displacement in the x_1 -direction, v as the displacement in the x_2 -direction, and w as the displacement in the x_3 -direction. Using the small strain assumption, longitudinal strain ε_{11} can be calculated by the change in the displacement in the x_1 -direction as

$$\varepsilon_{11} = \frac{u^{(3)}}{d} , \quad (\text{C.17})$$

where the superscript represents the node of interest. Because nodes 1 and 3 are constrained in the x_2 -direction, ε_{22} is simply calculated by

$$\varepsilon_{22} = \left(\frac{v^{(2)}}{b} \right) . \quad (\text{C.18})$$

The strain in the x_3 -direction, ε_{33} , is calculated from the average displacement of nodes 1 and 2 as

$$\varepsilon_{33} = - \left(\frac{w^{(1)} + w^{(2)}}{2} \right) \left(\frac{1}{h} \right) . \quad (\text{C.19})$$

Substituting the definition of h from above gives

$$\varepsilon_{33} = - \left(\frac{w^{(1)} + w^{(2)}}{2} \right) \left(\frac{2}{\sqrt{3}b} \right) . \quad (\text{C.20})$$

Consider shearing about the x_3 -axis as shown in Figure C.2. Assuming small angles, the shear strain γ_{12} is readily calculated as

$$\gamma_{12} = \frac{(u^{(2)} - u^{(1)})}{b} . \quad (\text{C.21})$$

Consider the shear strain γ_{13} described by the rotation about the x_2 -axis as shown in Figure C.3. The rotation can be calculated from the front face nodes as

$$\gamma_{13} = \left(\left(\frac{u^{(1)} + u^{(2)}}{2} \right) - u^{(3)} \right) \left(\frac{1}{h} \right) . \quad (\text{C.22})$$

Substituting the expression for h into the above gives

$$\gamma_{13} = \left(\left(\frac{u^{(1)} + u^{(2)}}{2} \right) - u^{(3)} \right) \left(\frac{2}{\sqrt{3}b} \right) . \quad (\text{C.23})$$

Consider again Figure C.4 depicting transverse shear. As with calculating the stress for this loading case, the displacements of nodes 1 and 2 in the x_3 -direction and the displacement of node 2 in the x_2 -direction must all be considered when defining the shear strain. Following the derivation of the transverse stress gives the transverse strain as

$$\gamma_{23} = \frac{(w^{(2)} - w^{(1)})}{b} + \frac{2v^{(2)}}{\sqrt{3}b} . \quad (\text{C.24})$$